Early-warning signals for sudden changes in dynamical flow patterns

Dissertation

zur Erlangung des akademischen Grades
Doctor of Philosophy (Ph.D.)

vorgelegt

dem Bereich Mathematik und Naturwissenschaften
der Technischen Universität Dresden

von

Moussa Ndour

Tag der Einreichung: 08. April 2020
Tag der Verteidigung: 11. May 2020

Gutachter: Prof. Dr. Kathrin Padberg-Gehle
Leuphana Universität Lüneburg
Prof. Dr. Axel Voigt
Technischen Universität Dresden
Prof. Dr. Martin Rasmussen
Imperial College London

Abstract

The understanding and prediction of sudden changes in flow patterns is of paramount importance in the analysis of geophysical flows as these rare events relate to critical phenomena such as atmospheric blocking, the weakening of the Gulf stream, or the splitting of the polar vortex. In this thesis, our aim is to fully set up a theoretical understanding of vortex splitting phenomena with concrete real-world applications. To this end, we firstly study bifurcations of global flow patterns in parameter-dependent two-dimensional incompressible flows, with the flow patterns of interest corresponding to specific invariant sets. Based on already known classical bifurcation results from probabilistic approaches, we exploit the discrete spectrum of a perturbed Frobenius-Perron operator to build almost-invariant sets from perturbed invariant sets and study their changes as the bifurcation parameter is varied. Even though these almost-invariant sets are supported in a neighborhood of a critical point that later bifurcates, our spectral results suggest a novel approach.

We, then, re-describe the underlying dynamics in terms of a reversible finite-state Markov chain in order to spectrally characterize a set-oriented bifurcation from matrix perturbations theory. Indeed, perturbed eigenvalues and their corresponding eigenvectors sign patterns are inter-dependently used as observables, to successfully depict generic indicators for pattern splitting.

These findings are, thus, extended to more realistic time-dependent systems where perturbed singular vectors and their singular values yield observables. Therefore, spectral early-warning signals are proven to be robust, given a specific class of incompressible time-dependent systems. Our results are confirmed, in application, by studying spectral indicators of the Antarctic ozone hole sudden break up in September 2002, from satellite velocity data.

Zusammenfassung

Das Verständnis und die Vorhersage von plötzlichen Veränderungen in Strömungsmustern sind bei der Analyse von geophysikalischen Strömungen von großer Bedeutung, da solche seltenen Ereignisse häufig mit kritischen Phänomenen zusammenhängen, beispielsweise der atmosphärischen Blockierung, der Abschwächung des Golfstroms oder der Aufspaltung der Polarwirbel.

In dieser Dissertation wollen wir ein umfassendes theoretisches Verständnis insbesondere von Wirbelaufspaltungen entwickeln und dies mit mit konkreten praktischen Anwendungen verbinden. Zu diesem Zweck untersuchen wir zunächst Bifurkationen von globalen Strömungsmustern in parameterabhängigen, zweidimensionalen, inkompressiblen Strömungen, wobei die interessierenden Strömungsmuster bestimmten invarianten Mengen entsprechen. Auf der Grundlage bekannter klassischer Verzweigungsergebnisse aus probabilistischen Ansätzen nutzen wir das diskrete Spektrum eines gestörten Frobenius-Perron-Operators, um aus gestörten invarianten Mengen sogenannte fast-invariante Mengen zu konstruieren und deren Änderungen bei Variation der Bifurkationsparameter zu untersuchen. Auch wenn diese fast-invarianten Mengen in einer lokalen Umgebung des sich später verzweigenden kritischen Punktes liegen, deuten unsere spektralen Ergebnisse auf einen neuen Ansatz hin.

Mit einer neuen Beschreibung der zugrunde liegenden Dynamik in Form einer diskreten, reversiblen, endlichen Markov-Kette erhalten wir dann eine spektrale Charakterisierung einer mengenorientierten Verzweigung auf Grundlage von Matrix-Störungstheorie. Tatsächlich werden gestörte Eigenwerte und die Vorzeichenmuster der entsprechenden Eigenvektoren gemeinsam als Beobachtungsgrößen verwendet, um generische Indikatoren für die Aufspaltung von Strömungsmustern erfolgreich abzubilden.

Diese Ansätze werden dann auf realistischere, zeitabhängige Systeme ausgedehnt, bei denen gestörte singuläre Vektoren und ihre Singulärwerte die entsprechenden Beobachtungsgrößen liefern. Dabei erweisen sich unsere spektralen Frühwarnsignale in den betrachteten inkompressiblen, zeitabhängigen Systemen als robust. Die Ergebnisse bestätigen sich in der Anwendung. Insbesondere untersuchen wir spektrale Indikatoren

der plötzlichen Aufspaltung des Ozonlochs über der Antarktis im September 2002 auf Grundlage von durch Satelliten gemessenen Geschwindigkeitsdaten.

Contents

1 Introduction

Understanding critical transitions in the macroscopic behavior of dynamical systems is, nowadays, of high interest due to the emergence of new scientific challenges towards developing mathematical theories for bifurcations of complex systems [3]. The ultimate goal is to provide indicators or early warning signals for the prediction of sudden changes in flow patterns emerging in real world systems such as the atmosphere. For instance, the Antarctic polar vortex break up scenario in late September 2002 appears as a rotating atmospheric pattern that suddenly splits [7, 9, 38]. Figure 1.1 illustrates graphically this splitting event from velocity data. One may classify this splitting event as a critical

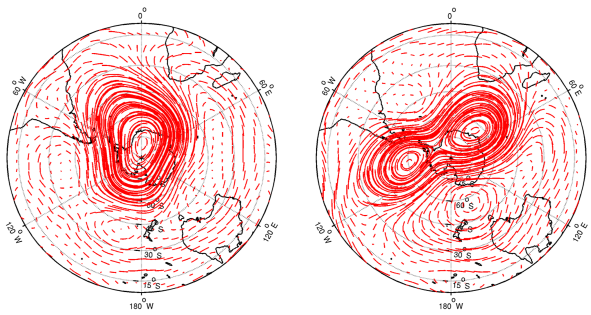

September 20, 2002 September 25, 2002

Figure 1.1: Antarctic polar vortex splitting event in September 2002, visualized using two-dimensional velocity data from the ECMWF Interim data set (http://data.ecmwf.int/data/index.html).

transition of patterns occurring in a specific natural complex system. Moreover, such complex system may be modeled as incompressible time-dependent dynamical systems where the sudden critical change is characterized as a critical transition [3, 5, 6] of dominant slowly mixing patterns. Thus, a legitimate question arises: How could such an

event be predicted before it happened? We suggest that a possible answer to this question can be found by the combination of a model-based approach and its set-oriented analysis. This means that, first, one needs to find a mathematical model that is representative enough for the underlying complex system phenomena. Secondly, from the newly built model, one needs to be able to distinguish and study critical transitions for patterns that, a priori, behave similar to the polar vortex. Indeed, from the dynamics of the chosen model, it follows that the task of finding **observables** as **early-warning signals** of any radical split of the resulting pattern will progressively lead to predicting the occurrence of the critical transition which may emerge as a sudden change.

Fortunately, there is an established mathematical concept to represent dominant slowly mixing patterns from a time evolving dynamical system [13, 15, 36]. This is mainly based on a measurable partition of the phase space into regions that are dynamically almost disjoint and thus material transport between these regions, or patterns is minimal. In case of autonomous systems, those regions are commonly called almost-invariant sets [13, 14] since they mitigate transport between their interior and the rest of the phase space. They are called coherent sets in the context of nonautonomous systems, as they move over time with minimal dispersion [15, 16]. The theory leading to the construction of these dominant patterns is mainly based upon the Perron-Frobenius operator. The latter is an infinite dimensional linear operator which maps the time evolution of probability densities, see [49] for more details. However, the discrete spectrum and the corresponding eigenfunctions of a dynamically similar, perturbed linear operator are systematically used to extract the patterns of interest [13, 15]. Besides, finite time bifurcation theory has been recently introduced in [58]. There, central concepts such as finite time attractivity and finite time repulsivity were analytically formulated and applied mainly to low dimensional dissipative nonautonomous systems undergoing critical transitions. However, the main concept of finite time dynamical systems can be transferred to incompressible flows, which will be our main interest in this research study.

To the best of our knowledge, a set-oriented bifurcation analysis is still a broadly open topic that may require a new theoretical approach beyond classical bifurcation theory. Known previous works in this direction include using the discrete spectrum of the deterministic Perron-Frobenius operator (referred to as transfer operator) generated by dissipative and non-dissipative systems. In [17] a transfer operator based framework was successfully developed for studying the one-dimensional pitchfork normal form. Indeed, particular changes in the discrete spectrum of the transfer operator, including

accumulation of eigenvalues to 1 as the critical parameter is reached, yield indicators of the pitchfork bifurcation.

The study of the time evolution of deterministic dynamical systems via a probabilistic approach has been a subject of intense research during the last decades. In particular, it has been used in many topics including physics and classical statistical mechanics [48, 49]. For Anosov flows [45, 47], the probabilistic framework is provenly very suitable for the analytical investigation of statistical properties of the dynamical systems. Examples include chaos, ergodicity and mixing properties. These dynamical properties are mathematically formulated after an invariant measure, or invariant distribution is found, or assumed to exist. In terms of densities, the probability distributions always converge to the existing unique invariant density when the system is mixing [52]. The spectrum of the Perron-Frobenius operator generated by an Anosov flow and sometimes referred to as the mixing spectrum [63], is used to interpret the global mixing properties of a given dynamical system. It is also relevant for studying bifurcations within a statistical view point. Indeed, the discrete spectrum of the Perron-Frobenius operators is directly linked to the hyperbolic stationary points of the underlying dynamical system [17, 46]. Thus, the spectrum captures the stretching or contracting dynamics near stationary states. Therefore, a critical transition of the dynamical system can be characterized by significant changes in the spectrum of the Perron-Frobenius operators, when a critical parameter is reached.
However, despite the mixing nature of a given system, there may exist regions in phase space that resist mixing under the action of the dynamical system. These regions turn out to be very relevant in the study of transport processes [41–44]. Hence, it would be very crucial – but highly challenging – to predict their occurrences, their bifurcations and their decays. Indeed, to the best of our knowledge, a set-oriented, probabilistic bifurcation theory is still a broadly open research topic that requires the development of approaches beyond the traditional bifurcation concepts. Furthermore, a probabilistic description of critical transitions in flow patterns will help to get a better understanding of possible early warning signals for sudden changes in geophysical real-world fluid dynamics, such as Antarctic vortex splitting event.

In [18] early warning indicators for transitions between atmospheric flow regimes were defined based on the transfer operator of a dissipative atmospheric model. In that work, the discrete spectrum of the transfer operator was initially used to approximate two isolated regimes as almost-invariant sets. Closer to the setting of the present work,

bifurcations of almost-invariant and almost-cyclic sets in two-dimensional conservative systems and corresponding changes in the spectrum of the transition matrices were observed in [19, 20] but not systematically studied.
As a matter of fact, the three major axes of our research study will be as follows:

Firstly, this thesis addresses the problem of characterizing bifurcation of almost-invariant sets from the classical bifurcation theory approach. That is, we seek qualitative changes of those sets by studying qualitative changes of local fixed points. This approach is similar to [17] but we use a perturbed transfer operator, instead of the deterministic Frobenius-Perron operator. The advantage of using the perturbed transfer operator resides in the nature of its discrete spectrum, at first sight. Indeed, we can identify a particular subset of real eigenvalues whose magnitudes are close to 1. In addition to that, positive/negative level sets of the corresponding eigenfunctions yield almost-invariant sets. However, bifurcation can only be studied numerically. Thus, with this approach one can see a spectral signature through significant changes of numerically approximated real eigenvalues, as a bifurcation parameter crosses its critical value. This result is similar to what is observed in [17]. However, changes in the approximated real eigenvectors corresponding to those real eigenvalues do not yield any set-oriented bifurcation insight. That is why, the second part of this thesis contribution consists of providing first steps towards predicting bifurcation of patterns that can mathematically be represented as optimal almost-invariant sets. Our approach is still probabilistic and will be mainly based on analyzing the spectral behavior of discrete Markov chains subject to external perturbations. The corresponding stochastic transition matrices are finite rank approximations of the Perron-Frobenius operator and its diffused version. Almost-invariant sets are numerically approximated by the dominant eigenvector basis of the transition matrix. Moreover, we use the sign structures of these vectors to systemically design the meaningful patterns that emerge from the dynamical system under study. Meanwhile, the behavior of the corresponding dominant eigenvalues under parameter-variation indicates when radical changes of patterns occur. Indeed, as the bifurcation parameter is varied, eigenvalues change continuously with respect to the parameter.
Finally, this thesis investigates the finite time bifurcation of coherent sets with the main goal of establishing a better understanding of early warning signals for sudden pattern splitting. The latter is motivated by the Antarctic polar vortex sudden break up in September 2002, as illustrated in figure 1.1. To this end, we study specific classes of nonautonomous systems who mimic the Antarctic polar vortex dynamics. To the best of our knowledge the bifurcation analysis of coherent sets as formulated in this work, has

remained a widely unexplored topic.
In the following is listed a brief outline of this thesis.

In chapter 2 and chapter 3 we respectively give the background study of the probabilistic analysis of deterministic systems and the background study of set-oriented dynamical systems. These two theories are actually in the core of our research study. Indeed, a set-oriented analysis of a dynamical system (chapter 3) is a particular probabilistic approach to analyzing dynamical systems (chapter 2). Besides, the particularity of a set-oriented approach is tied to the fact that the latter focus on extracting optimal coherent sets, while the probabilistic analysis of deterministic systems may lead to diverse conclusions including ergodicity. Hence, in addition to defining basics concepts of Frobenius-Perron operators, we give detailed mathematical constructions of almost-invariant sets and coherent sets.

In chapter 4, we challenge our understanding about where should the study of a set-oriented bifurcation really start, compared to already known classical bifurcation theory. In fact, our approach can only start from the most comprehensive way towards solving the main question of this thesis. Thus, chapter 4 explores the possibility of extending already known results about characterizing local bifurcations from a statistical approach. Namely, in [17], the spectral signature of the one-dimensional pitchfork normal form was developed. Therefore, in chapter 4 we use the ϵ-perturbed Frobenius-Perron operator and study the spectral signature of the pitchfork bifurcation of a two-dimensional Duffing-like oscillator system. Indeed, the latter yields a center stationary point for negative p and two center stationary points for positive p. Furthermore, the underlying system's dynamics mimics somehow the Antarctic polar vortex rotating dynamics and the undergoing bifurcations mimics the splitting scenario.

Results in chapter 4 have freed the set-oriented bifurcation study from the local bifurcation which is intrinsic to the system. Therefore, in chapter 5 we concretely study bifurcation of almost-invariant sets, in the sense of pattern splitting. There, we briefly review the concept of almost-invariant sets within a set-oriented numerical framework, which yields stochastic transition matrices for reversible finite-state Markov chains. We address results from the perturbation theory of stochastic matrices and show how their dominant spectrum is suitable for estimating almost-invariant sets that originate from invariant structures of the unperturbed dynamics. In order to illustrate the numerical framework, we discuss the practical computation of the dominant almost-invariant sets for a two-dimensional non-dissipative flow. Then, we start the foremost step by system-

atically experimenting Markov chain toy models undergoing bifurcations of specifically constructed patterns. Finally, we rigorously study two explicit dynamical models, a Duffing-type oscillator and a single gyre flow, and identify early warning signals for splittings of patterns through the trends of eigenvalues with respect to a bifurcation parameter. Findings in chapter 5 have been submitted for publication, see [57].

Patterns emerging from complex dynamics of real world systems, such as the Antarctic polar vortex break up in late September 2002, suggest an analogous nonstationary framework. That is, in order to apply this set-oriented formulation of bifurcation analysis of chapter 5 into real world applications, one may need to reconsider nonautonomous dynamical systems instead.
Inspired by chapter 5, we address a characterization of finite-time bifurcations of coherent sets in chapter 6, which emerge from a nonautonomous dynamical system. This has allowed us to deduce finite-time generic early warning signals for sudden vortex splittings. These results are used to spectrally describe and characterize the Antarctic polar vortex splitting event from the recorded velocity data, see figure 1.1. The results in chapter 6 are being prepared for submission to Chaos [60].

2 Dynamical systems and transfer operators

In this chapter, we briefly introduce basic concepts our research will be built on. Indeed, we define autonomous and nonautonomous dynamical systems. In particular, we introduce the notion of ensemble evolution of trajectories, as our main approach can also be classified in the broad range of statistical analysis of deterministic dynamical systems. Thus, infinite dimensional linear operators which maps the evolution of densities will be properly defined as as well. Finally, we introduce the main set-oriented objects that will be at the core of all the ultimately developed frameworks throughout.

2.1 General definition and motivation

The theory of dynamical systems is concerned with the temporal evolution of systems. As a matter of fact, a dynamical system can be used to describe process in motion, to predict the future behavior of the underlying systems. Areas where dynamical systems are relevant include changes in atmospheric flow motions, prediction of climate change from the dynamics of climate models, etc.
A fast mathematical understanding of dynamical system includes thinking the latter as being any semigroup acting on a set. Indeed, a semigroup is simply an algebraic structure made up of a set with an associative binary operation. Let $(G, \star)$ be the semigroup. Thus, the action of G on a set X is defined as a rule which associates to each element $t \in G$ a transformation R^t of X such that the operation $t \star s$ is associated with the composition $R^t \circ R^s$. Therefore, the dynamical system can be modeled as the transformation

$$R : G \times X \to X \quad \text{with} \quad R(t, x) = R^t(x). \tag{2.1}$$

Equation (2.1) models the final state of an initial data $x \in X$ after moving t times, under the transformation $R(t,x)$. That is, if t is considered as a time duration and x as an spatial data, then (2.1) represents the time evolution of data x in the domain X.
A more formal definition is given as follows.

Definition 1 *A dynamical system is a triplet consisting of a set of time $I \in \{\mathbb{R}, \mathbb{N}, \mathbb{Z}\}$, an non-empty topological Hausdorff space X known as the state space or phase space, and a continuous mapping $R : I \times X \to X, \quad (t,x) \mapsto R(t,x)$ known as the rule for evolution with*

$$R(0,x) = x \qquad \forall \quad x \in X \tag{2.2}$$

$$R(s, R(t,x)) = R(s+t,x) \qquad \forall \quad s,t \in I. \tag{2.3}$$

The triplet (I, X, R) is called a *discrete-time* dynamical system if $I \subseteq \mathbb{N}$ or $I \subseteq \mathbb{Z}$ and a *continuous-time* dynamical system if $I \subseteq \mathbb{R}$. Besides, (I, X, R) with the map (2.1) is called an *autonomous* dynamical system, as the knowledge of the final time is enough to understand the evolution of the system, whenever an initial point is given.
Definition 1 can be reformulated by incorporating an explicit initial time. That is, the transformation (2.1) becomes

$$R : I \times I \times X \to X \quad \text{with} \quad R(t,s,x) = R^{s,t}(x). \tag{2.4}$$

and models the final state of an initial data x at initial time s at time t. Moreover, conditions (2.2) and (2.3) become

$$R(s,s,x) = x \qquad \forall \quad x \in X \tag{2.5}$$

$$R(t, R(s,s_0,x)) = R(t,s,x) \qquad \forall \quad s_0, s, t \in I. \tag{2.6}$$

Hence, the quadruplet (I_1, I_2, X, R) where I_1 and I_2 denote, respectively, the set of initial and final times and the transformation in definition (1) is called a *nonautonomous* dynamical system. More details about the mapping (2.4) and the nonautonomous dynamical setting (2.5)-(2.6) will be given later in this chapter.
Now, for the sake of motivation we will focus more on the autonomous dynamical system. Given an initial point $x \in X$ and the autonomous dynamical system with the flow map (2.1), the set of points $\mathcal{O}_x = \{R(t,x)\ t \in I\}$ is called *orbit* or *trajectory* of x. In this setting, one may be interested in the time evolution of an individual orbit $\mathcal{O}_x$. In this case,

the asymptotic behavior of $\mathcal{O}_x$ may be investigated. Alternatively, a more macroscopic approach may be considered by studying the collective behavior of a swarm of initial points. That is, given $\{x_1, x_2, ..., x_N\} \subset X$, we can then seek to understand the global behavior of the set of trajectories $\{\mathcal{O}_{x_1}, \mathcal{O}_{x_2}, ..., \mathcal{O}_{x_N}\} \subset X$. The latter approach is very suitable in some contexts. For instance, the need to understand and/or predict the changes of behavior of ocean eddies or atmospheric vortices, which emerge from ocean or atmospheric dynamics, may leave us with no other choice than to consider the collective behavior of the systems dynamics. In addition, depending on the nature of the dynamics, say chaotic, it may be easier to study the fate of an ensemble of trajectories instead of a single trajectory $\mathcal{O}_x$. Indeed, two initial data whose spacial positions may be very close tend to diverge quickly as time runs forward.

In this study, we aim to understand the change in behavior of sets of ensemble of points (or a clusters of points) that are fixed or move in time together with minimum dispersion with respect to the flow map. This can be referred to a set-oriented approach. Hence, this set-oriented approach may be view as an sufficient pretext to analyze the underlying dynamical system from an ensemble evolution of trajectories approach.

In this pace, given the initial points $\{x_1, x_2, ..., x_N\}$, we can associate the probability density function $\rho_0(x) = \frac{1}{N}\sum_{i=1}^{N} \delta(x - x_i)$, where δ denotes the Dirac distribution, $\frac{1}{N}$ is the probability associated to each value x_i, $i = 1, \cdots, N$. Thus, ρ_0 is a well-defined probability density function, given $\rho_0(x) \geq 0$ and $\int_X \rho_0(x)dx = 1$. Now we define a smooth observable $g : X \to \mathbb{R}$. The value of the observable g at time t is denoted by $\langle g \rangle_t$ and is given by

$$\begin{aligned} \langle g \rangle_t &= \frac{1}{N}\sum_{i=1}^{N} g(R^t(x_i))\delta(x - x_i) = \int_X g(R^t(x))\rho_0(x)dx \\ &= \int_{R^t(X)} g(y)\rho_0(R^{-t}(y)) \left|\det J(R^{-t})(y)\right| dy, \end{aligned} \tag{2.7}$$

where $J(f)$ denotes the Jacobian matrix of partial derives of f and the transformation R^t is supposed to be differentiable and invertible, for simplicity. Note that $\left|\det J(R^t)(y)\right| = 1$, if the transformation R^t is area preserving, which is a characteristic of incompressible fluid flows. On the other hand, let ρ_t be the probability density function of the image points $\left\{R^t(x_1), R^t(x_2), ..., R^t(x_N)\right\}$ at time t. Thus, we have

$$\langle g \rangle_t = \int_{R^t(X)} g(y)\rho_t(y)dy \tag{2.8}$$

and it follows that

$$\begin{aligned}\rho_t(y) &= \frac{\rho_0(R^{-t}(y))}{|\det J(R^t)(y)|} \\ &= \int_X \delta(x - R^t(y))\rho_0(x)dx.\end{aligned} \tag{2.9}$$

Therefore, given the ensemble evolution of trajectories, the corresponding probability density functions are transported in a linear fashion. This is very important in the sense that, even though the evolution of trajectories may be non-linear, the evolution of corresponding density functions is linear as shown in (2.9). Thus, given the initial density ρ_0, we have then a trajectory of densities $\{\rho_t,\ t \geq 0\}$ that evolves linearly over time. One may think of the stochastic kernel $k(x, y) := \delta(x - R^t(y))$ as a matrix with indices (x, y) and index summation in matrix multiplication replaced by the integral over $Y := R^t(X)$. Therefore, the linear relation between ρ_0 and ρ_t may be mathematically formulated via an infinite dimensional operator L^t such that (2.9) becomes

$$\rho_t = L^t\rho_0. \tag{2.10}$$

Alternatively, the operator L^t in (2.10) could emerge from the nonautonomous setting (2.5)-(2.6) and denoted by $L^{(s,t)}$. In this case, the finite time evolution of densities within the time interval $[s, t]$ can modeled as

$$\rho_t = L^{(s,t)}\rho_s. \tag{2.11}$$

That is, even if a linear relation between densities is preferable to a non-linear evolution of trajectories, one may pay the cost of dealing with an infinite dimensional operator. Besides, linear infinite dimensional operators are particularly important when we can exploit their spectral features and use them to analyze statistical properties of the dynamical system, for instance. By spectral features, we mean a discrete set of eigenfunctions and their eigenvalues or singular values and their singular functions. Then, relation between the nonlinear flow map R^t and the linear operator L^t yields a connection between qualitative properties of a (finite time) dynamical system including bifurcation, ergodicity, etc., and the spectral theory of infinite dimensional operators, as Koopman [26] and von Neumann [27] firstly noticed.

Throughout this work, however, we will be investigating changes of magnitude of the discrete spectra of (2.10) and (2.11) with respect to changes in the dynamics of their corresponding dynamical systems (2.2)-(2.3) and (2.5)-(2.6), respectively. In particular,

with the operator (2.10), we will be targeting special densities $\mathbf{1}_A,\ \ A \subset X$ such that

$$L^t \mathbf{1}_A \approx \mathbf{1}_A. \tag{2.12}$$

and, with the operator (2.11), we will be seeking densities $\mathbf{1}_A,\ \ A \subset X$ and $\mathbf{1}_B,\ \ B \subset R(s,t,X)$ such that

$$L^{(s,t)} \mathbf{1}_A \approx \mathbf{1}_B. \tag{2.13}$$

Equation (2.12) may be interpreted as a functional characterization of the notion of *almost-invariance* of the set A, while equation (2.13) yields a functional representation of the notion of *coherence* of the sets A and B. Indeed, note that densities $\mathbf{1}_A$ and $\mathbf{1}_B$ are supported in A and B, respectively. Thus, in (2.12), we can say that the autonomous dynamics leaves the set A almost-invariant, whereas in (2.13), the nonautonomous dynamics carries the set A coherently to the set B in the sense that the set A is mapped to the set B by the nonautonomous flow. In addition, equations (2.12) and (2.13) may be cast in more general eigenequations for the operators L^t and $L^{(s,t)}$, respectively. Therefore, we can already notice that there may be an interdependency between finding almost-invariant/coherent objects and solving eigenequations of the infinite dimensional operators L^t and $L^{(s,t)}$. Note that with the operation $L^{(s,t)}$, we might want to solve a singular value decomposition problem, as $\mathbf{1}_A$ and $\mathbf{1}_B$ may be very different functions. Nevertheless, the spectral idea to finding these sets remains there. A set-oriented dynamical system consists of analyzing the behavior of system in the whole phase space with a special aim of computing and analyzing those sets. Thus, almost-invariant/coherent sets are the main objects on which our work will be based throughout this thesis. However, note that we have only partly introduced almost-invariance/coherence notions, since equations (2.12) and (2.13) only yield necessary conditions for finding these objects from a probabilistic approach. In the following, we concretely introduce the systems our study will be based on as well as mathematical definitions of basic concepts including almost-invariance/coherence.

2.2 Dynamical systems and transfers operators

We are mainly interested in continuous time processes generated by solutions of ordinary differential equations. Thus, we will define infinite dimensional linear operators generated from the time evolution of these processes. Throughout this work, we will consider

a continuous time interval $\mathbb{I} \subset \mathbb{R}$ and a measure space $D \subset \mathbb{R}^d$. Let $X \subset D$.

2.2.1 Dynamical systems

An autonomous ordinary differential equation (ODE) is given by

$$\frac{dx}{dt} =: \dot{x} = F(x), \tag{2.14}$$

where $F\colon X \to X$ is called the velocity field of (2.14) and is assumed to be smooth. Let $x\colon \mathbb{I} \to X$ be continuously differentiable. Thus, the function x is said to solve (2.14) if $\dot{x}(t) := \frac{dx}{dt} = F(x(t))$ for all $t \in \mathbb{I}$. Moreover, if the initial condition $x(t_0) = x_0$ is coupled with the equation (2.14), then (2.14) is referred to as an initial value problem. Thus, a solution x solves the initial value problem if $x(t_0) = x_0$ and $\dot{x}(t) = F(x(t))$. That is, if we assume global existence and uniqueness of the solutions, then the latter form a mapping

$$(t, t_0, x_0) \mapsto x(t, t_0, x_0), \ \forall \ (t, t_0, x_0) \in \mathbb{I} \times \mathbb{I} \times X \tag{2.15}$$

and are called general solution of (2.14). Adding an initial condition to (2.14) makes the problem simpler in the sense that, once a solution is found, it is translation invariant in time. That is, only the duration matters since starting, which means that the solutions depend only on the elapsed time $t - t_0$ since starting and not separately on the actual time t and the starting time t_0. Hence the solution mappings satisfy the relation

$$x(t - t_0, 0, x_0) = x(t, t_0, x_0), \ \forall \ (t_0, x_0) \in \mathbb{I} \times X. \tag{2.16}$$

Indeed, let $s_1(t) = x(t, t_0, x_0)$ and $s_2(t) = x(t - t_0, 0, x_0)$. Then we have $s_1(t_0) = s_2(t_0) = x_0$. Moreover, we have

$$\begin{aligned} \frac{d}{dt} s_2(t) &= \frac{d}{dt} x(t - t_0, 0, x_0) = \frac{\partial x}{\partial t}(t - t_0, 0, x_0) \cdot \frac{d}{dt}(t - t_0) \\ &= F(x(t - t_0, 0, x_0)) = F(s_2(t)), \end{aligned}$$

which concludes that both $s_2(t)$ and $s_1(t)$ satisfy the same initial value problem. Hence by the uniqueness assumption, we have $s_1(t) = s_2(t)$.
As a matter of fact, we can restrict the initial time to $t_0 = 0$ and write the solutions

(2.15)-(2.16) as $x(t, x_0)$. Furthermore, the solution mapping

$$\begin{aligned} \phi &: \mathbb{I} \times X \to X \\ &(t, x_0) \mapsto \phi(t, x_0) \end{aligned} \tag{2.17}$$

with $\phi^t(x_0) \equiv \phi(t, x_0) := x(t, x_0)$, is continuous in both variables and fulfills the initial value condition

$$\phi(0, x_0) = x_0, \ \ \forall \ \ x_0 \in X$$

and the group property

$$\phi(s + t, x_0) = \phi(s, \phi(t, x_0)), \ \ \forall \ \ s, t \in \mathbb{I} \ \text{ and } \ x_0 \in X.$$

The latter relation is a direction consequence of uniqueness of solutions. As, a consequence, the mapping (2.17) is special case of an autonomous dynamical system as defined in (2.1). One can, thus, see that from an autonomous ODE (2.14) and its solutions (2.15)-(2.16), an autonomous dynamical system can be defined and studied by tracking the time evolution of the the flow map (2.17), via group property formulation. However, the latter is only possible due to the translation invariant of the solutions (2.15) of (2.14). This means, autonomous dynamical systems do not depend separately on initial time t_0 and final time t.
The opposite occurs for nonautonomous systems, since both initial and final times are important rather than the elapsed time $t - t_0$. Hence, a generalization of the group property above is a two-parameter group property where both t_0 and t are parameters, which also referred to as a process of a nonautonomous dynamical system [59]. Let

$$\begin{aligned} \dot{x} &= F(t, x) \\ x(t_0) &= x_0 \end{aligned} \tag{2.18}$$

be the time-dependent extension of the ordinary equation (2.14). Let us assume existence and uniqueness of solutions in forward time. Then, the solutions form a continuous mapping $(t, t_0, x_0) \mapsto x(t, t_0, x_0) \in X$ satisfying the initial value condition (i) $x(t_0, t_0, x_0) = x_0$ and the evolution property (ii) $x(t_2, t_0, x_0) = x(t_2, t_1, x(t_1, t_0, x_0))$, for all $t_0 \leq t_1 \leq t_2$ in $\mathbb{I}$ and $x_0 \in X$. The principle in which solutions are uniquely determined by their initial values justifies the property (ii). A process can, thus, be defined as a continuous mapping

$$\begin{aligned}\phi\colon \mathbb{I}\times\mathbb{I}\times X &\to X\\ (t,t_0,x_0) &\mapsto \phi(t,t_0,x_0),\end{aligned} \tag{2.19}$$

which satisfies the initial value (i) and the evolution property (ii). Later in this work, we may write $\phi_{t_0}^t$ in place $\phi(t,t_0,\cdot)$ and vice versa, and the same will apply to the autonomous flow map. Regarding the inverse flow maps, we may choose to work with $\left(\phi_{t_0}^t\right)^{-1}$ in place of $\phi(t_0,t,\cdot)$ and vice versa, and the same will apply to the autonomous flow map. For more details about process formulations and nonautonomous dynamical systems, we refer the reader to [59].

In order to study the (finite) time evolution of a finite number of initial points $\left\{x_0^{(i)},\, i=1,...,N\right\}$ over time, one may think of considering a statistical evolution of the autonomous/nonautonomous deterministic dynamical system through its flow map (2.17) or (2.19). With this approach it helps to define a measure space environment, since investigating the (finite) time evolution of an initial density of the distribution of the initial points $\left\{x_0^{(i)},\, i=1,...,N\right\}$ may be simpler and more rewarding in many ways. Indeed, we could then study infinite dimensional linear operators whose spectra are suitable for set-oriented dynamical systems. This is in fact, the importance of the next section.

2.2.2 Transfer operators

Let (X,Σ_X,μ) be a measure space and let $\mathcal{D}=\left\{\rho\in L^1(X,\Sigma_X,\mu):\ \rho\geq 0\ \text{ and }\ \|\rho\|_1=1\right\}$. Note that to any measure space (X,Σ_X,μ), one can associate the Banach spaces $L^p(X,\Sigma_X,\mu)=\left\{\rho: X\to\mathbb{R}:\ \rho\ \text{ is measurable and }\ \int_X|\rho|^p d\mu<\infty\right\},\ \ p\geq 1$. Moreover, for any $\rho\in L^p\equiv L^p(X,\Sigma_X,\mu),\ \ \|\rho\|_p=\left(\int_X|\rho|^p d\mu\right)^{1/p}$ denotes the L^p norm of $\|\rho\|_p$. A transformation $R:X\to X$ is measurable if $R^{-1}(A)\in\Sigma_X$ for all $A\in\Sigma_X$.

We suppose that, for a fixed time $t\in\mathbb{I}$, the mapping $\phi^t\colon X\to X$ defined in (2.17) is a non-singular measurable transformation. That means, $\mu(\left(\phi^t\right)^{-1}(A))=0$, whenever $\mu(A)=0$ for all $A\in\Sigma_X$. The latter is immediately verified for measure preserving transformations which are flow maps generated by ODEs that model the dynamics of incompressible fluid flows. The *Frobenius-Perron operator* $P^t\colon L^1(X,\Sigma_X,\mu)\to L^1(X,\Sigma_X,\mu)$ with respect to the flow $\phi^t,\ t\in\mathbb{I}$ is uniquely defined [49] by the mass conservation relation

$$\int_A P^t\rho d\mu=\int_{(\phi^t)^{-1}(A)}\rho d\mu,\ \ \forall\ A\in\Sigma_X. \tag{2.20}$$

Moreover, it straightforward to show that the operator P^t satisfies the following relations
(a) $P^t\left(a_1\rho_1 + a_2\rho_2\right) = a_1P^t\rho_1 + a_2P^t\rho_2$
(b) $P^t\rho \geq 0$ if $\rho \geq 0$
(c) $\int_X P^t\rho d\mu = \int_X \rho d\mu$.
Hence, the Frobenius-Perron operator P^t, $t \geq 0$ is a linear operator, positive and maps probability densities in $\mathcal{D}$ to probability densities in $\mathcal{D}$. Furthermore, P^t, $t \geq 0$ has a dual operator called the *Koopman operator* K^t: $L^\infty(X, \Sigma_X, \mu) \to L^\infty(X, \Sigma_X, \mu)$ defined by $K^t g = g \circ \phi^t$, where the functions g are smooth and are called observables. The dynamical difference between P^t, $t \geq 0$ and K^t, $t \geq 0$ is that the former pushes densities forward under the evolution of the underlying dynamics, while the latter pulls backward observables. Due to the one-to-one property of the flow map (2.17), the explicit formula of P^t is given by

$$P^t\rho_0(y) = \frac{\rho_0\left(\left(\phi^t\right)^{-1}(y)\right)}{\left|\det J\left(\phi^t\right)(y)\right|}, \tag{2.21}$$

where ρ_0 the initial density of the initial points $\left\{x_0^{(i)},\, i = 1, ..., N\right\}$. Similarly, the finite time Frobenius-Perron operator $P^{t_0,t}$ related to the flow map (2.19) is given by

$$P^{t_0,t}\rho_0(y) = \frac{\rho_0(\left(\phi_{t_0}^t\right)^{-1}(y))}{\left|\det J\left(\phi_{t_0}^t\right)(y)\right|}, \tag{2.22}$$

A lot of studies have been carried out around these operators, see [49]. In this work, we will intensively use these operators to construct particular measurable sets which are introduced below.

2.3 Basic concepts

Definition 2 (invariance) *A subset M of X is called invariant under the autonomous flow map (2.17) if*

$$\phi(t, M) = M \text{ for all } t \in \mathbb{I}.$$

In autonomous settings, as defined in (2.17), invariant sets characterize the local long-term dynamical behaviors. Thus, simplest examples of invariant sets include equilibria and periodic solutions. An equilibrium point, $\phi(t, x) = x$ for all $t \in \mathbb{I}$, is an invariant set M when M is the singleton $\{x\}$. Periodic solutions can also be referred to as periodic orbit γ where for any $x \in \gamma$, we have $\phi(T + s, x) = \phi(s, x)$ and $\phi(kT, x) = x$ for any

integer k. The latter relations are possible due to the group property of ϕ. Besides, T is called the period of γ as the minimum positive value for which $\phi(T, x) = x$. Thus, γ is an invariant set. In this study, periodic orbits will play a key role in the construction of invariant sets that emerge from the dynamics of incompressible flows. This will be widely detailed in chapter 4.

Let us assume that M is a compact invariant subset of X and the underlying dynamics is incompressible. Then M and $M^c = X \setminus M$ partition the phase space X into two invariant sets. We have, thus, a coexistence of two phase spaces with no transport of flow between them. However, in real-world incompressible dynamics such as ocean or atmospheric dynamics, an invariant partition of phase space is not possible. Indeed, interesting objects include sets that move with minimum transport through there boundaries. Examples include ocean eddies. Motivated by practical examples, this work will deal with almost-invariant/coherent measurable sets which emerge from the dynamics of incompressible flows. Let us suppose that μ is an invariant probability measure with respect to the flow map (2.17). That is, $\mu(\phi^{-t}(A)) = \mu(A) \ \forall \ A \in \Sigma_X$. As a consequence, μ is automatically nonsingular. Invariant measures in set-oriented autonomous dynamics are fixed with respect to the flow map. Thus, they are relevant to represent mass distribution of fixed macroscopic objects, as the underlying dynamics is fixed in time.

Definition 3 (Almost-invariance) *A measurable set $A \subset X$ is said to be an almost-invariant set with respect to μ if*

$$\frac{\mu(A \cap \phi(-t, A))}{\mu(A)} \approx 1. \tag{2.23}$$

Definition 2.23 states that the probability to leave the set A in t time steps is very low. In other words, the set of points that are currently in A and will stay in A after t time steps is large relative to A in the sense of the μ-measure. The almost-invariant set A partitions the phase space into A and $A^c = X \setminus A$ such that both A and A^c satisfy definition 3. Later in chapter 3, we will seek balanced and maximal almost-invariant sets. That is, measurable sets of interest should be balanced in the sense that $\mu(A) = \mu(A^c)$ and dominant among other sets. Thus, we say that $\{A, A^c\}$ is a pair of almost-invariant sets, whenever A and A^c each satisfies (2.23) and $\mu(A) = \mu(A^c)$. Moreover, we will see in chapter 3 that equation (2.23) is, in a functional level, equivalent to equation (2.12) and finding and computing pair of optimal almost-invariant sets will require solving a functional optimization problem.

Given the nonautonomous dynamical system with the flow map (2.19) and inspired by definition 3 in the autonomous setting, we can ask for finding measurable partitions $X_1 \cup X_2 = X$ and $Y_1 \cup Y_2 = Y := \phi(t, t_0, X)$ so that

$$\begin{aligned} Y_1 \approx \phi(t, t_0, X_1) \quad &\text{and} \quad Y_2 \approx \phi(t, t_0, X_2) \quad \text{with} \\ \mu(X_1) = \nu(Y_1) \quad &\text{and} \quad \mu(X_2) = \nu(Y_2). \end{aligned} \tag{2.24}$$

These separate both the initial and image phase spaces into two regions with minimal transport between them. Note that the measure μ is transformed, via the flow map (2.19), to a final measure ν, which is supported on the corresponding measure space (Y, Σ_Y, ν). That is, $\nu(A) = \mu \circ \phi(t_0, t, A),\ \forall\ A \in \Sigma_Y$. Moreover, the measure ν represents the mass distribution of objects of interest at time t. With the time-dependent setting (2.18), note that the measure μ does not need to be necessarily invariant. In the following is given a more formal definition regarding set relations in (2.24).

Definition 4 (Coherence) *$\{A, B\}$ is a pair of coherent sets, whenever*

$$\frac{\mu(A \cap \phi(t_0, t, B))}{\mu(A)} \approx 1 \ \textit{and}\ \ \mu(A) = \nu(B). \tag{2.25}$$

Definition 4 states that the conditional probability of a point initially in $A \subset X$ to be mapped forward into $B \subset Y$ at time t is very high. Moreover, the measurable sets $\{X_1, Y_1\}$ and $\{X_2, Y_2\}$ in (2.24) are pairs of coherent sets.
Coherent sets are optimal regions that resist mixing with their surroundings over a finite time span, while almost-invariant sets are fix optimal regions that asymptotically resist mixing [13–16, 36]. The former emerge from a nonautonomous dynamical system (2.19), while the latter exist when an autonomous dynamical system (2.17) is considered.
Given that $\mathbf{1}_{X_k}$ is a functional representation of X_k, $k = 1, 2$ and $\mathbf{1}_{Y_k}$ is the functional representation of Y_k, $k = 1, 2$, relations in (2.24) can be reproduced in a functional manner. For this we need a suitable linear operator [16] so that our goal will finally consist of the following

Goals 5

1. $L\mathbf{1}_{X_k} \approx \mathbf{1}_{Y_k}$.
2. $\mu(X_k) = \nu(Y_k),\ k = 1, 2.$

Therefore, the mapping $\phi(t, t_0, X_k)$ may be operator-wise viewed as the functional mapping $L\mathbf{1}_{X_k}$. This intuitively makes sense since we are interested in tracking the evolution of densities that represent the distribution of initial data. Note that the constraint in goals 5(2) means that there is no loss of mass under the dynamics, while mapping X_k to its image Y_k, under the action of L or the flow $\phi(t, \cdot, \cdot)$. However, the operator L should be specified and understood, which requires a particular setting where L can be gradually constructed. For the moment, one may notice that the operator L, restricted in goals 5(1), satisfies equation (2.13). That is, L must be built using flow map information with a functional approach. That is equivalent to think of building L from the Frobenius-Perron operators in (2.21) and (2.22) which do not always satisfy goals 5(1). A mathematical framework for constructing the operator L in both autonomous and nonautonomous dynamical systems and for finding optimal almost-invariant/coherent sets will be carried out in chapter 3.

2.4 Summary

This chapter has served as a brief introduction of dynamical systems and transfer operators concepts, which will be heavily used throughout this work. There is a broad literature about these mathematical tools but it is always necessary to introduce key concepts in order to align with traditional scientific methods. Finally, precise definitions of the notions of almost-invariant/coherent sets were given. These sets are the main dynamical objects we are interested in throughout this thesis. That is why an early understanding of these concepts is necessary.

3 Diffused transfer operators, set-oriented dynamics

In this chapter we give a detailed construction process of robust coherent sets as well as almost-invariant sets. Robust coherent sets are those that exhibit robustness under external perturbations. They are, thus, suitable to mathematically model transporters of mass, given the dynamics of a complex system such as the ocean/atmospheric circulation. In fact, coherent sets can numerically simulate ocean eddies, which are good transporters of water that is warmer/cooler/saltier than the surrounding water. Hence, coherent sets can, for instance, very well contribute to change the temperature of the area of their destinations, according to ocean flow direction. The approach that we follow is analytic and is, firstly, based on perturbed infinite dimensional linear operators which are built around transfer operators (2.21) and (2.22) introduced in chapter 2.

3.1 Singuar vectors for compact operators

3.1.1 Operator setting

Let $L\colon X \to Y$ be a compact linear mapping between two Hilbert spaces. Let $Q = L^*L\colon X \to X$ with L^* the dual of L. Hence, Q is compact, self-adjoint, and positive, i.e., $\langle Qx, x\rangle_X \geq 0$. As a consequence, Q has a non-negative spectrum ordered as $\lambda_1 \geq \lambda_2 \geq \cdots \geq 0$. Therefore, by the spectral theorem for compact and self-adjoint operators ([61], Theorem II.5.1), we can find an orthonormal basis of eigenvectors, $u_k \in X,\ Qu_k = \lambda_k u_u$, so that

$$Q = \sum_{k=1}^{N} \lambda_k \langle \cdot, u_k\rangle_X u_k \tag{3.1}$$

Note that N may be finite or infinite.
It follows, thus, the minimax principle ([62], Theorem 9.2.4, p212) :

Theorem 6

$$\lambda_k = \min_{V:\operatorname{codim} V \leq k-1<N} \max_{0\neq x\in V} \frac{\langle Qx, x\rangle_X}{\langle x, x\rangle_X},\ k = 1, ..., N. \tag{3.2}$$

Furthermore, the maximizing x's are the u_k, $k = 1, ..., N$.

On the other hand, we have that the transformation

$$\frac{\langle Qx, x\rangle_X^{1/2}}{\langle x, x\rangle_X^{1/2}} = \frac{\langle Lx, Lx\rangle_Y^{1/2}}{\|x\|_X} = \frac{\|Lx\|_Y}{\|x\|_X} = \max_{0\neq y\in Y} \frac{\langle Lx, y/\|y\|_Y\rangle_Y}{\|x\|_X},$$

solves the optimization problem

$$\sigma_k := (\lambda_k)^{1/2} = \min_{V:\operatorname{codim} V \leq k-1<N} \max_{0\neq x\in V, 0\neq y\in Y} \frac{\langle Lx, y\rangle_X}{\|x\|_X\|y\|_Y},\ k = 1, ..., N, \tag{3.3}$$

where we call the maximizing units x and y in (3.3) the left and right singular vectors of L, respectively. Moreover, σ_k are the corresponding singular values of L.
One can easily observe that the compactness property of the linear operators L and the existence of inner products were only used to arrive at a singular value decomposition (SVD) in an operator level. Recall that our goal is to find coherent sets, given a nonautonomous dynamical system between measurable phase spaces. Therefore, we will see that constructing compact operators from the underlying dynamical systems and choosing appropriate Hilbert spaces will lead to finding a SVD that will systematically yield coherent partitions of the phase spaces.

3.1.2 SVD of matrices

To fix understanding, it is important to have in mind that the set-oriented analysis of the dynamical systems (2.17) and (2.19) will eventually lead to a spectral analysis of

matrices $\mathcal{M} \in \mathbb{R}^{n\times m}$:

$$\mathcal{M} = \begin{pmatrix} \mathcal{M}_{11} & \mathcal{M}_{12} & \cdots & \mathcal{M}_{1m} \\ \mathcal{M}_{21} & \mathcal{M}_{22} & \cdots & \mathcal{M}_{21} \\ \vdots & \vdots & \ddots & \vdots \\ \mathcal{M}_{n1} & \mathcal{M}_{n2} & \cdots & \mathcal{M}_{nm} \end{pmatrix}, \quad k > 2. \tag{3.4}$$

The state space of the system is, thus, subdivided in to smaller sub-states and the entries $\mathcal{M}_{ij} \neq 0$, $i = 1, ..., n$, $j = 1, ..., m$ correspond to transition probabilities between states. In other words, the conditional probability of the flow map to land in a sub-state j given that it was initially in the sub-state i yields the entry $\mathcal{M}_{ij}$. This will be more explicit in chapter 5 and chapter 6. Therefore, depending on the nature of the dynamics in phase space, $\mathcal{M}$ is vertical and tall when $n \gg m$, horizontal and short when $n \ll m$. For instance, $n \gg m$ may corresponds to a contraction where the flow (2.19) maps all the initial data together into a smaller region in the image phase space. The case $n \ll m$ may correspond to an expansion where all the initial data are mapped to wider region within the image phase space. Given the time dependent flow (2.19), the matrix $\mathcal{M}$ is mainly used to determine input and output numerically approximated coherent clusters of sub-states under the finite time dynamics. Further details about the matrix $\mathcal{M}$ will be given later in this study. Finally, $\mathcal{M}$ can be non-uniquely decomposed as

$$\mathcal{M} = U\Sigma V^{\intercal}, \tag{3.5}$$

where $U \in \mathbb{R}^{n\times n}$ and $V \in \mathbb{R}^{m\times m}$ are unitary matrices. That is to say that $UU^{\intercal} = U^{\intercal}U = I_n$ and $VV^{\intercal} = V^{\intercal}V = I_m$ with I_n and I_m being the identity matrices. The matrix Σ is diagonal and the diagonal entries $\sigma_i = \Sigma_{ii}$ are called singular values of $\mathcal{M}$. The number of non-zero diagonal entries determine the rank of $\mathcal{M}$. Equation (3.5) is known as the SVD of $\mathcal{M}$ and vectors U and V are called left and right singular vectors, respectively. The SVD is well known to be relevant in extracting dominant patterns from a low dimensional approximation given a high dimensional data. This is the so called principal component analysis (PCA). The SVD can also be systematically used to extract dominant coherent patterns given a matrix of data which is generated from the finite time evolution of a dynamical system. The SVD is actually a data-driven method since it can help detect qualitatively relevant features, given complicated set of data. In this study our first task will always consist of finding dominant coherent patterns, given singular vectors obtained from (3.5). In the following, we will elaborate more on the different steps towards connecting the underlying dynamical systems, the transfer operators, the SVD,

and also the eigenvalue value decomposition. In other words, the matrix (3.4) will later be more specified as a finite dimensional approximation of compact operators. Note that the SVD is convenient when studying nonautonomous dynamical systems, see chapter 6. Furthermore, for an autonomous dynamical system, a square matrix will approximate the autonomous transfer operators and, instead of SVD, eigenvalue decomposition will yield almost-invariant patterns, see chapter 5.

3.1.3 Compact linear operators, coherent partitions

Now, we specify our setting by taking the Hilbert spaces $L^2(X, \Sigma_X, \mu)$ and $L^2(Y, \Sigma_Y, \nu)$ and a transfer operator

$$L\colon L^2(X, \Sigma_X, \mu) \to L^2(Y, \Sigma_Y, \nu). \tag{3.6}$$

Note that the measurable spaces X and Y are now different from the Hilbert spaces X and Y in the previous section. Let $\langle \cdot, \cdot \rangle_\mu$ and $\langle \cdot, \cdot \rangle_\nu$ denote the standard inner products of $L^2(X, \Sigma_X, \mu)$ and $L^2(Y, \Sigma_Y, \nu)$, respectively. Under the following assumptions:

Assumption 7
1. $(Lf)(y) = \int k(x, y) f(x) d\mu(x)$ *where* $K \in L^2(X \times Y, \Sigma_X \times \Sigma_Y, \mu \times \nu)$ *is non-negative,*
2. $L\mathbf{1}_X = \mathbf{1}_Y$, *equivalently* $\int k(x, y) d\mu(x) = 1$ *for* $\nu-$ *a.a* y,
3. $L^*\mathbf{1}_Y = \mathbf{1}_X$, *equivalently* $\int k(x, y) d\nu(y) = 1$ *for* $\mu-$ *a.a* x,

it is proven in [16] that both operators L and L^* are compact, the largest singular value of L is $\sigma_1 = 1$ and is simple (i.e., of multiplicity one) with $\mathbf{1}_X$ and $\mathbf{1}_Y$ the respective associated left and right singular vectors, and the second singular value σ_2 satisfies

$$\sigma_2 = \max_{f \in L^2(X, \Sigma_X, \mu),\, g \in L^2(Y, \Sigma_Y, \nu)} \left\{ \frac{\langle Lf, g \rangle_\nu}{\|f\|_\mu \|g\|_\nu} : \langle f, \mathbf{1}_X \rangle_\mu = \langle g, \mathbf{1}_Y \rangle_\nu = 0 \right\} < 1. \tag{3.7}$$

Besides, the maximizing f and g of (3.7) are u_2 and $\frac{Lu_2}{\|Lu_2\|}$, respectively. The latter are the respective left and right singular vector of L corresponding to the singular σ_2.
The square integrability of the stochastic kernel k in assumption 7(1) ensures compactness of L and L^*, which also ensures that the spectrum of the operator $Q = L^*L$ located far from the origin is discrete. In addition, the non-negativity of k is set to make sure that Lf represents mass distribution with respect to ν, whenever f represents some distribution

of mass with respect to μ. As $\mathbf{1}_X$ represents the density function of the measure μ and $\mathbf{1}_Y$ represents the density function of the measure ν, then assumption 7(2) requires $\mathbf{1}_X$ to be mapped to $\mathbf{1}_Y$ by L. From assumption 7(3), one can easily prove that L preserves integrals.

Therefore, assumption 7(1-3) yields necessary conditions to have a meaningful discrete spectrum of L. Moreover, it provides an intuitive understanding of what the operator L should look like, given an ultimate explicit nonautonomous dynamics.

Using only results from assumption 7 including (3.7) and the targeted goals in 5, it is shown in [16] that

$$\max_{X_1\cup X_2=X,\, Y_1\cup Y_2=Y} \left\{ \frac{\langle L\mathbf{1}_{X_1}, \mathbf{1}_{Y_1}\rangle_\nu}{\mu(X_1)} + \frac{\langle L\mathbf{1}_{X_2}, \mathbf{1}_{Y_2}\rangle_\nu}{\mu(X_2)} \right\} \leq 1 + \sigma_2 \tag{3.8}$$

Indeed, it all starts from solving the optimization problem

$$\begin{aligned} \textbf{(P)} \max_{X_1\cup X_2=X,\, Y_1\cup Y_2=Y} \Bigg\{ \Bigg\langle L\left(\sqrt{\frac{\mu(X_2)}{\mu(X_1)}}\mathbf{1}_{X_1} - \sqrt{\frac{\mu(X_1)}{\mu(X_2)}}\mathbf{1}_{X_2}\right), \sqrt{\frac{\nu(Y_2)}{\nu(Y_1)}}\mathbf{1}_{Y_1} - \\ \sqrt{\frac{\nu(Y_1)}{\nu(Y_2)}}\mathbf{1}_{Y_2}\Bigg\rangle_\nu : \mu(X_k) = \nu(Y_k),\ k = 1, 2. \Bigg\}, \end{aligned} \tag{3.9}$$

where $\langle LU_X, V_Y\rangle_\nu$ with $U_X = \sqrt{\frac{\mu(X_2)}{\mu(X_1)}}\mathbf{1}_{X_1} - \sqrt{\frac{\mu(X_1)}{\mu(X_2)}}\mathbf{1}_{X_2}$ and $V_Y = \sqrt{\frac{\nu(Y_2)}{\nu(Y_1)}}\mathbf{1}_{Y_1} - \sqrt{\frac{\nu(Y_1)}{\nu(Y_2)}}\mathbf{1}_{Y_2}$ is the objective function and $\mu(X_k) = \nu(Y_k),\ k = 1, 2$ is the constraint. The latter agrees with goals 5(2). Hence, given the constraint, it is straight forward to rewrite the objective function as

$$\langle LU_X, V_Y\rangle_\nu = \frac{\langle L\mathbf{1}_{X_1}, \mathbf{1}_{Y_1}\rangle}{\mu(X_1)} + \frac{\langle L\mathbf{1}_{X_2}, \mathbf{1}_{Y_2}\rangle}{\mu(X_2)} - 1. \tag{3.10}$$

That is, the set-based optimization (3.9) becomes

$$\textbf{(P)} \max_{X_1\cup X_2=X,\, Y_1\cup Y_2=Y} \left\{ \frac{\langle L\mathbf{1}_{X_1}, \mathbf{1}_{Y_1}\rangle}{\mu(X_1)} + \frac{\langle L\mathbf{1}_{X_2}, \mathbf{1}_{Y_2}\rangle}{\mu(X_2)} - 1 :\ \ \mu(X_k) = \nu(Y_k),\ k = 1, 2 \right\}. \tag{3.11}$$

As a consequence, a strongly possible way to achieve the goals 5 is to solve the problem (3.9) which is just problem (3.11). Moreover, given that $\|U_X\|_\mu = \|V_Y\|_\nu = 1$ and

$\langle U_X, \mathbf{1}\rangle_\mu = \langle V_Y, \mathbf{1}\rangle_\nu = 0$, then problem

$$\textbf{(RP)} \max_{f\in L^2(X,\Sigma_X,\mu),\, g\in L^2(Y,\Sigma_Y,\nu)} \left\{ \frac{\langle Lf, g\rangle_\nu}{\|f\|_\mu \|g\|_\nu} : \langle f, \mathbf{1}_X\rangle_\mu = \langle g, \mathbf{1}_Y\rangle_\nu = 0 \right\}$$

is a relaxed version of the problem

$$\max_{X_1\cup X_2 = X,\, Y_1\cup Y_2 = Y} \langle LU_X, V_Y\rangle_\nu.$$

We, thus, have the following:

$$\begin{aligned} \textbf{(P)} &\leq \max_{X_1\cup X_2 = X,\, Y_1\cup Y_2 = Y} \langle LU_X, V_Y\rangle_\nu \\ &\leq \max_{f\in L^2(X,\Sigma_X,\mu),\, g\in L^2(Y,\Sigma_Y,\nu)} \left\{ \frac{\langle Lf, g\rangle_\nu}{\|f\|_\mu \|g\|_\nu} : \langle f, \mathbf{1}_X\rangle_\mu = \langle g, \mathbf{1}_Y\rangle_\nu = 0 \right\} \end{aligned}$$

That is

$$\max_{X_1\cup X_2 = X,\, Y_1\cup Y_2 = Y} \left\{ \frac{\langle L\mathbf{1}_{X_1}, \mathbf{1}_{Y_1}\rangle}{\mu(X_1)} + \frac{\langle L\mathbf{1}_{X_2}, \mathbf{1}_{Y_2}\rangle}{\mu(X_2)} : \ \mu(X_k) = \nu(Y_k),\ k = 1, 2 \right\} \leq 1 + \textbf{(RP)}. \tag{3.12}$$

One can, therefore, see that (3.12) is simply (3.8).
The relaxed problem **(RP)** can be easily solved in reality, given that a numerical approximation of L is available. That requires an explicit operator L whose approximation yields a matrix similar to (3.4). Then the SVD (3.5) can be computed and dominant left and right singular vectors (f_2, g_2) with corresponding singular value σ_2 are systematically used to approximate the coherent partitions $(X_k, Y_k)\,,\ k = 1, 2$. Indeed, a heuristic approach consists of creating coherent partitions $\{X_1, X_2\}$ of X and $\{Y_1, Y_2\}$ of Y by choosing thresholds a and b such that $\mu(X_k) = \nu(Y_k),\ k = 1, 2$. Then, as performed in [15], partitions are built from the following classification:

$$X_1 = \{f_2 > a\}\,,\ X_2 = \{f_2 < a\} \quad \text{and} \quad Y_1 = \{g_2 > b\}\,,\ Y_2 = \{g_2 < b\}\,.$$

Thus, given that $\sigma_2 \approx 1,\ (X_k, Y_k)$ is a pair of coherent sets since $L\mathbf{1}_{X_k} \approx \mathbf{1}_{Y_k},\ k = 1, 2$. In other terms, the relation (2.24) holds. Hence, the nonautonomous flow will then transport X_k to Y_k with minimum dispersion.

Remark 8 *In this study, approximating coherent sets is only the beginning of the work towards understanding qualitative changes of the latter. Indeed, we are interested in*

predicting sudden qualitative changes of coherent sets, as the nonautonomous dynamical system evolves in time. That means, we will be interested in particular coherent partitions which may not be approximated by the second dominant singular vectors but by other singular vectors with smaller magnitude singular value. In other words, we will not restrict ourselves to only finding σ_2 and (f_2, g_2). In fact, the spectral collection of the whole family $\{(f_1, g_1), (f_2, g_2), (f_3, g_3), \cdots, (f_N, g_N)\}$ with $1 \geq \sigma_2 \geq \sigma_3 \geq \cdots \geq \sigma_N,\ N \geq 3$ is necessary for finding the convenient coherent partition to be studied.

3.2 Nonautonomous dynamics, robust coherent sets

Now, we will specify the operator L, given an explicit dynamical system and robustness constraints of coherent sets. A coherent set is robust when it remains coherent under external perturbations. The latter will be explicitly modeled so that a perturbed linear operator, say L_ϵ, satisfying assumption 7 will be derived.

3.2.1 The deterministic setting

Let us consider the nonautonomous flow map $\phi_t^{t+\tau}$ from time t to time $t+\tau$ defined in (2.19) and acting on a compact set $D \subset \mathbb{R}^d$. However, our initial domain of interest will be $X \subset D$ and Y will be its image with respect to the flow. Now, we define a new measure μ in X which has a density $h_\mu \in L^2(X, \ell)$ with respect to the Lebesgue measure, i.e, $h_\mu = \frac{d\mu}{d\ell}$. The new measure μ may be interpreted as the mass distribution of the matter we are interested in transporting. In the same vein, we define ν as the image of μ with respect to the ongoing finite time dynamics. The measure ν is supposed to have a density $h_\nu \frac{d\nu}{d\ell}$. It may be interpreted as the mass distribution of the transported matter at final time.

Let the time-dependent Frobenius-Perron operator be defined with respect to the Lebesgue measure ℓ as $P^{t,t+\tau}\colon L^1(X, \ell) \to L^1(Y, \ell)$. Now we define a transfer operator $L\colon L^1(X, \mu) \to L^1(Y, \nu)$ by

$$Lf = \frac{P^{t,t+\tau}(fh_\mu)}{h_\nu}, \tag{3.13}$$

where $h_\nu = P^{t,t+\tau}(h_\mu)$. Note that $L\mathbf{1}_X = \mathbf{1}_Y$. Now, let $L^*\colon L^\infty(Y,\nu) \to L^\infty(X,\mu)$ denote the dual operator of L. Then for $f \in L^1(X,\ell)$ and $g \in L^\infty(Y,\nu)$ we have that

$$\langle Lf, g\rangle_\nu = \int \frac{P^{t,t+\tau}(fh_\mu)}{h_\nu} g d\nu = \int P^{t,t+\tau}(fh_\mu)\, g d\ell = \int fg \circ \phi_t^{t+\tau} d\mu = \langle f, L^* g\rangle_\mu.$$

Note that the use of the standard duality relation between the Koopman operator $K^{t,t+\tau}$ and the Frobenius-Perron operator was used to make the above relation possible. We have, thus, $L^* = g \circ \phi_t^{t+\tau}$ and $L^*\mathbf{1}_Y = \mathbf{1}_X$. Finally, substituting the abstract operator L in the left hand side of (3.8) by the concrete operator L defined in (3.13), we have

$$\begin{aligned}
&\max_{X_1\cup X_2=X,\, Y_1\cup Y_2=Y} \left\{ \frac{\langle L\mathbf{1}_{X_1}, \mathbf{1}_{Y_1}\rangle_\nu}{\mu(X_1)} + \frac{\langle L\mathbf{1}_{X_2}, \mathbf{1}_{Y_2}\rangle_\nu}{\mu(X_2)} \right\} \\
&\max_{X_1\cup X_2=X,\, Y_1\cup Y_2=Y} = \left\{ \frac{\langle \mathbf{1}_{X_1}, L^*\mathbf{1}_{Y_1}\rangle_\nu}{\mu(X_1)} + \frac{\langle \mathbf{1}_{X_2}, L^*\mathbf{1}_{Y_2}\rangle_\nu}{\mu(X_2)} \right\} \\
&\max_{X_1\cup X_2=X,\, Y_1\cup Y_2=Y} = \left\{ \frac{\mu\left(X_1 \cap \left(\phi_t^{t+\tau}\right)^{-1} Y_1\right)}{\mu(X_1)} + \frac{\mu\left(X_2 \cap \left(\phi_t^{t+\tau}\right)^{-1} Y_2\right)}{\mu(X_2)} \right\} \\
&\qquad\qquad \leq 1 + \sigma_2.
\end{aligned}$$

Therefore, given any two measurable sets $\{Y_1, Y_2\}$ such that $X_1 = \left(\phi_t^{t+\tau}\right)^{-1} Y_1$ and $X_2 = \left(\phi_t^{t+\tau}\right)^{-1} Y_2$, we have that

$$\max_{X_1\cup X_2=X,\, Y_1\cup Y_2=Y} = \left\{ \frac{\mu\left(X_1 \cap \left(\phi_t^{t+\tau}\right)^{-1} Y_1\right)}{\mu(X_1)} + \frac{\mu\left(X_2 \cap \left(\phi_t^{t+\tau}\right)^{-1} Y_2\right)}{\mu(X_2)} \right\} = 2, \quad (3.14)$$

which implies directly that $\sigma_2 = 1$. As a consequence, every pair of measurable sets $\{X_1, X_2\}$ and $\{Y_1, Y_2\}$ that satisfy the relations $X_k = \left(\phi_t^{t+\tau}\right)^{-1} Y_k,\ k = 1, 2$ yield coherent sets that partition X and Y. However, constructed this way with the operator (3.13), these kind of coherent sets are infinitely many. Moreover, these coherent sets do not have robustness. Indeed, depending on the nature of the dynamics, the coherent couple $(X_k, Y_k),\ k = 1, 2$ may consist of thin and elongated measurable sets. As a consequence, any external perturbation will easily push points outside these sets. That means, these coherent sets lack robustness. The robustness property is, however, very important in practice, since real world physical systems are usually exposed to external perturbations. For instance, ocean dynamics are subject to perturbations such as wind intensities. In this context ocean gyres must be modeled as robust coherent sets. As a matter of fact, the operator (3.13) is not suitable to obtain optimal coherent sets. We should then build a different transfer operator by incorporating additional perturbations into the dynamics.

Hence, the deterministic operator (3.13) will be replaced by a non-deterministic linear operator built from the perturbed nonautonomous dynamics.

3.2.2 Robust operators and robust coherent sets

The robustness property of coherent sets is essential as argued in the previous section. Hence, we are going to study nonautonomous dynamics which are subject to additional perturbations. Note that the latter are independent from the dynamics and the reason why we are adding external perturbation is to find robust coherent sets. Indeed, our study is motivated by real world applications such as predicting the sudden split of the Antarctic polar vortex in September 2002. Given that coherent sets are obtained from compact transfer operators, we are going to construct the latter from the perturbed dynamics.
To construct the perturbed operator L, we should first specify the manner in which perturbations will be incorporated into the dynamics.
The perturbation process is similar to discontinuously adding small random noise. That is, firstly, the phase space X will be initially perturbed in the sense of shaking the whole domain with an amplitude $\epsilon > 0$. This means every single point in the phase space X will be perturbed with a radius of ϵ. Secondly, the flow will be applied to the perturbed phase space, say X_ϵ. Thirdly, the image phase space, denoted by $Y'_\epsilon := \phi_t^{t+\tau}(X_\epsilon)$, is again perturbed to yield the final phase space Y_ϵ which is the perturbed version of Y and yields the perturbed dynamics phase space at final time. Hence, it is clear that the underlying dynamics is only perturbed at initial and final time [16]. That is why, the perturbation is referred to as a discontinuous addition of small random noise.
A concrete mathematical formulation of the perturbation process is also constructed progressively. Perturbation is added in form of local diffusion which is modeled using the diffusion operators

$$\begin{aligned} &\mathcal{D}_\epsilon^X \colon L^1(X,\ell) \to L^1(X_\epsilon,\ell), \qquad \mathcal{D}_\epsilon^X g(y) = \int_X \gamma_{X,\epsilon}(y-x)g(x)dx \\ &\mathcal{D}_\epsilon^{Y'_\epsilon} \colon L^1(Y'_\epsilon,\ell) \mapsto L^1(Y_\epsilon,\ell), \qquad \mathcal{D}_\epsilon^{Y'_\epsilon} f(y) = \int_{Y'_\epsilon} \gamma_{Y'_\epsilon,\epsilon}(y-x)f(x)dx \end{aligned} \tag{3.15}$$

where

$$\begin{aligned} &\gamma_{X,\epsilon} \colon D \to \mathbb{R}_+, \qquad \int_{X_\epsilon} \gamma_{X,\epsilon}(y-x)dy = 1, \\ &\gamma_{Y'_\epsilon} \colon D \to \mathbb{R}_+, \qquad \int_{Y_\epsilon} \gamma_{Y'_\epsilon}(y-x)dy = 1. \end{aligned} \tag{3.16}$$

are the stochastic kernels. Thus, the operators (3.15) act as convolution with the stochastic kernels (3.16). To fix thoughts, one may think of the kernels functions (3.16) as supported on ϵ-neighborhood of the origin, that $X_\epsilon = \text{supp}\left(\mathcal{D}_\epsilon^X \mathbf{1}_X\right)$, that $Y'_\epsilon = \phi_t^{t+\tau}(X_\epsilon)$ and that $Y_\epsilon = \text{supp}\left(\mathcal{D}_\epsilon^{Y'_\epsilon} \mathbf{1}_{Y'_\epsilon}\right)$.
From (3.15), we construct the perturbed version of the Lebesgue Frobenius-Perron operator $P^{t,t+\tau}$ as

$$P_\epsilon^{t,t+\tau}\colon L^1(X,\ell) \mapsto L^1(Y_\epsilon,\ell), \qquad P_\epsilon^{t,t+\tau} f(y) = \mathcal{D}_\epsilon^{Y'_\epsilon} \circ P^{t,t+\tau} \circ \mathcal{D}_\epsilon^X f(y).$$

That is

$$P_\epsilon^{t,t+\tau} f(y) = \int_X \left(\int_{X_\epsilon} \gamma_{Y'_\epsilon}(y - \phi_t^{t+\tau}(z)) \gamma_{X,\epsilon}(z-x) dz \right) f(x) dx. \tag{3.17}$$

Given that $h_\mu = \frac{d\mu}{d\ell}$, we can operate a change of measure and rewriting (3.17) yields

$$P_\epsilon^{t,t+\tau} f(y) = \int_X \left(\int_{X_\epsilon} \gamma_{Y'_\epsilon}(y - \phi_t^{t+\tau}(z)) \gamma_{X,\epsilon}(z-x) dz \right) \frac{f(x)}{h_\mu(x)} d\mu(x).$$

Besides, we have

$$P_\epsilon^{t,t+\tau}(f h_\mu)(y) = \int_X \left(\int_{X_\epsilon} \gamma_{Y'_\epsilon}(y - \phi_t^{t+\tau}(z)) \gamma_{X,\epsilon}(z-x) dz \right) f(x) d\mu(x) \tag{3.18}$$

and

$$P_\epsilon^{t,t+\tau}(h_\mu)(y) = \int_X \left(\int_{X_\epsilon} \gamma_{Y'_\epsilon}(y - \phi_t^{t+\tau}(z)) \gamma_{X,\epsilon}(z-x) dz \right) d\mu(x). \tag{3.19}$$

Note that taking $f = \mathbf{1}_X$ in equation (3.18) yields equation (3.19). Hence, we can normalize (3.18) with (3.19) and finally define the perturbed transfer operator L_ϵ as

$$L_\epsilon^{t,t+\tau} f(x) = \frac{P_\epsilon^{t,t+\tau}(f \cdot h_\mu)(x)}{P_\epsilon^{t,t+\tau} h_\mu(x)} \tag{3.20}$$

which satisfies the relation $L_\epsilon^{t,t+\tau} \mathbf{1}_X = \mathbf{1}_{Y_\epsilon}$. A more detailed expression of (3.20) is given as

$$\begin{aligned} L_\epsilon^{t,t\tau} f(y) &= \frac{\int_X \left(\int_{X_\epsilon} \gamma_{Y'_\epsilon}(y - \phi_t^{t+\tau}(z)) \gamma_{X,\epsilon}(z-x) dz \right) f(x) h_\mu(x) dx}{\int_X \left(\int_{X_\epsilon} \gamma_{Y'_\epsilon}(y - \phi_t^{t+\tau}(z)) \gamma_{X,\epsilon}(z-x) dz \right) h_\mu(x) dx} \\ &= \int_X \Gamma_\epsilon(x,y) f(x) d\mu(x) \end{aligned} \tag{3.21}$$

In [16], it is proven that the operator $L_\epsilon^{t,t\tau}$ will act on functions in $L^2(X,\mu)$, depending on the conditions set on the kernels functions (3.16). More precisely, a suitable choice would be

$$\gamma_{X,\epsilon} = \gamma_{Y'_\epsilon} = \frac{1}{\ell(B_\epsilon(0))}\mathbf{1}_{B_\epsilon(0)}$$

then (3.21) becomes

$$\begin{aligned} L_\epsilon^{t,t+\tau} f(y) &= \int_X \frac{\ell\left(B_\epsilon(x) \cap (\phi_t^{t+\tau})^{-1}\left(B_\epsilon(y)\right)\right)}{\int_X \ell\left(B_\epsilon(x) \cap (\phi_t^{t+\tau})^{-1}(B_\epsilon(y))\right) d\mu(x)} f(x) d\mu(x) \\ &= \int_X \Gamma_\epsilon(x,y) f(x) d\mu(x), \end{aligned} \tag{3.22}$$

where

$$\Gamma_\epsilon(x,y) = \frac{\ell\left(B_\epsilon(x) \cap (\phi_t^{t+\tau})^{-1}\left(B_\epsilon(y)\right)\right)}{\int_X \ell\left(B_\epsilon(x) \cap (\phi_t^{t+\tau})^{-1}(B_\epsilon(y))\right) d\mu(x)}. \tag{3.23}$$

Thus, [16] showed that $\Gamma_\epsilon(x,y) \in L^2(X \times Y_\epsilon, \mu \times \nu)$, $L_\epsilon^{t,t+\tau}$ is compact and acts on $L^2(X,\mu)$. Moreover, the dual operator $L_\epsilon^{(t,t+\tau)*}$ is compact and satisfies $L_\epsilon^{(t,t+\tau)*}\mathbf{1}_{Y_\epsilon} = \mathbf{1}_X$. We arrive then at the conclusion that the operator $L_\epsilon^{t,t+\tau}$ fulfills the conditions to yield σ_2 as in (3.7) and then optimal coherent sets can be obtained from its discrete spectrum. The process of constructing the operator $L_\epsilon^{t,t+\tau}$ looks technical but the end goal consists of numerically approximating the latter in order to arrive at a matrix similar to (3.4). Indeed, one may already view the the stochastic kernel Γ_ϵ in (3.22) as a matrix with matrix entries entries $\Gamma_\epsilon(x,y)$ and the evolution of densities $L_\epsilon^{t,t\tau} f(y)$ in (3.21) as a matrix multiplication. We will see later in this study that a systematic exploitation of the SVD of the matrix approximation of (3.21) yields approximation of coherent sets. In chapter 6, the latter will be computed and there qualitative change within the finite time dynamics will be studied. This will consist of a purely discretized finite time bifurcation framework and coherent patterns will be extracted from sign patterns of singular vectors. But from now, we remark that the infinite dimensional operator $L_\epsilon^{t,t+\tau}$ in (3.22) acts on densities f as a matrix multiplication where the operator $\Gamma_\epsilon(x,y)$ in (3.23) denotes the matrix entries. A finite dimensional approximation of $L_\epsilon^{t,t+\tau}$ was fully developed in [36].

3.3 Autonomous dynamics, robust almost-invariant sets

In the autonomous setting, the analytic framework developed in section 3.2 becomes simpler. Indeed, the dynamics no longer depends on both initial and final time, only

the flow time matters. Moreover, the dynamics is fixed in space which means we only consider the domain $X \subset D$ and look at fix measurable almost-invariant sets with respect to an invariant measure μ which is absolutely continuous with respect to the Lebesgue measure ℓ. Hence, as, in section 3.2 with nonautonomous dynamics, we are particularly interested in finding an optimal measurable almost-invariant set A. This is equivalent to finding a measurable partition $\left\{A, A^c\right\}$ of the domain X with minimal transport between them. In order to set an optimization problem, a functional representation of this partition is used as $\mathbf{1}_A$ and $\mathbf{1}_{A^c}$. Thus, under the constraint $\mu(A) \approx \mu(A^c)$ and $L\mathbf{1}_A \approx \mathbf{1}_A,\ L\mathbf{1}_{A^c} \approx \mathbf{1}_{A^c}$, we maximize over measurable sets A the following ratio

$$r_t(A) = \frac{\left\langle L\mathbf{1}_A, \mathbf{1}_A \right\rangle}{\mu(A)} + \frac{\left\langle L\mathbf{1}_{A^c}, \mathbf{1}_{A^c} \right\rangle}{\mu(A^c)}. \tag{3.24}$$

The ratio (3.24) is equivalent to

$$r_t(A) = \frac{\mu(A \cap \left(\phi^t\right)^{-1}(A))}{\mu(A)} + \frac{\mu(A^c \cap \left(\phi^t\right)^{-1}(A^c))}{\mu(A^c)}. \tag{3.25}$$

Note that, the operator L is the same as (3.6) defined in section 3.1.3 but defined in $L^2(X, \mu)$ to itself. Under the specific deterministic autonomous dynamics, the ratio in the left hand side of (3.14) becomes (3.25). Thus, the framework for finding optimal almost-invariant sets is just a particular setting of section 3.2.

It is clear that the optimal almost-invariant set A will satisfy $r_t(A) \approx 2$. However, the problem (3.25) is not well posed. Therefore, we seek realistic optimal almost-invariant sets, in the sense of robustness in the presence of noise as described in section 3.2, or small external random perturbations. Therefore, a perturbed transfer L_ϵ, which is dynamically similar to P^t, is necessary. If ϵ represents the perturbation strength, a diffused transfer operator, L_ϵ is constructed in section 3.2 and was proposed in [16]. Robust almost-invariant sets will eventually be computed from the spectrum of a self-adjoint operator derived from the diffused transfer operators [36]. As mentioned above, we use an ϵ-perturbation to obtain a diffused version of the deterministic transfer operator L. Thus, as discussed in [16], the following diffusion operator transforms a deterministic density to a diffused one via a stochastic kernel with a bounded support, Moreover, the kernel is supported in $B_\epsilon(0)$ with an explicit form $\gamma_\epsilon = \frac{1}{\ell(B_\epsilon(0))}\mathbf{1}_{B_\epsilon(0)}$. Therefore, with this choice of the stochastic kernel, both operators L_ϵ and L_ϵ^* are compact, positive with $L_\epsilon \mathbf{1}_X = \mathbf{1}_X$ and $L_\epsilon^* \mathbf{1}_X = \mathbf{1}_X$. From now on we can address the question of finding robust almost-invariant sets under the ϵ-perturbed dynamics. Hence, we set a perturbed version

of (3.24) as

$$r^{\epsilon}(A) = \frac{\left\langle L_{\epsilon}\mathbf{1}_A, \mathbf{1}_A \right\rangle}{\mu(A)} + \frac{\left\langle L_{\epsilon}\mathbf{1}_{A^c}, \mathbf{1}_{A^c} \right\rangle}{\mu(A^c)}. \tag{3.26}$$

The optimization problem becomes finding a measurable partition $\left\{A, A^c\right\}$ that maximizes (3.26), i.e., $\mu(A) \approx \mu(A^c)$ and $L_{\epsilon}\mathbf{1}_A \approx \mathbf{1}_A$, $L_{\epsilon}\mathbf{1}_{A^c} \approx \mathbf{1}_{A^c}$. The constraint $\mu(A) \approx \mu(A^c)$ is set to ensure that the partition is nontrivial. The expression (3.26) is equivalent to the following

$$r^{\epsilon}(A) = \frac{\left\langle Q_{\epsilon}\mathbf{1}_A, \mathbf{1}_A \right\rangle}{\mu(A)} + \frac{\left\langle Q_{\epsilon}\mathbf{1}_{A^c}, \mathbf{1}_{A^c} \right\rangle}{\mu(A^c)}. \tag{3.27}$$

where $Q_{\epsilon} = \frac{L_{\epsilon}+L_{\epsilon}^*}{2}$. The latter has the same property as L_{ϵ} and, more importantly, it is self-adjoint. Therefore, in [16, 36], it is shown that maximizing r^{ϵ} over all measurable sets is the same as solving the relaxed optimization problem

$$\max_{f\neq 0}\left\{\frac{\langle Q_{\epsilon}f, f\rangle}{\|f\|_{\mu}^2}, \quad \langle f, \mathbf{1}_X\rangle = 0\right\} \tag{3.28}$$

knowing that the solution of the above problem is λ_2, the second largest eigenvalue of Q_{ϵ}, which is realized for $f = v_2$ where v_2 is he corresponding eigenfunction. Indeed, due to the properties of Q_{ϵ} including compactness and self-adjointness with the specific choice of the stochastic kernel γ_{ϵ}, the first dominant eigenvalue, $\lambda_1 = 1$, is simple and $\mathbf{1}_D$ is the corresponding eigenfunction [16]. Moreover, all the eigenvalues of Q_{ϵ} are real. However, the spectrum of L_{ϵ} and L_{ϵ}^* may be complex except for the leading eigenvalue $\lambda_1 = 1$, which is also simple with $\mathbf{1}_X$ as the corresponding eigenfunction. It is possible to find bounds of r^{ϵ} [36] as

$$2 - 2\sqrt{(1-\lambda_2)} \leq \sup_{A\subset D} r^{\epsilon}(A) \leq 1 + \lambda_2. \tag{3.29}$$

It is clear from (3.29) that $\sup_{A\subset X} r^{\epsilon}(A) \approx 2$ whenever $\lambda_2 \approx 1$. Consequently, the existence of an eigenvalue $\lambda_2 \approx 1$ is linked to the existence of an almost-invariant set A. Furthermore, the corresponding measurable partition into almost-invariant sets A and A^c is constructed from the corresponding eigenfunction v_2. Indeed, a threshold δ is carefully chosen so that A and A^c are the upper and lower level sets of v_2, respectively.
Numerical approximations of L_{ϵ} and Q_{ϵ} and computation of almost-invariant sets can be found in [36]. In this study, we will just use them in case we need them. Note that

this work addresses bifurcations of almost-invariant/coherent sets. But in chapter 4 and chapter 5, it will be clear that set-oriented bifurcation is only possible with the discretized compact operators L_ϵ and Q_ϵ.

3.4 Summary

The analytic framework proposed above was widely developed in [16]. Moreover, finite dimensional approximation of (3.21) and its autonomous version in section 3.3 was widely developed in [36]. Thus, this chapter can be viewed as a mandatory introduction for understanding the theoretical background of our current study. Indeed, it is necessary to have a solid comprehension of measurable coherent/almost-invariant sets before any further serious work in this regards. A very interesting observation is that there is a strong interdependency connection between discrete spectra of compact operators and set-oriented dynamics. That is why, in the upcoming chapters we are going to use this connection to characterize bifurcation in a set-oriented dynamical system approach. The latter approach is actually very innovative. Hence, in chapter 4, we will show how to specifically characterize bifurcation of almost invariant sets based on known classical bifurcation theory [10, 25, 28].

4 Bifurcations, spectral signatures and almost-invariant sets

This chapter is the starting point of the study of qualitative changes of optimal almost-invariant/coherent sets. Understanding and characterizing changes of optimal almost-invariant/coherent sets sounds a very unfamiliar task to do despite the rich content of dynamical system theory. Indeed, by the time we are writing this thesis, there is no preexisting study in this regard that we know of. Therefore, we will start our work by briefly reviewing the very classical theory of qualitative changes of a dynamical system on a microscopic level, before we progressively move forward to address changes in a macroscopic levels.

4.1 Basic concepts and definitions

Let us define a p-parametrized ODE in the Lebesgue measure space (D, Σ, μ) with D a compact subset of $\mathbb{R}^d$ and let us suppose that $p \in \mathbb{R}$ is a bifurcation parameter.

$$\dot{x} = F(x, p) =: F_p(x). \tag{4.1}$$

We fix p and assume that the vector field $F_p : D \to \mathbb{R}^d$ is sufficiently smooth to guarantee the existence and uniqueness of solutions of (4.1). Thus, there exists a flow map $S^t : D \to D$ such that for any given initial solution $x(0) = x_0$ and flow time $t \in \mathbb{R}$

$$x_0 \mapsto S^t(x_0) \in D, \ x_0 \in D \tag{4.2}$$

yields the solution of the system at time t for the initial value x_0. Note that in this chapter we use the notation S^t for a flow map, unlike the notation used in chapter 2 (2.17). Indeed, we want to avoid naming confusions between flow map and eigenfunctions that

we will introduce later.
Recall that the solution of (4.1) generates a Frobenius-Perron operator

$$\begin{aligned} P^t f(x) &= \frac{f(S^{-t}(x))}{|\det J(S^t)(x)|} \\ &= \int_X \delta(x - S^t(y))\rho_0(x)d\mu(y), \;\; t \geq 0, \end{aligned} \tag{4.3}$$

which is actually a strongly continuous semigroup of contraction. Hence, its infinitesimal generator is given by

$$\mathcal{G}f := \lim_{t\to 0} \frac{P^t f - f}{t} \;\; f \in D(\mathcal{G}). \tag{4.4}$$

$\mathcal{G}$ is linear and its domain is given by

$$D(\mathcal{G}) = \Big\{ f \in D(P^t) : \;\; \lim_{t\to 0} \frac{P^t f - f}{t} \quad \text{exists} \Big\}.$$

In this work, the infinitesimal generator of the Lebesgue Frobenius-Perron operators generated by (4.1) is particularly given by the so-called transport/continuity equation

$$\mathcal{G}f := -\nabla \cdot (F_p f) = -F_p \cdot \nabla f,$$

for every continuously differentiable function f (Chapter 7, [49]). Given such initial time density f, the density at time t, $g(t,x) = P^t f(x)$, is the solution of the equation

$$\frac{\partial g}{\partial t} = -F_p \cdot \nabla g = \mathcal{G}(g). \tag{4.5}$$

Furthermore, the discrete spectra of both P^t and $\mathcal{G}$, denoted respectively by $\sigma(P^t)$ and $\sigma(\mathcal{G})$, are related by the spectral mapping theorem (Theorem 2.4 [50])

$$e^{t\sigma(\mathcal{G})} \subset \sigma(P^t) \subset e^{t\sigma(\mathcal{A})} \cup \{0\}, \;\; \forall \; t > 0. \tag{4.6}$$

This means that for a given $t > 0$, if $\lambda \in \sigma(\mathcal{G})$ then $e^{\lambda t} \in \sigma(P^t)$, conversely, if $e^{\lambda t} \in \sigma(P^t)$ then $\lambda + \frac{2\pi i c}{t} \in \sigma(\mathcal{G}), \;\; c \in \mathbb{Z}$. Note that both operators P^t and $\mathcal{G}$ can also have a continuous spectrum, since they are infinite dimensional. However, in this work we will only focus on the discrete spectra of both operators. Moreover, for an appropriate Banach space $D(P^t), \;\; t \geq 0$, the resolvent operator of $\mathcal{G}$, given by $\mathcal{R}(z) = (zI - \mathcal{G})^{-1}, \;\; z \in \rho(\mathcal{G}) = \mathbb{C} \setminus \sigma(\mathcal{G})$ with $\rho(\mathcal{G})$ being the resolvent set, is bounded and its explicit form becomes the

Laplace transform of semigroup $P^t,\ t \geq 0$ (see [31], Chapter II, Theorem 1.10). That is,

$$\mathcal{R}(z)f = \int_0^\infty e^{-zs} P^s f ds,\ \ f \in L^1,\ \ z \in \rho(\mathcal{G}),\ \text{ with } \ \mathrm{Re}(z) > 0. \tag{4.7}$$

4.2 Bifurcations

4.2.1 Classical approach

The origin of the term bifurcation was by Henri Poincaré [30] who used it to describe the "splitting" of equilibrium solutions, given the family of ODEs (4.1). Indeed, given a parametrized dynamical system, bifurcation occurs when a change in parameter causes an equilibrium point to move the system to a qualitively different regime. The equilibrium solutions of (4.1) are the solutions of the equation $F(x,p) = 0$. Hence, equilibrium points can be created or destroyed, or their stability can change, as the parameter p is varied. Moreover, as p varies, these equilibrium points are described by smooth functions of p, say $x_0(p)$, far from points at which the Jacobian derivative of $F(x,p)$ with respect to x, denoted by DF_p, has a zero eigenvalue. The graphs $\{(p, x_0(p)),\ \ p \in \mathbb{R}\}$ are *branches of equilibria* of (4.1). Thus, we say that $(p_0, \bar{x}_0)$ is a point of *bifurcation* if DF_p has a zero eigenvalue at $(p_0, \bar{x}_0)$. In this case, several branches of equilibria may come together and qualitative changes such as loss or gain of stability may occur. These qualitative changes in the dynamics are called *bifurcations*. A *bifurcation diagram* is a diagram that depicts the evolution of the graphs $\{(p, x_0(p)),\ \ p \in \mathbb{R}\}$. The following example illustrates a bifurcation which occurs as a catastrophic jump. Catastrophe is meant in the sense that the stability of an equilibrium point will break down and causes the system to suddenly jump to into another state.

Example 9

$$\dot{x} = p - x^3 + x,\ \ p, x \in \mathbb{R}. \tag{4.8}$$

The dynamical system generated by the ODE (4.8) undergoes a qualitative change as an example of bifurcation with the corresponding diagram shown in figure 4.1. There are two bifurcation points marked as black dots. The blue branches are stable equilibrium points or stable states, while the red branch connects unstable equilibrium points or unstable states. Hence, when the parameter p passes beyond a bifurcation point, the system transitions very fast to another stable state. This sudden transition is not immediately followed by another

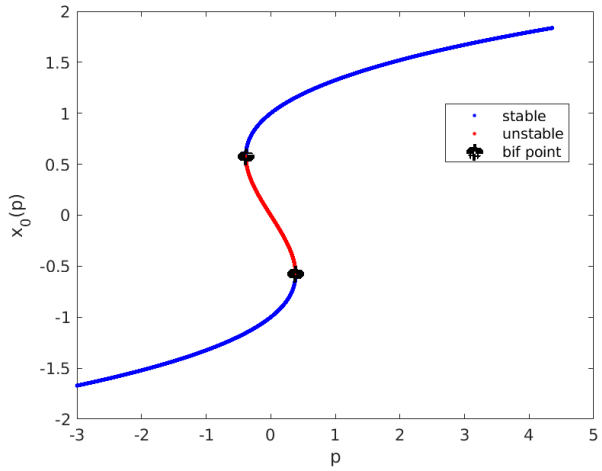

Figure 4.1: Bifurcation diagram of the (4.8) in Example 9.

sudden jump towards the previous stable state by simply tuning parameters p slightly. In fact, one needs to put a considerable change in the parameter p in order to get back to the prior stable state. This lack of immediate reversibility as a parameter is changed is called hysteresis. *Therefore, the bifurcation diagram exhibits oscillations between stable states where slow and fast motions alternate. This is known as the* hysteresis loop. *Mathematical models where the hysteresis bifurcation are found include the Budworm population dynamics. The latter describes the population dynamics of an insect called spruce budworm (see [25], chapter 3).*

4.2.2 Statistical approach and the trace formula

In example 9, we have illustrated qualitative changes, occurring in the dynamics of a chosen initial point. The bifurcation of an ensemble of trajectories can also be studied by relying on the statistical properties of the deterministic system (4.1). The latter suggests a formulation of a randomly generated set of initial points into a probability distribution function, as introduced in chapter 2. One then needs to study their evolution under the deterministic dynamics via the continuity equation (4.5). In this setting, it is possible to study the bifurcation of the underlying system statistically. This method is spectral and connects the spectra of the operators (4.3) and (4.4) to the stability eigenvalues of the stationary points of (4.1). Indeed, a spectral signature of the pitchfork bifurcation was studied in [17] where, in an appropriate functional space, the spectrum of the infinitesimal generator could be found as well as the corresponding eigenfunctions. The

eigenvalues of (4.4) came out as a linear combination of the bifurcation parameters p and stability eigenvalues. As a result, eigenvalues tend to accumulate at zero as the bifurcation parameter comes close to 0. The challenging part of this method is choosing the appropriate functional space for the eigenfunctions.

An easier approach that guarantees a direct computation of the eigenvalues of (4.4) is based on the so-called trace formula (Chapter 3, [48]). This approach consists of extracting eigenvalues by computing the trace of the resolvent operator (4.7). Indeed, from the Laplace transform (4.7), we have that

$$tr\mathcal{R}(z)f = tr(zI - \mathcal{G})^{-1} = tr\int_0^\infty e^{-zs}P^s ds = \int_0^\infty e^{-zs} trP^s ds \tag{4.9}$$

and

$$\begin{aligned} trP^t &= tr\int_X \delta(x - S^t(y))\rho_0(x)d\mu(y) \\ &= \int_X \delta(x - S^t(x))d\mu(x) \\ &= \sum_s \frac{1}{|\det\left(I - J(S^t)(x_s)\right)|} \end{aligned}$$

where $x_s,\ s \in \mathbb{N}$ denote(s) the stationarity solution(s). A necessary condition to use the trace formula is to assume that all the stationary points of (4.1) are hyperbolic. That is, the corresponding stability eigenvalues of x_s, denoted by $\lambda_{s,j} \in \mathbb{C},\ \ j = 1, 2, \cdots, d$, should satisfy $\mathrm{Re}(\lambda_{s,j}) \neq 0$. Since $J(F_p)$ is the matrix of the linearized vector field, we have $J(S^t(x_s)) = \exp(J(F_p)(x_s)t),\ \ t \geq 0$, and hence

$$trP^t = \sum_s \frac{1}{|\det\left(I - \exp(J(F_p)(x_s)t)\right)|}.$$

One can see that trP^t diverges like $\frac{1}{|t|^n},\ n \in \mathbb{N}$ for $t \to 0$, but it also decays to zero for $t \to \infty$. Indeed, we can rewrite trP^t as

$$trP^t = \sum_s \prod_{j=1}^{d} \frac{1}{\left|1 - \exp(\lambda_{(s,j)}(p)t)\right|}$$

which can be decomposed as

$$trP^t = \sum_s \left(\prod_{\mathrm{Re}(\lambda_{(s,j)}(p))>0} \frac{\exp(-\lambda_{(s,j)}(p)t)}{1-\exp(-\lambda_{(s,j)}(p)t)} \right) \left(\prod_{\mathrm{Re}(\lambda_{(s,j)}(p))<0} \frac{1}{1-\exp(\lambda_{(s,j)}(p)t)} \right).$$

Therefore, for $t \to +\infty$, we that $\frac{\exp(-\lambda_{(s,j)}(p)t)}{1-\exp(-\lambda_{(s,j)}(p)t)} \to 0$ and $\frac{1}{1-\exp(\lambda_{(s,j)}(p)t)} \to 1$. Moreover, in the denominators we have $\left|\exp(-\lambda_{(s,j)}(p)t)\right| < 1$ and $\left|\exp(\lambda_{(s,j)}(p)t)\right| < 1$, for positive real parts and negative real parts, respectively. Thus, we can write trP^t as a Taylor expansion in the following way:

$$\begin{aligned}
trP^t &= \sum_s \left(\prod_{\mathrm{Re}(\lambda_{(s,j)}(p))>0} \exp\left(-\lambda_{(s,j)}(p)t\right) \sum_{n_j=0}^{\infty} \exp\left(-n_j\lambda_{(s,j)}(p)t\right) \right) \times \\
&\qquad \left(\prod_{\mathrm{Re}(\lambda_{(s,j)}(p))<0} \sum_{m_j=0}^{\infty} \exp\left(m_j\lambda_{(s,j)}(p)t\right) \right) \\
&= \sum_s \prod_{\mathrm{Re}(\lambda_{(s,j)}(p))>0} \sum_{n_j=0}^{\infty} \exp\left(-(n_j+1)\lambda_{(s,j)}(p)t\right) \prod_{\mathrm{Re}(\lambda_{(s,j)}(p))<0} \sum_{m_j=0}^{\infty} \exp\left(m_j\lambda_{(s,j)}(p)t\right) \\
&= \sum_s \sum_{n_j=0}^{\infty} \exp\left(- \sum_{\mathrm{Re}(\lambda_{(s,j)}(p))>0} (n_j+1)\lambda_{(s,j)}(p)t \right) \sum_{m_j=0}^{\infty} \exp\left(\sum_{\mathrm{Re}(\lambda_{(s,j)}(p))<0} m_j\lambda_{(s,j)}(p)t \right) \\
&= \sum_s \sum_{n_j,m_j=0}^{\infty} \exp\left[- \sum_{\mathrm{Re}(\lambda_{(s,j)}(p))>0} (n_j+1)\lambda_{(s,j)}(p)t + \sum_{\mathrm{Re}(\lambda_{(s,j)}(p))<0} m_j\lambda_{(s,j)}(p)t \right].
\end{aligned}$$

The trace of the transfer operator is, thus, a sum of exponential decays, for each stationary point. Hence, given a hyperbolic stationary point x_s

$$trP^t = \sum_{n_j,m_j=0}^{\infty} \exp\left[- \sum_{\mathrm{Re}(\lambda_{(s,j)}(p))>0} (n_j+1)\lambda_{(s,j)}(p)t + \sum_{\mathrm{Re}(\lambda_{(s,j)}(p))<0} m_j\lambda_{(s,j)}(p)t \right],$$

and it follows from (4.9) that

$$\begin{aligned}
tr(zI-\mathcal{G})^{-1} = \int_0^{\infty} &\exp(-zs) \times \\
&\sum_{n_j,m_j=0}^{\infty} \exp\left[- \sum_{\mathrm{Re}(\lambda_{(s,j)}(p))>0} (n_j+1)\lambda_{(s,j)}(p)t + \sum_{\mathrm{Re}(\lambda_{(s,j)}(p))<0} m_j\lambda_{(s,j)}(p)t \right] ds.
\end{aligned}$$

Computing the integral above, we have, for $z \in \rho(\mathcal{G})$ with $\mathrm{Re}(z) > 0$, that

$$tr(zI-\mathcal{G})^{-1} = \sum_{n_j,m_j=0}^{\infty} \left(z + \sum_{\mathrm{Re}(\lambda_{(s,j)}(p))>0} (n_j+1)\lambda_{(s,j)}(p) - \sum_{\mathrm{Re}(\lambda_{(s,j)}(p))<0} m_j\lambda_{(s,j)}(p) \right)^{-1}. \tag{4.10}$$

Therefore, the discrete spectrum of the generator associated to the stationary point x_s is given by the poles of (4.10). That is,

$$z = - \sum_{\mathrm{Re}(\lambda_{(s,j)}(p))>0} (n_j+1)\lambda_{(s,j)}(p) + \sum_{\mathrm{Re}(\lambda_{(s,j)}(p))<0} m_j\lambda_{(s,j)}(p). \tag{4.11}$$

Note that z in (4.11) is a function of n_j, m_j and p and we can write $z(n_j, m_j, p)$, to mean z and vice versa. Thus, the discrete spectrum of $\mathcal{G}$ in (4.11) is composed of isolated eigenvalues of finite multiplicity which are located in the strip $-q < \mathrm{Re}\, z < 0$, for some $q > 0$. As a consequence, due to (4.6), the discrete spectrum of $P^t,\ t \geq 0$ consists of isolated eigenvalues of finite multiplicity which are located inside the unit disc. Since (4.11) is a linear combination of the stability eigenvalues, it follows that (4.11) is relevant to characterize a bifurcation. As mentioned above, (4.11) and their corresponding eigenfunctions were used in [17] to characterize the one-dimensional pitchfork bifurcation. A concrete example is given in the following.

Example 10

$$\dot{x}(t) = -\left(\pi p \sin(2\pi x) + (1-p)\pi \sin(\pi x)\right), \ \ p, x \in [0,\, 1]. \tag{4.12}$$

For $p \in [0,\, 1/3]$, the stationary points are given by

$x_1 = 0, \quad x_2 = 1$ *with stability eigenvalues* $\lambda_1(p) = \pi^2(p+1), \quad \lambda_2(p) = -\pi^2(3p-1).$

For $p \in [0,\, 1/3]$, the stationary points are given by
$x_1 = 0, \quad x_2 = 1, \quad x_3 = \frac{1}{\pi}\arccos\left(\frac{p-1}{2p}\right)$ *with corresponding stability eigenvalues*
$\lambda_1(p) = \pi^2(p+1), \quad \lambda_2(p) = -\pi^2(3p-1), \ \lambda_3(p) = -\left[2\pi^2\cos(2\arccos(\frac{p-1}{2p})) - \frac{(1-p)^2}{2p}\pi^2\right]$.
Thus, one sees that $\lambda_1(p)$ is always negative while $\lambda_3(p)$ is positive and exists only for $p \in (1/3,\, 1]$. However, $\lambda_2(p)$ is positive for $p \in [0,\, 1/3)$, negative for $p \in (1/3,\, 1]$, and $\lambda_2(p) = 0$ when $p = 1/3$. Therefore, a bifurcation occurs at $p = 1/3$. Given that the fixed point $x_1 = 0$ is always stable, we can only focus on $\lambda_2(p)$ and $\lambda_3(p)$, in order to investigate

the bifurcation in a spectral level. In figure 4.2, we show the changes of $\lambda_2(p)$ *and* $\lambda_3(p)$ *with respect to the changes of the bifurcation parameter* p*. The discrete spectrum (4.11) of*

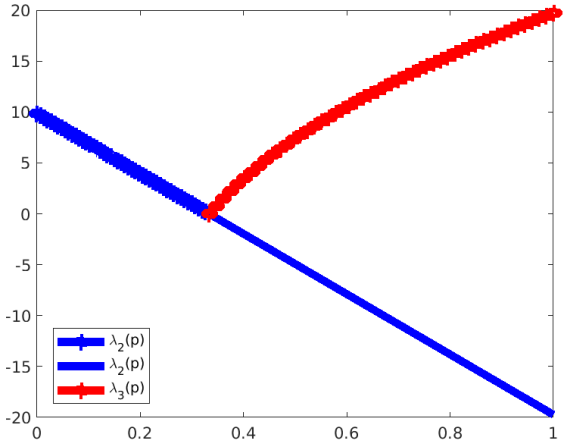

Figure 4.2: In the $y-$axis: stability eigenvalues $\lambda_2(p)$ in blue (dashed line for $p < 1/3$ and smooth line for $p > 1/3$), stability eigenvalues $\lambda_3(p)$ in red and dashed curve of the system (4.12). In the $x-$axis the bifurcation parameter p.

the generator at x_2 *and* x_3 *can be easily computed now.*

For $p < 1/3$:

$$\text{at } x_2: \quad z_2(n,p) = (n+1)\pi^2(3p-1), \ n = 0,1,2,\cdots$$

For $p > 1/3$:

$$\text{at } x_2: \quad z_2(n,p) = -n\pi^2(3p-1), \ n = 0,1,2,\cdots,$$

$$\text{at } x_3: \quad z_3(n,p) = (n+1)\left[2\pi^2\cos(2\arccos(\frac{p-1}{2p})) - \frac{(1-p)^2}{2p}\pi^2\right], \ n = 0,1,2,\cdots.$$

Hence, changes in these eigenvalues correspond to the spectral signatures of the undergoing bifurcation. The latter are illustrated in figure 4.3. For each bifurcation parameter p*,* $n = 10$ *eigenvalues of the generator (4.4) are plotted. Figure 4.3 agrees perfectly with the spectral data formula in (4.11). Moreover, as the bifurcation parameter is close to its critical value, i.e.* $p = 1/3$*, the eigenvalues tend to shrink and accumulated near zero. This is a typical spectral signature of the bifurcation. Compared to the classical bifurcation studied in example 9, we are able to see the slowing down scenario before the system transitions to its post-bifurcation state. Indeed, slowing down was observed to occur in the dynamics of systems before a bifurcation occurs [5]. On the spectral level, we observe an accumulation of the spectrum of the generator around zero. The same can be observed with the spectra of the transfer operators* $P^t, \ t \geq 0$ *by simply applying the spectral relation in (4.6) with a chosen*

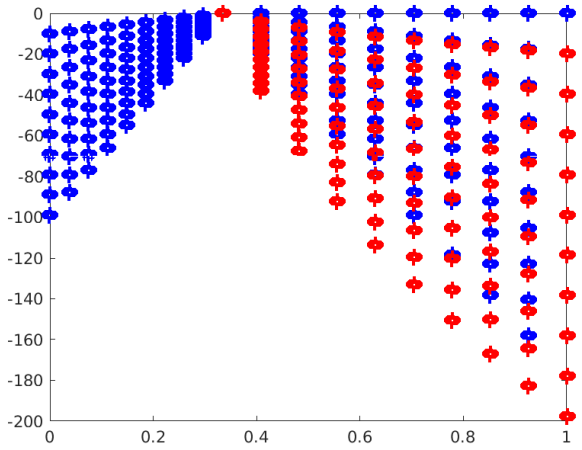

Figure 4.3: In the $y-$axis: $z_2(n,p)$ in blue and $z_3(n,p)$ in red. In the $x-$axis the bifurcation parameter p.

time t. For instance, with $t = 10^{-4}$ we have the changes of the spectrum of P^t in figure 4.4.

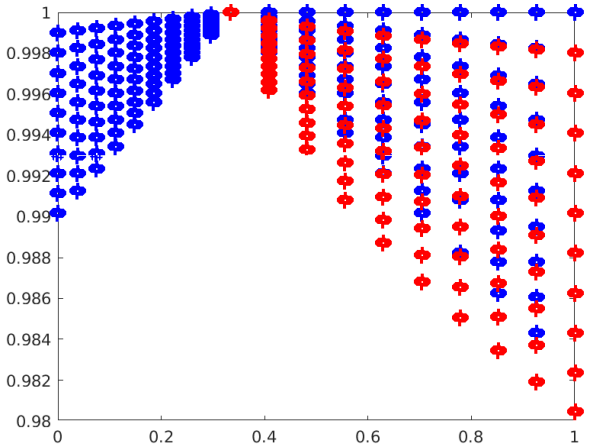

Figure 4.4: In the $y-$axis: $\exp(z_2(n,p)t)$ in blue and $\exp(z_3(n,p)t)$ in red. In the $x-$axis the bifurcation parameter p. The chosen time is $t = 10^{-4}$.

One then observes a convergence of the eigenvalues of $P^t,\ t \geq 0$ towards 1 as p approaches its critical value. Note that the bifurcation found in (4.12) is similar to a generic pitchfork normal form ([28], Chapter 2), since the only difference is the lack of symmetry of the emerged unstable branch $\lambda_3(p)$ for $p > 0$. Nevertheless, the spectral signature shown in figure 4.3 has similar trends as in [17]. Therefore, we can say that these spectral trends are generic indicators of bifurcations including the the pitchfork bifurcation.

A similar spectral approach was used in [46] using the generic Hopf bifurcation ([28], Chapter 3). In this study, however, we are more interested in spectral signatures for bifurcations of pitchfork type. Indeed, our goal is to study and understand critical changes of almost-invariant/coherent sets. These critical transitions come out as a form of pitchfork bifurcation in the macroscopic consideration of the dynamical system. Indeed, a set-oriented pitchfork bifurcation should practically be equivalent to sudden splitting of rotating gyres/storms/vortices into two.
As illustrated by example 9 and example 10, the statical approach to study classical bifurcations requires the existence of hyperbolic stationary points. However, in the present work, we will study bifurcations while there is no prior existence of hyperbolic stationary points. In other terms, we will study a particular class of Hamiltonian systems whose dynamics mimic a rotating vortex, before a qualitative change occurs. We will then consider elliptic stationary points (i.e., $\mathrm{Re}\,\lambda = 0$ and $\mathrm{Im}\,\lambda \neq 0$) that will bifurcate to become hyperbolic, as a parameter changes. In addition, we will focus on almost-invariant sets generated by the underlying dynamics. Note that, as detailed in chapter 3, the occurrence of almost invariant sets is tight to the existence of dominant eigenvalues. Thus, the set-oriented bifurcation analysis will consider two indicators: changes in the eigenvalues and changes in almost-invariant sets, knowing that those sets are just the corresponding eigenfunctions of the eigenvalues, given the linear operators (see Chapter 3). Under the robustness constraint of almost-invariant sets (see Chapter 3), we will use the diffused operators P_ϵ^t and ultimately $\mathcal{G}_\epsilon$, instead of their deterministic version P^t and $\mathcal{G}$ studied above. Hence, we will look at a spectral signature of the critical transitions, given the diffused operators. However, spectral relations between deterministic and diffused operators will be explored, in order to understand spectral signatures in the diffused setting. We will explore eigenvectors and eigenvalues of these diffused operators by mainly considering eigenvalues whose corresponding eigenvectors approximate almost-invariant sets.

4.3 Almost-invariant sets as eigenfunctions level sets

In this section, we prepare for dealing with the specific dynamics that motivates our research, namely two-dimensional area preserving flows. Here elliptic fixed points are surrounded by periodic solutions forming a family of invariant sets, which we expect to appear as almost-invariant sets for the perturbed dynamics. We will later demonstrate that in order to obtain such almost-invariant sets, it suffices to use the real eigenvalues

and corresponding eigenvectors of the spectrum of the transfer operator P_ϵ^t as defined in chapter 3. We will briefly review some properties of the discrete spectrum of the deterministic operator P^t for general conservative systems before investigating the spectrum of the diffused operator P_ϵ^t. Furthermore, the analysis of almost-invariant sets and their possible bifurcations we will studied and, in this context, the randomly perturbed infinitesimal generator will be used to better confirm found spectral signatures.

4.3.1 Spectrum of the deterministic transfer operator

We suppose that the dynamical system generated by (4.1) is conservative. Therefore, the Frobenius-Perron operator defined in (4.3) becomes

$$P^t f(x) = f(S^{-t}(x)).$$

Thus, P^t is stochastic, meaning that $P^t \mathbf{1}_D = \mathbf{1}_D$, and the Lebesgue measure μ is invariant. In addition, we can restrict the functional domains of P^t and its adjoint, the Koopman operator K^t, to the L^p spaces, $p \geq 1$ [29]. We particularly choose $p = 2$, in order to benefit from the Hilbert space $L^2(D, \Sigma, \mu)$, which allows us to use its scalar product $\langle \cdot, \cdot \rangle_\mu$. Hence, P^t is unitary, meaning $P^{t*} = P^{-t}$, where P^{t*} is the adjoint of P^t. Indeed, $K^t \colon L^2(D, \Sigma, \mu) \to L^2(D, \Sigma, \mu)$ is explicitly defined as $K^t g = g \circ S^t$, for any observable $g \in L^2$. That is $K^t = P^{-t} = P^{t*}$. Thus, K^t maps backward observables, while P^t propagates forward the densities. Beside, due to their isometric properties, the discrete spectrum of the deterministic operators P^t and its adjoint K^t is expressed as

$$P^t f_n = \lambda_n(t) f_n, \text{ whereas } K^t f_n = \overline{\lambda_n(t)} f_n, \ \forall\ t > 0,$$

with $|\lambda_n(t)| = |\overline{\lambda_n(t)}| = 1$. Thus, $||P^t f_n|| = ||f_n|| = ||K^t f_n||$ and eigenfunctions are neither contracted nor expanded but rotated.

The set-oriented approach connects the phase space dynamics to a functional dynamics within a functional space such that every function, or density, is supported on μ-measurable subsets of D. Hence, invariant densities or almost-invariant densities (i.e. $f \in L^2(D, \Sigma, \mu)$ such that $P^t f \approx f$) yield qualitative information of the space dynamics at equilibrium. Let

$$\mathcal{S} = \left\{ f \in L^2(D, \Sigma, \mu) : \ \int_D f d\mu = 0, \ f \neq 0. \right\} \tag{4.13}$$

be the set of all nontrivial functions $f \in L^2(D, \Sigma, \mu)$ that are orthogonal to $\mathbf{1}_D$, under the scalar product $\langle \cdot, \cdot \rangle_\mu$. Let $\overline{f} \in \mathcal{S}$ satisfy the following assumption:

Assumption 11 *There exists a measurable partition of D with partition elements $A_i, i = 1, .., q$, such that*
1. $\overline{f}|_{S^{-t}(A_i)}$ is either positive or negative and if $\overline{f}|_{S^{-t}(A_i)} > 0$ then $\overline{f}|_{S^{-t}(A_{i+1})} < 0$, and vice versa.
2. $P^t\overline{f} \approx \overline{f}$ on A_i, in the sense of the L^2 norm (i.e. $\int_{A_i}(P^t\overline{f} - \overline{f})^2 d\mu \approx 0$).

Then the A_i's form an almost-invariant measurable partition of D, under the following reasoning. Indeed, $\int_D f d\mu = \langle f, \mathbf{1}_D \rangle_\mu = \sum_{i=1}^q \int_{A_i} f d\mu = 0$ and, $\int_{A_i} P^t f d\mu \approx \int_{A_i} f d\mu$ for $i = 1, \ldots, q$, implies $\int_{S^{-t}(A_i)} f d\mu \approx \int_{A_i} f d\mu$. Thus, a possible set-oriented solution for the latter is

$$S^{-t}(A_i) \approx A_i \tag{4.14}$$

wherein it follows

$$\frac{\mu(A_i \cap S^{-t}(A_i))}{\mu(A_i)} \approx 1, \ \forall \ 1 \leq i \leq q.$$

As a result, the A_i's form an almost-invariant measurable partition of D. One sees that for such a real-valued density $\overline{f} \in \mathcal{S}$ with the relation (4.14), the ratio

$$r_t(A_1, A_2, ..., A_q) = \sum_{i=1}^{q} \frac{\mu(A_i \cap S^{-t}(A_i))}{\mu(A_i)} \tag{4.15}$$

is maximized in the sense that $r_t(A_1, A_2, ..., A_q) \approx q$.
We, thus, infer that if there is presence of almost-invariant sets that partition the state space, then we may find almost-invariant densities that belong to $\mathcal{S}$ satisfy assumption 11 and that are supported on those sets. This brings us to the idea of searching for almost-invariant densities in order to identify almost-invariant sets.
Finding densities $\overline{f}$ that satisfy Assumption (11) in realistic systems is intractable. The first step would be to find solutions of the equation

$$P^t f = \delta(t) f \ \text{ where } \ \delta(t) \approx 1,$$

requiring to investigate the discrete spectrum of P^t, which is, however, an analytically hard task. Moreover, the spectrum of P^t does not immediately yield almost-invariant measurable partitions. Indeed, Assumption 11 on the density $\overline{f}$ is not guaranteed by the

eigenfunctions. Moreover, all the corresponding eigenvalues lie on the unit circle. That is, from the discrete spectrum of P^t, the idea of finding almost-invariant sets must be ruled out. Nevertheless, the discrete spectrum of P^t may provide two types of measurable sets: almost-cyclic sets and invariant sets that will later become almost-invariant sets, under external perturbations.
Almost-cyclic sets are measurable sets that undergo a cyclic motion around the elliptic stationary point. Recall that almost-invariant sets, in contrary, are measurable sets that are fixed with respect to the flow map and have the property to lessen transport between their interior and the rest of the phase space. We remind that the dynamical system under investigation consists of rotating orbits around a global elliptic fixed point.
The following remark yields conditions under which eigenfunctions generate almost-cyclic sets.

Remark 12 *Let* $\left\{\lambda_n(t), f_n\right\}_{n\geq 1}$ *be the discrete spectrum of* P^t. *Then* $|\lambda_n(t)| = 1$ *and* $P^t f_n = \lambda_n(t) f_n,\ \forall n \geq 1$, *where* $f_n = f_n^{re} + i f_n^{im}$. *Let us assume that* $\Re e\lambda_n(t) \approx 1$ *while* $\Im m\lambda_n(t) \approx 0$. *Then* $P^t f_n^{re} \approx f_n^{re}$ *and,* $P^t f_n^{im} \approx f_n^{im}$. *Moreover, if* $f_n^{re}, f_n^{im} \in \mathcal{S}$ *and Assumption 11 is satisfied, then* f_n^{re} *and* f_n^{im} *both yield measurable almost-cyclic partitions of* D.

In fact, the push-forward effect of P^t on f_n is only a rotation and, since $\lambda_n(t)$ are complex with a particularity of having $\Re e\lambda_n(t) \approx 1$ while $\Im m\lambda_n(t) \approx 0$, we can deduce that f_n^{re} yields almost-cyclic sets. Denote by

$$\mathcal{E} = \{\Re e\lambda_n(t) :\ \Re e\lambda_n(t) \approx 1,\ n \geq 0\} \tag{4.16}$$

the set of these dominant eigenvalues. These are analytically intractable in general as are the corresponding eigenfunctions, which are indicators of almost-cyclic sets. Instead, we will later consider the diffused operator P_ϵ^t, which can be numerically approximated and its spectrum can be investigated.
Note that, in the present chapter, we study the spectral signature of the bifurcation of the system described above, with a high presence of almost-invariant sets.

4.3.2 Deterministic spectrum and invariant sets

In this section we are going to show that there exist particular eigenfunctions with eigenvalues $\lambda_n(t) = 1$ that are supported on invariant measurable sets partion which describe

the deterministic dynamics of the system we are studying. Moreover, these measurable sets yield measurable almost invariant sets partition, when external perturbations is added to the system's dynamics.
In order to construct an invariant set partition of the deterministic system (without perturbations), we are going to use the Hamiltonian function

$$\begin{aligned} &\Psi_p \colon D \to [a,\, b] \\ &(x, y) \mapsto \Psi_p(x, y), \end{aligned} \tag{4.17}$$

which generates the two-dimensional area-preserving system 4.1. The latter generates a dynamical system completely described by the 1-degree of freedom scalar function (4.17), the Hamiltonian. In addition, the value of the Hamiltonian function is constant along the trajectory $\left\{S^t(\cdot),\ t \geq 0\right\}$. That is, every closed orbit can be mapped to a single value of $\Psi_p(\cdot, \cdot)$. Thus, one can think of the Hamiltonian as a smooth function which lifts the phase space into the interval $[a,\, b]$. Hence, for every $a_i \in [a,\, b]$, there exist a closed orbit $\left\{S^t(x_i),\ t \geq 0\right\} \subset D$ such that $\left\{S^t(x_i),\ t \geq 0\right\} = \Psi_p^{-1}(a_i)$. As a consequence, let us partition $[a,\, b]$ into N disjoint sub intervals $I_i,\ i = 1, ..., k$ and build the measurable sets

$$A_i(p) = \Psi_p^{-1}(I_i),\ i = 1, ..., k. \tag{4.18}$$

As a results, every $A_i(p)$ is composed of closed orbits and $A_i(p) \cap A_j(p) = \emptyset,\ j \neq i$ with $S^{-t}(A_i(p)) = A_i(p),\ i = 1, ..., k$. In this way, we have a measurable partition of D into rings-like patterns with a particular invariant set

$$\overline{A}_h(p) = \Psi_p^{-1}(\overline{I}_h), \tag{4.19}$$

which is supported on a neighborhood of the fixed point and surrounded by all the other rings $A_i,\ i \neq h$. In fact, (4.19) can be understood as a macroscopic representation of the fixed point. Note that this partitioning is not unique and the trivial case consists of a partition with an infinite number of closed orbits. That corresponds to the case where each I_i is a singleton. However, since we are looking at the macroscopic dynamics, we can set the number of partitions k to be finite.
Now we are going to construct stationary eigenfunctions whose level sets yield the invariant partition $A_i(p),\ i = 1, ..., k$.

For $i = 1, ..., k$, we define the functions

$$\psi_i(x) = \mathbf{1}_{A_i(p)}(x) = \begin{cases} 1 & \text{if} \quad x \in A_i(p) \\ 0 & \text{if} \quad x \notin A_i(p). \end{cases} \tag{4.20}$$

Then, we have that $\{\psi_1, \psi_2, ..., \psi_k\}$ are eigenfunctions of $P^t,\ t \geq 0$ with eigenvalue $\lambda(t) = 1$. Indeed,

$$P^t\psi_i = P^t\mathbf{1}_{A_i(p)} = \mathbf{1}_{A_i(p)} \circ S^{-t} = \mathbf{1}_{S^t(A_i(p))} = \mathbf{1}_{A_i(p)}.$$

Note that $D = \bigcup_{i=1}^k A_i(p)$ and $P^t\mathbf{1}_D = P^t\left(\mathbf{1}_{A_1(p)} + \mathbf{1}_{A_2(p)} + ... + \mathbf{1}_{A_k(p)}\right) = P^t\mathbf{1}_{A_1(p)} + P^t\mathbf{1}_{A_2(p)} + ... + P^t\mathbf{1}_{A_k(p)} = \mathbf{1}_{A_1(p)} + \mathbf{1}_{A_2(p)} + ... + \mathbf{1}_{A_k(p)} = \mathbf{1}_D$. Thus, $\mathbf{1}_D$ is also an eigenfunction of eigenvalue 1, we refer to it as the trivial eigenfunction.
Let us consider the subspace $\mathcal{E}_1$ of the eigenspace corresponding to the eigenvalue 1 and spanned by only the eigenfunctions $\{\psi_1, \psi_2, ..., \psi_k\}$. Then $\mathcal{E}_1 \subset L^2$ with $\dim \mathcal{E}_1 = k$. That is, every element $f \in \mathcal{E}_1$ is a linear combination of the functions (4.20) with coefficients in $\mathbb{R}$. Moreover, the functions ψ_i are orthogonal, i.e. $\langle \psi_i, \psi_j \rangle_\mu = 0,\ i \neq j$. Hence, let $\mathcal{V}_1 = \{\phi_1, \phi_2, ..., \phi_k\}$ be an orthogonal basis of $\mathcal{E}_1$. That is,

$$\phi_i = \sum_{j=1}^{k} \alpha_{ij}\psi_j,\ i = 1, ..., k,\ \alpha_{ij} \in \mathbb{R}. \tag{4.21}$$

It follows that the basis elements (4.21) of $\mathcal{V}_1$, i.e. $\{\phi_1, \phi_2, ..., \phi_k\}$, are also eigenfunctions of P^t with eigenvalue 1. Indeed, $P^t\phi_i = \sum_{j=1}^k \alpha_{ij}P^t\psi_j = \sum_{j=1}^k \alpha_{ij}\psi_j = \phi_i$. Moreover, to each $\phi_i,\ i = 1, ..., k$, we have the vector-wise correspondence

$$\phi_i \mapsto (\alpha_{i1}, \alpha_{i2}, ..., \alpha_{ik}), \tag{4.22}$$

and the invariant measurable sets $\{A_j(p),\ j = 1, ..., k\}$ can be obtained from the level sets of the basis elements $\phi_i,\ i = 1, ..., k$. Indeed, let us consider the negative level sets $\{\phi_i < 0\}$, for instance. We have then

$$\phi_i < 0 = \{x :\ \phi_i(x) < 0\} = \{x \in D :\ \alpha_{ij} < 0 :\ j = 1, ..., k\},$$

which is equivalent to

$$\{x :\ \phi_i(x) < 0\} = \{A_j(p),\ \text{such that}\ \alpha_{ij} < 0 :\ j = 1, ..., k\}.$$

For positive level sets $\{\phi_i > 0\}$, we have

$$\{x : \phi_i(x) > 0\} = \{A_j(p), \text{ such that } \alpha_{ij} > 0 : \ j = 1, ..., k\}.$$

Equation (4.22) may be written in terms of sign patterns. That is, for $i = 1, ..., k$,

$$\phi_i \mapsto (\text{sgn}(\alpha_{i1}), \text{sgn}(\alpha_{i2}), ..., \text{sgn}(\alpha_{ik})). \tag{4.23}$$

Given ϕ_i and (4.23) and the sign pattern structure of the coefficients, it may be possible to classify the measurable invariant partitions $\{A_i(p), \ i = 1, ..., k\}$ into aggregates of measurable partitions. For instance, if

$$(\text{sgn}(\alpha_{i1}), \text{sgn}(\alpha_{i2}), ..., \text{sgn}(\alpha_{ik})) = (+, +, +, ..., -, -, -, ..., -) \tag{4.24}$$

with n^+ the number of successive positive sign coefficients and n^- the number of successive negative sign coefficients satisfy $n^+ + n^- = k$, we have that

$$\mathcal{C}_1 = \bigcup_{j=1}^{n^+} A_j(p)$$

and

$$\mathcal{C}_2 = \bigcup_{j=n^++1}^{n^-} A_j(p)$$

are aggregates of measurable invariant sets. Hence, $\mathcal{C}_1$ and $\mathcal{C}_2$ partition D into two measurable

$$(\text{sgn}(\alpha_{i1}), \text{sgn}(\alpha_{i2}), ..., \text{sgn}(\alpha_{ik})) = (+, -, +, -, ..., +, -, +, ...) \tag{4.25}$$

and

$$\mathcal{C}_j = A_j(p), \ j = 1, ..., k.$$

The coarsest aggregates correspond to a single sign pattern structure corresponding to all positive or all negative entries. That is,

$$\begin{aligned}(\text{sgn}(\alpha_{i1}), \text{sgn}(\alpha_{i2}), ..., \text{sgn}(\alpha_{ik})) &= (+, +, +, ..., +, +, +, ...) \\ &= (-, -, -, ..., -, -, -, ...)\end{aligned} \tag{4.26}$$

and in both cases

$$\mathcal{C} = \bigcup_{j=1}^{k} A_j(p) = D.$$

Therefore, as illustrated in (4.24), (4.25), and (4.26), we can restrict ourselves to the signs of α_{ij} to find aggregates of invariant measurable sets. That is, signs matter more than their corresponding entries. Note that we assume the α_{ij} be non-zero. Besides, the need of aggregates of measurable sets comes naturally from set-oriented approach for finding maximal slowly mixing regions [36].
Equation (4.26) is particularly important, since we can then assume the entries α_{ij} in (4.26) to be all equal to one. Let ϕ_1 be the corresponding eigenfunction. Hence, $\phi_1 = \mathbf{1}_D$ and $\mathcal{V}_1 = \{\phi_1, \phi_2, ..., \phi_k\} = \{\mathbf{1}_D, \phi_2, ..., \phi_k\}$ with $\langle \phi_i, \phi_j \rangle_\mu = 0,\ i \neq j$. As a result, we have

$$\int_D \phi_i d\mu = 0,\ \phi_i \neq 0,\ \text{ and } \phi_i \in L^2(D, \Sigma, \mu),\ \text{ for } i = 2, ..., k. \tag{4.27}$$

Therefore, (4.27) corresponds to (4.13), which means $\phi_i \in \mathcal{S}$, for $i = 2, ..., k$. Note that $\phi_i,\ i = 2, ..., k$ yield measurable invariant sets from their positive/negative level sets. Besides, these invariant sets existed already by construction in (4.18). It is easy to verify that the eigenfunctions $\phi_i,\ i = 2, ..., k$ corresponding to eigenvalue $\lambda(t) = 1$ only satisfy assumption 11(1), since we have $P^t\phi_i = \phi_i$, instead of $P^t\phi_i \approx \phi_i$. From these observations, we are going to systematically perturb the system so that invariant sets defined above will simply become almost invariant. As we will see in the following, this systematic perturbation will result in an perturbed transfer operator P^t_ϵ. Besides, the spectrum of P^t_ϵ may contain a set of k eigenvalues which are clustered near 1 and and the corresponding eigenfunctions showing a sign pattern structure similar to (4.24), (4.25), and (4.26) but with little variation.

In the following, we demonstrate how the spectral properties of the perturbed operator P^t_ϵ, which is however, dynamically similar to P^t, can be used to obtain actual almost-invariant partitions of the domain D.

4.3.3 Diffused spectrum and almost-invariant sets

The ϵ-perturbation $\epsilon > 0$, which is central to the construction of the operators P^t_ϵ and its adjoint P^{t*}_ϵ, leaves the dynamics undissipated. Indeed, any given density $f \in L^2(D, \Sigma, \mu)$ is initially diffused, rotated by the dynamics, and the resulting density is again diffused at

final time. For more details about the construction of P_ϵ^t, we refer the reader the chapter 3. Therefore, we have

$$P_\epsilon^t f = \mathcal{D}_\epsilon P^t \mathcal{D}_\epsilon f, \text{ whereas } P_\epsilon^{t*} f = \mathcal{D}_\epsilon^* K^t \mathcal{D}_\epsilon^* f, \ \forall\, t > 0.$$

In particular, it follows immediately that the eigenfunctions of P_ϵ^t and P_ϵ^{t*} are the specific densities $\phi_n \colon L^2(D, \Sigma, \mu) \to \mathbb{C}$ that satisfy the following relations

$$P_\epsilon^t \phi_n^\epsilon = \lambda_n^\epsilon(t)\phi_n^\epsilon \text{ and } P_\epsilon^{t*}\phi_n = \overline{\lambda_{\mathrm{n}}^\epsilon(\mathrm{t})}\phi_n^\epsilon, \ \forall\, t > 0 \tag{4.28}$$

with $|\lambda_n^\epsilon(t)| = |\overline{\lambda_{\mathrm{n}}^\epsilon(\mathrm{t})}|$. As a consequence, the two operators P_ϵ^t and its dual agree in the subset of real eigenvalues, since eigenfunctions are the same.
We are interested in almost-invariant sets as supports of eigenfunctions of P_ϵ^t as well as their corresponding eigenvalues, under the perturbed dynamics. That is, we are going to characterize spectral signatures of bifurcations exhibited by the underlying system. We are, thus, going to shed light on the spectral property of P_ϵ^t, before any spectral bifurcation analysis.

Proposition 13 *Any non-zero real eigenfunction $\phi^\epsilon \neq \mathbf{1}_D \in L^2(D, \Sigma, \mu)$ of P_ϵ^t with corresponding real eigenvalue $\lambda^\epsilon(t)$ belongs to $\mathcal{S}$ defined in (4.13). Furthermore, its corresponding eigenvalue, $\lambda^\epsilon(t)$, satisfies the following inequality*

$$2 - 2\sqrt{(1 - \lambda^\epsilon(t))} \leq \sup_{A \subset D} r^\epsilon(A) \leq 1 + \lambda^\epsilon(t), \tag{4.29}$$

whenever $\lambda^\epsilon(t) < 1$ is the largest real eigenvalue of P_ϵ^t.

Proof 14 *From chapter 3, we have*

$$Q_\epsilon^t \phi = \frac{P_\epsilon^t + P_\epsilon^{t*}}{2}\phi = \frac{\lambda^\epsilon(t)\phi + \lambda^\epsilon(t)\phi}{2} = \lambda^\epsilon(t)\phi$$

thus, $\lambda^\epsilon(t) \in \sigma(Q_\epsilon^t)$ and due to the orthogonality of the eigenfunctions of Q_ϵ^t, it follows that $\int_D \phi d\mu = 0$, or $\phi \perp \mathbf{1}_D$
As detailed in chapter 3,

$$\lambda_2 = \max_{f \neq 0} \left\{ \frac{\langle Q_\epsilon^t f, f\rangle}{\|f\|_\mu^2} \quad \langle f, \mathbf{1}_D\rangle = 0 \right\}.$$

and we have

$$\max_{f\neq 0}\left\{\frac{\langle Q_\epsilon^t f,f\rangle}{\|f\|_\mu^2},\quad \langle f,\mathbf{1}_D\rangle=0\right\}=\max_{f\neq 0}\left\{\frac{\langle \frac{P_\epsilon^t+P_\epsilon^{t*}}{2}f,f\rangle}{\|f\|_\mu^2},\quad \langle f,\mathbf{1}_D\rangle=0\right\},$$
$$=\frac{1}{2}\max_{f\neq 0}\left\{\frac{\langle P_\epsilon^t f,f\rangle}{\|f\|_\mu^2}+\frac{\langle P_\epsilon^{t*} f,f\rangle}{\|f\|_\mu^2},\quad \langle f,\mathbf{1}_D\rangle=0\right\}.$$

Thus

$$\lambda_2\leq\frac{1}{2}\max_{f\neq 0}\left\{\frac{\langle P_\epsilon^t f,f\rangle}{\|f\|_\mu^2},\quad \langle f,\mathbf{1}_D\rangle=0\right\}+\frac{1}{2}\max_{f\neq 0}\left\{\frac{\langle P_\epsilon^{t*} f,f\rangle}{\|f\|_\mu^2},\quad \langle f,\mathbf{1}_D\rangle=0\right\}.$$

Note that, with the the chosen diffusion, $\lambda_1^\epsilon(t)=1$ is a simple eigenvalue of both P_ϵ^t and P_ϵ^{t*} with corresponding eigenfunction $\phi_1=\mathbf{1}_D$. Hence, the right hand side of the above inequality seeks the largest eigenvalue $\lambda^\epsilon(t)$ such that $\phi_n\perp\mathbf{1}_D$, or $\int_D\phi_n d\mu=0$.
It follows that

$$\lambda_2\leq\frac{\lambda^\epsilon(t)+\lambda^\epsilon(t)}{2}=\lambda^\epsilon(t).$$

Recall that λ_2 yields the inequality $2-2\sqrt{(1-\lambda_2)}\leq\sup_{A\subset D}r^\epsilon(A)\leq 1+\lambda_2$ [36]. Hence, substituting λ_2 by $\lambda^\epsilon(t)$, we obtain (4.29).

One possibility of achieving a measurable partition is to consider the threshold 0, then set $A^+=\operatorname{supp}\{\phi>0\}$ and $A^-=\operatorname{supp}\{\phi\leq 0\}$. This is indeed the threshold we will consider in this study. Thus, $\{A^+,\ A^-\}$ yields a measurable balanced partition of D whenever $\lambda^\epsilon(t)$ is close to 1. It is clear by now that only real eigenfunctions and corresponding eigenvalues of P_ϵ^t are potential candidates to generate almost invariant partitions. Indeed, a partition of almost-invariant sets can only be done we eigenvalues of Q_ϵ^t, [16, 36].

Corollary 15 *All real eigenfunctions of P_ϵ^t are orthogonal.*

In other words, corollary 15 is highlighting the fact that the subset of real eigenvalues of P_ϵ^t and their corresponding eigenfunctions are contained in the spectrum of Q_ϵ^t which is composed of orthogonal eigenfunctions.

Let us denote by $\mathcal{S}'=\left\{\phi_n^\epsilon\right\}_{n=1}^N$ the finite set of real eigenfunctions of P_ϵ^t. We choose to order the corresponding eigenvalues $\{\lambda_n^\epsilon(t)\}_{n=1}^N$ as $1=\lambda_1^\epsilon(t)>\lambda_2^\epsilon(t)\geq\cdots\geq\lambda_N^\epsilon(t)$.

Hence, $\phi_1 = \mathbf{1}_D$, the eigenfunction ϕ_2^ϵ yields the existing optimal almost-invariant partition of D into two measurable sets, and λ_2 satisfies (4.29).

Corollary 16 *Any eigenfunction ϕ_n^ϵ $n \geq 2$, generates at least a measurable n-partition of D in the sense that*

$$\text{supp}\,\{\phi_n > 0\} = \cup_{i=1}^{n^+} A_i^+ \;\; \textit{and} \;\; \text{supp}\,\{\phi_n \leq 0\} = \cup_{i=1}^{n^-} A_i^-,$$

with $n = n^+ + n^-$.

This follows directly from the orthogonality of the eigenfunctions as stated in corollary 15. Let us suppose that $N = k$ and that P_ϵ^t has a $k \geq 2$ distinct eigenvalues $\{\lambda_1^\epsilon(t), ..., \lambda_k^\epsilon(t)\}$ clustered near $\lambda^\epsilon(t) = 1$ and each has a geometric multiplicity which is equal to one. Then $\mathcal{S}' = \{\phi_i^\epsilon,\ i = 1, ..., k\}$ are mutually orthogonal, from corollary 15. Moreover, the eigenfunctions $\{\phi_i^\epsilon,\ i = 2, ..., k\}$ are all elements of $\mathcal{S}$ defined in (4.13), given that $\phi_1^\epsilon = \mathbf{1}_D$. Finally corollary 16 stated that eigenfunctions $\{\phi_i^\epsilon,\ i = 2, ..., k\}$ yield almost-invariant partitions.

It is worth mentioning that it is highly unlikely to find an analytical relationship between the eigenfunctions $\{\phi_i^\epsilon,\ i = 2, ..., k\}$ from the perturbed dynamics and the eigenfunctions $\{\phi_i,\ i = 1, ..., k\}$ defined in (4.21) from the unperturbed dynamics, except the trivial eigenfunction $\phi_1^\epsilon = \phi_1 = \mathbf{1}_D$. However, note that the perturbation used here is discontinuous because it only incorporates diffusion at initial and final time. Thus, with this type of diffusion, invariant sets or aggregates of invariant sets, such as (4.24), (4.25), (4.26), are simply inflated in the order of the diffusion amplitude ϵ. We can then propose a formula for the diffused eigenfunctions in the following way:

$$\phi_i^\epsilon = \phi_i + \epsilon h_i + O(\epsilon^2),\ \ i = 2, ..., k, \tag{4.30}$$

where ϕ_i is defined in (4.21), $h_i = \sum_{j=1}^k \beta_{ij}\psi_j,\ j = 1, .., k,\ \beta_{ij} \in \mathbb{R}$. With this formula, we can see that $\phi_i^\epsilon = \phi_i$, whenever the diffusion amplitude ϵ is zero. The latter corresponds to the deterministic dynamics where only invariant sets are present. If ϵ is a small

amplitude, then the pattern structure of ϕ_i^ϵ can be understood by rewriting (4.30) as

$$\begin{aligned}\phi_i^\epsilon &= \sum_{j=1}^{k} \alpha_{ij}\psi_j + \epsilon \sum_{j=1}^{k} \beta_{ij}\psi_j + O(\epsilon^2) \\ &= \sum_{j=1}^{k} (\alpha_{ij} + \epsilon\beta_{ij})\, \psi_j + O(\epsilon^2).\end{aligned} \tag{4.31}$$

for $i = 2, ..., k,\ j = 1, ..., k$ and $\alpha_{ij},\ \beta_{ij},\ \in \mathbb{R}$. Similar to (4.22), we have the vector-wise correspondence of $\phi_i^\epsilon,\ i = 1, ..., k$ as

$$\phi_i^\epsilon \mapsto (\alpha_{i1}^\epsilon, \alpha_{i2}^\epsilon, ..., \alpha_{ik}^\epsilon)\,, \tag{4.32}$$

and

$$\phi_i^\epsilon \mapsto (\text{sgn}\,(\alpha_{i1}^\epsilon)\,, \text{sgn}\,(\alpha_{i2}^\epsilon)\,, ..., \text{sgn}\,(\alpha_{ik}^\epsilon))\,, \tag{4.33}$$

with $\alpha_{ij}^\epsilon = \alpha_{ij} + \epsilon\beta_{ij} + O(\epsilon^2)$. Indeed, the entries α_{ij}^ϵ in (4.32) are obtained form the entries of (4.22) by adding a forward or backward shift $\epsilon\beta_{ij}$ and a limiting term $O(\epsilon^2)$. Adding the latter terms does not bring changes in the sign pattern structure of (4.32) compared to (4.22). Indeed, note that with the formula (4.30), we have

$$P^t\phi_i^\epsilon = \phi_i^\epsilon$$

Moreover, it is trivial to show that the deterministic sign structure (4.23) does not change by only shifting the constants α_{ij} with $\epsilon\beta_{ij},\ \ \epsilon \geq 0$ and $O(\epsilon^2)$. Thus, given the constant level patterns α_{ij}^ϵ, there is no significant difference between (4.23) and (4.33). This means that eigenfunctions $\{\phi_i^\epsilon,\ i = 2, ..., k\}$ are supported in the same aggregates as the eigenfunctions $\{\phi_i,\ i = 2, ..., k\}$ with corresponding eigenvalues $\{\lambda_2^\epsilon(t), ..., \lambda_k^\epsilon(t)\}$. The difference is that in the deterministic setting, we have $P^t\phi_i = \phi_i$, while in the perturbed setting $P_\epsilon^t\phi_i^\epsilon = \lambda_i^\epsilon(t)\phi_i^\epsilon,\ 2, ..., k$. The latter means that the eigenfunctions $\{\phi_i^\epsilon,\ i = 2, ..., k\}$ are slightly contracted in all directions by P_ϵ^t and the $\{\lambda_2^\epsilon(t), ..., \lambda_k^\epsilon(t)\}$ are the corresponding contraction rates. Thus, instead of an equality, we can write

$$P_\epsilon^t\phi_i^\epsilon \approx \phi_i^\epsilon,\ i = 2, ..., k. \tag{4.34}$$

As a result, the eigenfunctions $\{\phi_i^\epsilon,\ i = 2, ..., k\}$ satisfy assumption 11 with the diffused transfer operator P_ϵ^t, rather than the deterministic operator P^t. The eigen-

functions $\{\phi_i^\epsilon,\ i = 2, ..., k\}$ yield almost-invariant sets with corresponding eigenvalues $\{\lambda_2^\epsilon(t), ..., \lambda_k^\epsilon(t)\}$ clustered near 1

With this theoretical setting, we are going to numerically approximate P_ϵ^t and proceed to a bifurcation analysis by exploring changes in the spectrum of the numerical operator. A particular focus will be made on the subset of real eigenfunctions with corresponding eigenvalues close to 1. We believe that with the class of dynamical systems we are studying, the existence of real eigenvalues close to 1 is very likely, given the detailed theory above.

4.4 Numerical approximation of the transfer operator

As illustrated in (4.29), the spectrum of the transfer operator is key to identifying almost-invariant sets, but a corresponding analysis of specific mathematical models requires numerical approximations. Here, we propose a discretization of the diffused transfer operator P_ϵ^t based on Ulam's method [22]. Following [13] we subdivide the domain D into disjoints subsets, or boxes $\Big\{B_1, B_2, ..., B_N\Big\}$ of positive volumes. Each box B_i has the same dimension as the domain and all the boxes have same size.

We then approximate the deterministic Perron-Frobenius operator P^t. Let us define $\Delta_N = \langle \mathbf{1}_{B_1}, ..., \mathbf{1}_{B_N} \rangle$ as a $N-$ dimensional subspace of $L^2(D, \Sigma, \mu)$, where μ denotes Lebesgue measure. Let

$$\begin{aligned} \Pi_N \colon L^1(X, \mu) &\to \Delta_N \\ f &\mapsto \Delta_n f = \sum_{j=1}^{N} \left(\frac{1}{\mu(B_i)} \int_{B_i} f d\mu \right) \mathbf{1}_{B_j} \end{aligned}$$

be the L^2-orthogonal projection of $L^2(D, \Sigma, \mu)$ onto Δ_N. Let

$$P_N^t \colon \Delta_N \to \Delta_N, \ \text{ with } \ P_N^t = \Pi_N P^t$$

be the finite-rank approximation of P^t. The matrix representation $\mathcal{P}_N^t$ with respect to the basis $\{\mathbf{1}_{B_1}, ..., \mathbf{1}_{B_N}\}$ is given as

$$P_N^t \mathbf{1}_{B_i} = \sum_{j=1}^{N} \left(\frac{1}{\mu(B_i)} \int_{B_i} P^t \mathbf{1}_{B_i} d\mu \right) \mathbf{1}_{B_j}$$

and finally,

$$\begin{aligned}(\mathcal{P}_N^t)_{ij} &= \frac{\mu(B_i \cap S^{-t}(B_j))}{\mu(B_j)} \\ &= \frac{\mu(B_i \cap S^{-t}(B_j))}{\mu(B_i)}\end{aligned} \tag{4.35}$$

The entries $(\mathcal{P}_N^t)_{ij}$ are numerically estimated by uniformly sampling k test points $\left\{x_i\right\}_{i=1}^{k}$ in each box B_i and computing the transition probabilities between boxes. Thus, each matrix entry is given by

$$(\mathcal{P}_N^t)_{ij} = \frac{\#\{x_i \in B_i \,:\, S^t(x_i) \in B_j\}}{k}$$

In this way, the matrix $\mathcal{P}_N^t$ represents a transition matrix of an N-states Markov chain; the states are given by the boxes B_i, $i = 1, .., N$. Moreover, the entry $(\mathcal{P}_N^t)_{ij}$ represents the conditional probability that a randomly chosen point in B_i lands in B_j at time t after application of the flow S^t.
$\mathcal{P}_N^t$ is row stochastic and has a leading eigenvalue 1. Even though, we are more interested in the finite dimensional version of the diffused transfer operator P_ϵ^t, it is enough to use the matrix $\mathcal{P}_N^t$. Indeed, the numerical method used to compute $\mathcal{P}_N^t$ adds sufficient numerical diffusion with ϵ being of the order of box size. So it suffices to directly use $\mathcal{P}_N^t$ as a numerical approximation of P_ϵ^t.

4.5 Simple example systems

As already mentioned above, we are interested in specific types of conservative systems. Motivated by the Antarctic polar vortex dynamics figure 1.1, we are going to consider two-dimensional area-preserving systems that, a priori, exhibit a global elliptic stationary point. Hence, the dynamical behavior is characterized by rotating orbits around that global elliptic stationary point. We will study numerically approximated almost-invariant patterns. Moreover, we will explore the spectral signature of the bifurcation of almost-invariants sets. Under this supposition, the discrete spectra of the deterministic Frobenius-Perron operator P^t and their adjoint K^t are given by

$$P^t f_n = e^{i\omega_n t} f_n, \;\; \text{whereas} \;\; K^t f_n = e^{-i\omega_n t} f_n, \;\; \forall\; t > 0.$$

Thus, eigenfunctions are periodically propagated with period $\frac{2\pi}{\omega_n t}$ by P^t and K^t forward and backward, respectively.

4.5.1 Harmonic oscillator

As a first numerical investigation, we consider the harmonic oscillator

$$\begin{aligned} \dot{x} &= y \\ \dot{y} &= -\omega^2 x \end{aligned} \tag{4.36}$$

The stationary point $(0,0)$ is a stable center and trajectories form a family of ellipses centered at $(0,0)$ for each parameter $\omega \neq 0$. This system can be viewed as a simple toy model of an ocean or atmospheric eddy. The solution of the flow is given by

$$\begin{aligned} x(t) &= x_0 \cos(\omega t) + \frac{y_0}{\omega} \sin(\omega t) \\ y(t) &= y_0 \cos(\omega t) - x_0 \omega \sin(\omega t) \end{aligned} \tag{4.37}$$

and the Hamiltonian/streamfunction is given by

$$\Psi(x,y) = x^2 + \frac{y^2}{\omega^2} + C, \;\; C \in \mathbb{R} \tag{4.38}$$

In order to determine the discrete spectrum of the deterministic transfer operator P^t, we use the continuity equation of (4.5) and solve the following equation in ρ with $\lambda \in \mathbb{C}$

$$y \frac{\partial \rho}{\partial x} - \omega^2 x \frac{\partial \rho}{\partial y} = \lambda \rho.$$

$\rho(x,y) = (x - i\frac{y}{\omega})^n$ solves the above equation $\forall\ n \geq 0$ with $\lambda = in\omega$, which are the eigenvalues of the infinitesimal generator $\mathcal{G}$. Therefore, by the spectral mapping theorem (4.6), the discrete spectrum of the Perron-Frobenius operator P^t is given by $\lambda_n(t) = e^{in\omega t},\ \forall\ t > 0$, so all the eigenvalues lie on the unit circle. The corresponding eigenfunctions are the same as those of the generator, i.e. $\phi_n(x,y) = (x - i\frac{y}{\omega})^n$, which we rewrite as $\phi_n(x,y) = (x^2 + \frac{y^2}{\omega^2})^n e^{in\theta}$ with $\theta = \arctan(-\frac{y}{x\omega})$.
Moreover, as detailed in section 4.3.2 (equation (4.21)), the spectrum of P^t contains a finite number of orthogonal real eigenfunctions, denoted $\{\phi_i',\ i = 1, ..., k\}$ with eigenvalue 1, which are constructed from the Hamiltonian (4.38). These eigenfunctions, by construction, are supported on the invariant ring-like patterns, given the circular behavior of the flow.

Now, let us assume that $\mathrm{Re}\,\lambda_n(t) \approx 1$. Then $\sin(n\omega t) \approx 0$ and it follows that

$$n\omega t \approx 2m\pi, \;\; m \in \mathbb{Z}.$$

As a consequence, if m is a multiple of n, then the system of solutions (4.37) yields the almost stationarity relation

$$(x(t), y(t)) \approx (x_0, y_0) \text{ with } t \neq t_0. \tag{4.39}$$

Indeed, it is enough to substitute wt by $\frac{2m\pi}{n}$ into the equations in (4.37) to obtain (4.39). Moreover, with respect to the spectrum we immediately have that the corresponding eigenfunction ϕ_n satisfies $P^t\phi_n \approx \phi_n$. This means, $P^t\left[(x^2+\frac{y^2}{\omega^2})^n\cos(n\theta)\right] \approx (x^2+\frac{y^2}{\omega^2})^n\cos(n\theta)$ and $P^t\left[(x^2+\frac{y^2}{\omega^2})^n\sin(n\theta)\right] \approx (x^2+\frac{y^2}{\omega^2})^n\sin(n\theta)$.
we are going to numerically show that the positive and negative level sets of the latter partition the domain D into almost-cyclic sets, given the almost stationarity relation (4.39). On the other hand, we are going to numerically show that the diffused eigenfunctions $\{\phi_i'^{\epsilon},\ i = 1, ..., k\}$ of the diffused transfer operator P_ϵ^t, which are constructed in (4.31) from the deterministic eigenfunctions $\{\phi_i',\ i = 1, ..., k\}$, are supported on almost-invariant ring-link patterns with eigenvalues clustered near 1.
The system (4.36) is integrated with a fixed flow time 1 using a RungeKutta scheme of fourth order and studied in the space domain $[-2,\, 2] \times [-2,\, 2]$. The latter is subdivided into 2^{13} equals subdomains with 900 uniformly distributed test points in each subdomain. Thus, we compute the transition matrix approximation of the infinite dimensional operator P_ϵ^t. Note that diffusion of amplitude ϵ is artificially including from the numerical discretization. In fact, the diffusion amplitude is equal to the size of a subdomain. Finally note that the system (4.36) is open. That is, trajectories of test points may leave the considered domain at final time integration. To numerically overcome this computational obstacle, an additional box is added in order to capture all the image points that are being mapped out of the initial domain D when computing the transition matrix. At the end of the computation, this temporary subdomain will be removed from the eigenvector entries by just considering the 2^{13} first entries.

In Figure 4.6 we have plotted the largest magnitude eigenvalues of the approximated diffused transfer operator P_ϵ^t in the left panel. The right panel shows the largest real part eigenvalues. The numerical spectrum was computed for a fixed parameter $\omega = 1$.

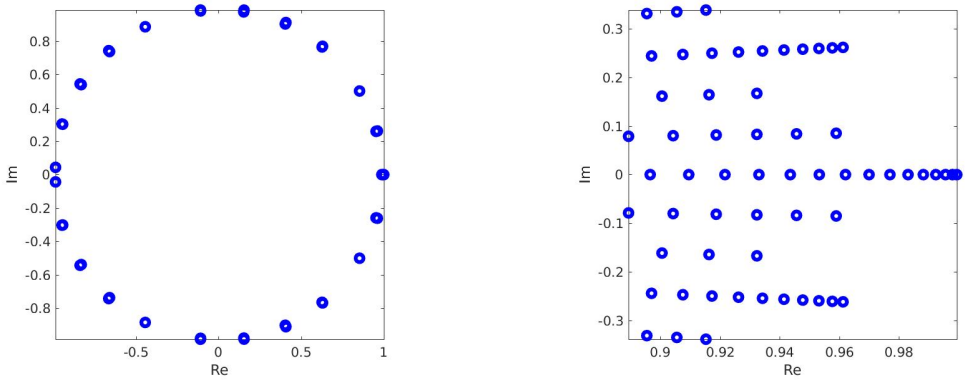

Figure 4.5: Largest magnitude (left) and largest real part eigenvalues (right) for the linear flow with parameter choice $\omega = 1$.

As shown in figure 4.5, we have a cohabitation between strictly real eigenvalues clustered near the eigenvalue 1 and complex eigenvalues which have, among them, complex eigenvalues with real parts close to 1. The latter yield almost-cyclic sets in figure 4.6 in agreement with remark 12, while the former yield ring-like patterns in figure 4.7 as predicted by our study in section 4.3.3.
In figure 4.7(a)-(d), note the center pattern defined in (4.19), which is present in every eigenvector pattern. The pattern (4.19) carries the qualitative behaver of the center fixed point $(0, 0)$. This is a qualitatively important difference with eigenvectors patterns in figure 4.6, as the latter only cycle around the fix point $(0, 0)$. It may be very helpful to keep this in mind for a better understanding of results in the upcoming chapters. Indeed, when the fixed point $(0, 0)$ bifurcates, it may be more logical to investigate the set oriented response of the bifurcation in the real eigenvectors in figure 4.7 than in the complex eigenvectors in figure 4.6.

4.5.2 One-dimensional circle dynamics

Let us now consider a macroscopic approach of the circle dynamics

$$\dot{\theta} = \omega \tag{4.40}$$

This can be interpreted as viewing one periodic orbit in a two-dimensional system. In this study we illustrate the lack of possibility to construct the real eigenfunctions (4.21) and their diffused version (4.31) from the Hamiltonian function (4.17). Indeed, we will show that the only real eigenvalue that one can find is the trivial eigenfunction with

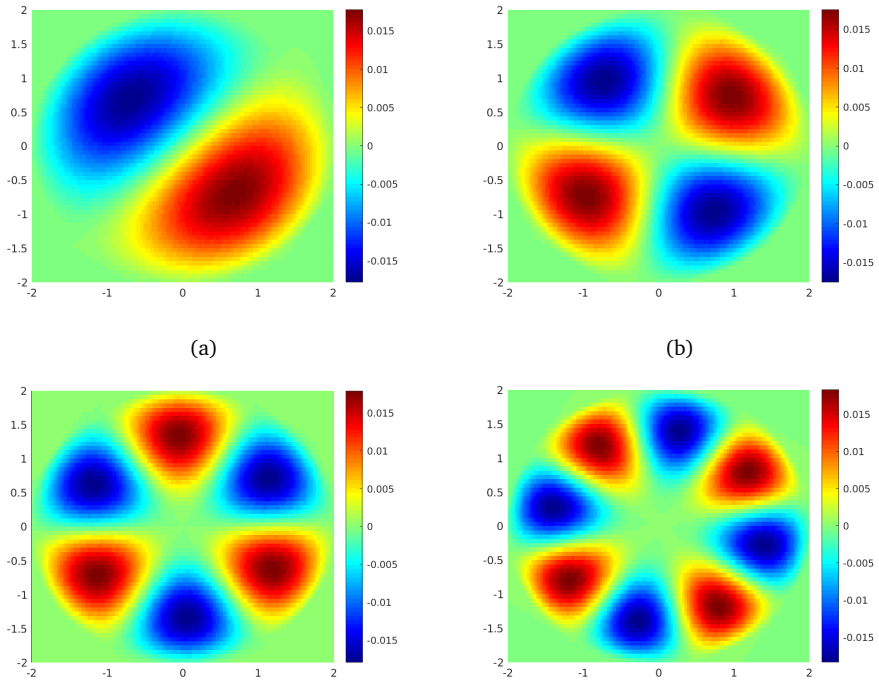

Figure 4.6: Approximations of the leading complex eigenvectors of the transfer operator for the linear flow for $\omega = 1$ exhibit spatially-periodic pattern that partition the domain into almost-cyclic sets.

corresponding eigenvalue 1. Therefore, the diffused transfer operator yields the same eigenfunction with eigenvalue one. However, almost-cyclic sets can always be obtained from eigenfunctions with eigenvalues whose real parts are close to 1 and imaginary part close to 0.

Given any initial angle $\theta \in [0, 2\pi)$, the flow S^t is given by

$$S^t(\theta) = \omega t + \theta \mod 2\pi, \tag{4.41}$$

the Lebesgue measure μ is invariant under S^t. Then $P^t f(\theta) = f \circ S^{-t}(\theta) = f(\theta - \omega t)$ and any point $z(\theta) \in \mathbb{S}^1$ is given by $z(\theta(t)) = e^{i\theta_t} = e^{i(\theta+\omega t)}$ with $\theta_t = S^t(\theta) = \omega t + \theta \mod 2\pi$. We are able to easily obtain the discrete spectrum of $P^t, t \geq 0$ by taking $f_n(\theta) = z^n = e^{in\theta_t} = e^{in\theta}e^{in\omega t}$. Thus, eigenfunctions and eigenvalues are given by

$$\phi_n(\theta) = e^{in\theta} \text{ and } \lambda_n(t) = e^{in\omega t}, n \in \mathbb{Z}.$$

Note that these eigenfunctions are Fourier basis elements, forming a complete orthogonal

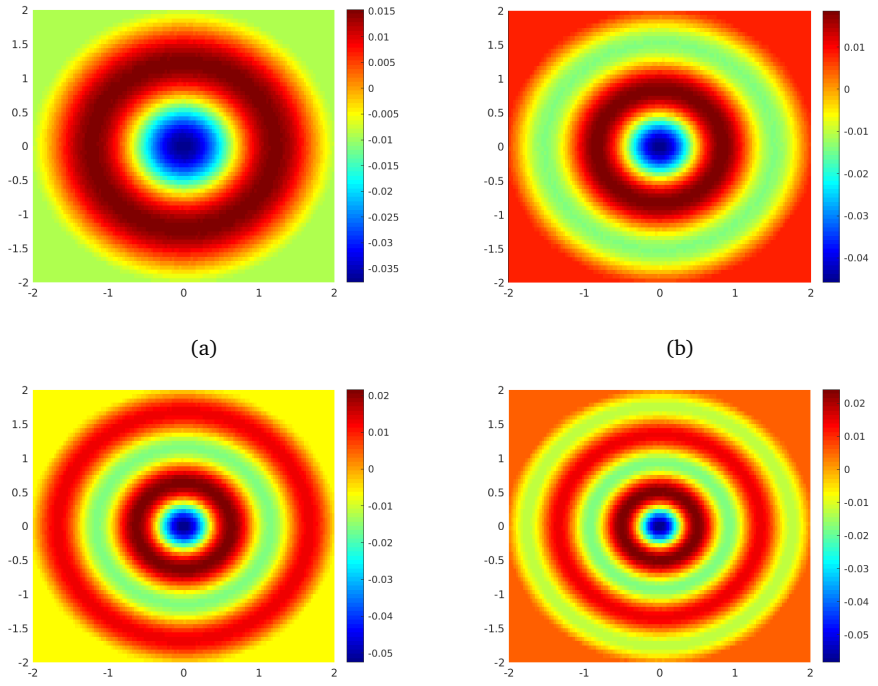

(a) (b)

(c) (d)

Figure 4.7: Approximations of the leading real eigenvectors of the transfer operator for the linear flow for $\omega = 1$ exhibit spatially-periodic patterns that partition the domain into almost-invariant sets.

basis of L^2.

Since $P^t\phi_n(\theta) = \lambda_n(t)\phi_n(\theta)$, we have

$$\begin{aligned} P^t\phi_n(\theta) =& \Big(\cos(n\omega t) + i\sin(n\omega t)\Big)\Big(\cos(n\theta) + i\sin(n\theta)\Big) \\ &= \cos(n\omega t)\cos(n\theta) - \sin(n\omega t)\sin(n\theta) \\ &\quad + i\Big(\cos(n\omega t)\sin(n\theta) + \cos(n\theta)\sin(n\omega t)\Big). \end{aligned}$$

Now, let us suppose that $\mathrm{Re}(\lambda_n(t)) \approx 1$. Then $\sin(n\omega t) \approx 0$, which implies that

$$n\omega t \approx 2k\pi, \quad k \in \mathbb{Z}. \tag{4.42}$$

Hence, due to equation (4.42) we have for (4.41) the almost-stationarity relation

$$\theta(t) \approx \theta_0 \tag{4.43}$$

for the chosen flow time $t > 0$. From (4.43) it is clear that a measurable almost-cyclic partition generated by (4.41) must consist of sub-intervals of $[0, 2\pi)$ of equal length, which are supported on either real or imaginary parts of the eigenfunctions $\phi_n(\theta)$ with corresponding eigenvalues satisfying $\mathrm{Re}(\lambda_n(t)) \approx 1$. Indeed, with respect to the spectrum, we have

$$P^t\phi_n(\theta) \approx \Big(\cos(nt)\cos(n\theta)\Big) + i\Big(\sin(n\theta)\cos(nt)\Big).$$

Therefore, $P^t\cos(n\theta) \approx \cos(n\theta)$ and $P^t\sin(n\theta) \approx \sin(n\theta)$. As stated in Remark 12, for such n satisfying equation (4.42), real part eigenfunctions of P^t_ϵ must be periodic and their level sets partition the domain into sub-intervals of equal length. That is what either $\phi_n = \cos(n\theta)$ or $\phi_n = \sin(n\theta)$ exactly do. Finally, note that besides the trivial eigenvalue 1 with corresponding eigenfunction $\mathbf{1}_D$, one cannot construct the real eigenfunctions (4.21) from the underlying system (4.41). In fact, the Hamiltonian (4.17) cannot be derived from (4.41). Therefore, the spectrum of the diffused operator P^t_ϵ can only yield complex eigenvalues and an eigenvalue 1 with corresponding eigenfunction $\mathbf{1}_D$.
In the following, we are going to give numerical illustrations.
The system (4.41) is, thus, integrated using a RungeKutta scheme of forth order with a fixed flow time of length 1. Thus, (4.41) is studied in the space interval $[0, 2\pi)$. The latter is subdivided into 2^{12} equals sub-intervals with 400 uniformly distributed test points in each sub-interval. Thus, we compute the transition matrix which is the finite dimensional approximation of P^t_ϵ. Recall that diffusion of amplitude ϵ comes in artificially with the numerical discretization.
As expected, the spectrum lies on the unit circle, see Figure 4.8. There is only one real eigenvalue, which is the trivial one, as P^t_ϵ is a stochastic operator. Thus, in the finite dimensional approximation, we have a stochastic matrix whose stationarity distribution is the positive/negative entries (i.e. probability distribution over sub-intervals) eigenvector with eigenvalue 1, see figure 4.9. Moreover, there exists a finite number of eigenvalues with real part close to 1. The real parts of the corresponding eigenvectors are displayed in Figure 4.10 corresponding to approximations of $\cos(n\theta)$. Note that in synchronization with the circle dynamics, both $\cos(n\theta)$ and $\sin(n\theta)$ are oscillations of frequency $2\pi/n$ in the domain $[0, 2\pi)$. Their zero-level sets yield a finite partition of the domain $[0, 2\pi)$.

Consequently, eventual critical transitions of almost-invariant sets will be based on the strictly real spectrum of P^t_ϵ, which is always numerically accessible. As a matter of fact, we will be looking for real eigenfunctions of P^t_ϵ with real eigenvalue close to 1. We

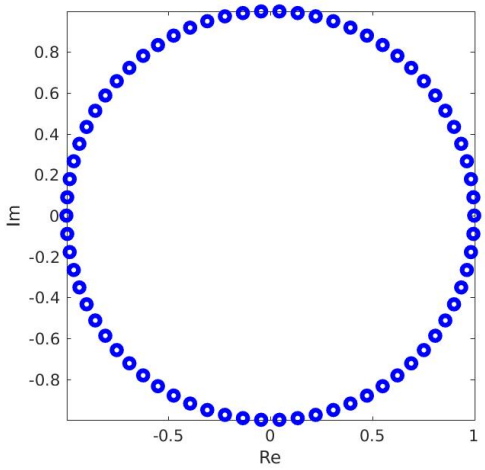

Figure 4.8: The numerically approximated eigenvalues of P_ϵ^t for the circle dynamics with parameters $w = \pi/34$ and $t = 1$.

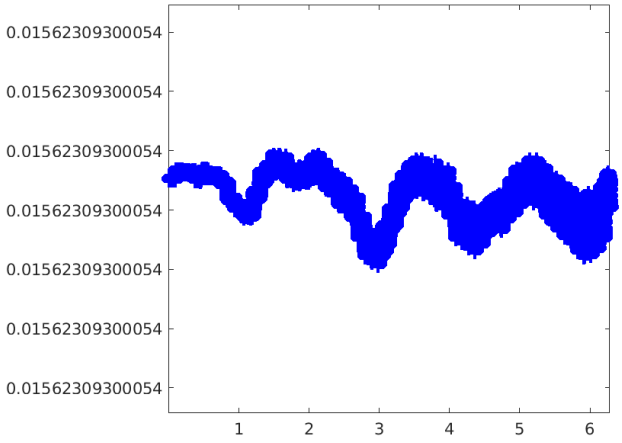

Figure 4.9: Numerically approximated real eigenfunction (stationary distribution) of P_ϵ^t for the circle dynamics with parameters $w = \pi/34$ and $t = 1$.

will then construct almost-invariant sets as the zero-level sets of the eigenfunctions and eventually track the changes of this spectrum with respect to a bifurcation parameter. Special focus will be made on parameter values close to the critical parameter.

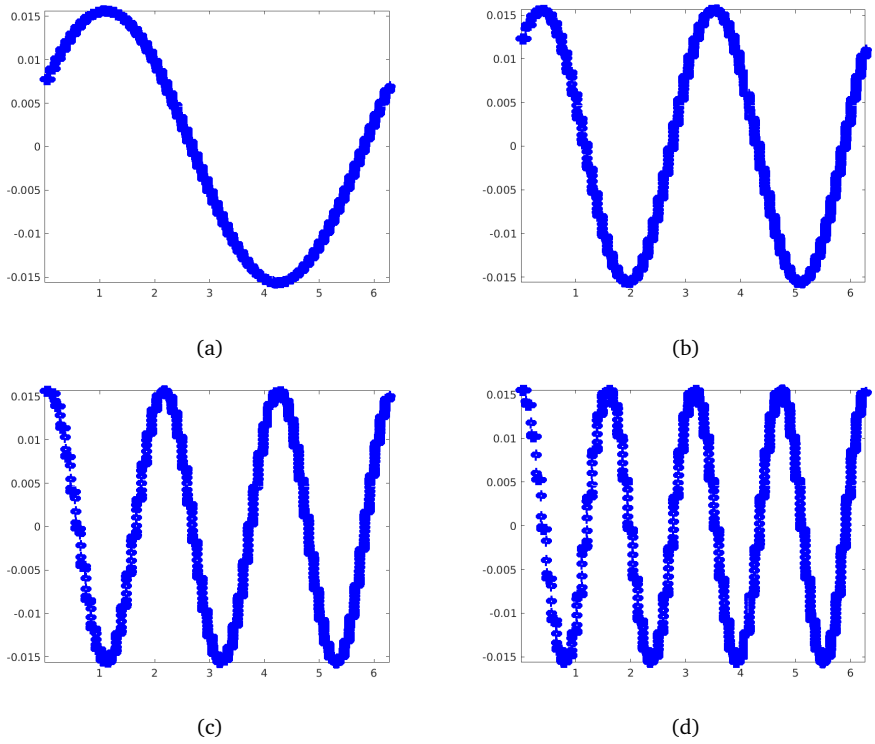

Figure 4.10: Real parts of eigenvectors of the numerical approximation of P_ϵ^t to eigenvalues with real part close to 1 for the circle dynamics with parameters $w = \pi/34$ and $t = 1$.

4.6 Spectral signature for set-oriented bifurcation

The spectrum of the operator P_ϵ^t, is reliable to study the bifurcation of patterns generated by the real spectrum $\mathcal{S}'$. In this section we consider a nonlinear version of (4.36)

$$\begin{aligned} \dot{x} &= y \\ \dot{y} &= px - x^5. \end{aligned} \tag{4.44}$$

For $p \in \mathbb{R}$, the system displays two different stable phases separated by a critical state as shown in Figure 4.11.

The transition from one stable phase to another is referred to as a critical transition. The early indicators before the system shifts to another state are of interest here, mostly referred to as critical slowing down [3]. In the first part of this section we investigate the critical slowing down based on the diffused spectrum, i.e., the spectrum of the operator P_ϵ^t. In the second part, we investigate the same phenomena with a randomly perturbed

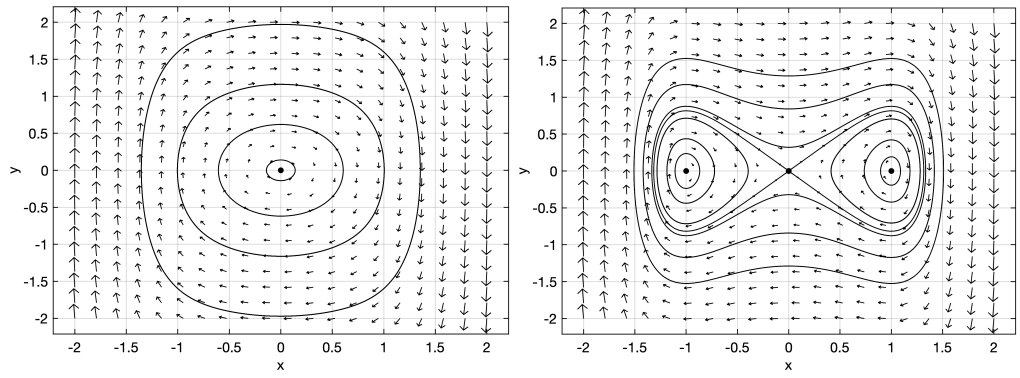

Figure 4.11: Phase plane of system (4.44) for parameters $p = -1$ (left) and $p = 1$ (right).

version of the deterministic infinitesimal generator defined in (4.4).

4.6.1 Transfer operator approach

Now, we are ready to study the spectral signature of the underlying bifurcation with respect to the diffused spectrum of P_ϵ^t. We will show that the transfer operator based approach gives an indication of a bifurcation before the critical parameter is reached. The vector fields before and after the bifurcation is illustrated in Figure 4.11.

System (4.44) clearly undergoes a pitchfork bifurcation of elliptic-type equilibria. When $p \leq 0$, (4.44) has a unique fixed point at the origin. The latter is a stable center. Actually, (4.44) is a nonlinear perturbation of the linear system

$$\begin{aligned} \dot{u} &= v \\ \dot{v} &= pu. \end{aligned} \tag{4.45}$$

When $p \leq 0$, adding the nonlinear term in (4.44) to (4.45) does not change the qualitative behavior of the latter with respect to the former. Indeed, the two dynamical regimes consist only of rotating closed orbits around the stationarity point $(0, 0)$ for negative values of p. Hence, we can say that near a neighborhood of $(0, 0)$, the nonlinear system (4.44) is qualitatively equivalent to (4.36) and (4.45), for negative values of p. Moreover, near $(0, 0)$, the discrete spectrum of the deterministic operator P^t generated by (4.44) may be given by

$$\lambda_n(t, p) = e^{in\sqrt{-p}t}, \ n \geq 0, \ p \leq 0.$$

As mentioned earlier, almost-cyclic partitions require, $\Re e(\lambda_n(t, p)) \approx 1$ while $\Im m(\lambda_n(t, p)) \approx$

0. Let $s_n(t,p) = \Re e\lambda_n(t,p) \approx 1$. Therefore, we focus on

$$s_n(t,p) = \cos(n\sqrt{-p}t) \approx 1$$

and, as in (4.16), we pick all of them in

$$\mathcal{E} = \{s_n(t,p) : \ \ n \geq 0\}. \tag{4.46}$$

Note that, even though $s_n(t,p) \approx 1, \ \forall \ n \geq 0$, there is a decreasing order among them since $s_n(t,p) \neq s_m(t,p)$ when $n \neq m$. Therefore, near the critical parameter p we have that

$$s_n(t,p) \to 1 \text{ as } p \to 0, \ \ \forall \ n \geq 0. \tag{4.47}$$

The spectrum in (4.46) tends to accumulate at 1 when the system is close to the tipping point $p = 0$. This is clearly a spectral version of the critical slowing down scenario [3] which the system faces near the bifurcation. However, (4.47) only concerns the complex eigenvalues of the deterministic operator P^t. Moreover, in example 4.36, it is made clear that studying real eigenvectors in figure 4.7 may be more relevant to characterize the set-oriented bifurcation of the center point $(0,0)$. Indeed, these eigenvectors correspond to real eigenvalues accumulated near 1, as shown in figure 4.5. In the same vein, we are going to study the pitchfork bifurcation by relying on these kind of real eigenvalues. Their existence should be shown first.
Indeed, we have the Hamiltonian of (4.44)

$$\rho(x,y) = \frac{1}{2}y^2 - \frac{p}{2}x^2 + \frac{1}{6}x^6 + C \tag{4.48}$$

with which we can construct k orthogonal real eigenfunctions $\{\phi'_i, \ i = 1, ..., k\}$ with eigenvalue 1 of the deterministic operator P^t. Note that these eigenfunctions are the concrete realizations of (4.21). They are, thus, supported on ring-like invariant sets, given the circular behavior of the phase space of (4.44), see figure 4.11 (left panel). As shown in section (4.3.3), under the diffused dynamics, the transfer operator P^t_ϵ yields k orthogonal eigenfunctions $\{\phi'^\epsilon_i, \ i = 1, ..., k\}$ with corresponding eigenvalues $\{\lambda^\epsilon_i(t,p), \ i = 1, .., k\}$ eigenvalues near 1, including the eigenvalue $\lambda^t_1(p) = 1$.
In the following, we will numerically investigate the pitchfork bifurcation of the underlying system. Thus, we will mainly focus on the changes of the eigenvalues
$\{\lambda^\epsilon_i(t,p), \ i = 1, .., k\}$ and their corresponding eigenvalues $\{\phi'^\epsilon_i, \ i = 1, ..., k\}$, as the pa-

rameter p is varied.

The flow map is approximated by using a fourth order Runge Kutta ODE solver with a time interval of length 1 and step size of $h = 0.1$, i.e 100 time steps. The domain $[-2, 2] \times [-2, 2]$ is subdivided into 2^{depth} rectangular grid sets (boxes). Here, we use $depth = 13$, which gives $N = 2^{13} = 8192$ boxes B_i that partition the phase space M. In each box, we sample 900 test points as initial data for constructing the transition matrix approximation of P_ϵ^t. Note that diffusion of amplitude ϵ is artificially including from the numerical discretization. That is, the diffusion amplitude ϵ is equal to the size of the subdomains which are all equal.

Note that the system (4.44) is open. That is trajectories from initial test points may leave the domain $D = [-2, 2] \times [-2, 2]$ during integration. To numerically overcome this computational obstacle, an additional box is added in order to capture all the image points that are being mapped out of the initial domain D when computing the transition matrix. At the end of the computation, this temporary subdomain will be removed from the eigenvector entries by just considering the 2^{13} first entries.

For $p = 1$, we show the eigenvalues of the transition matrix approximation of P_ϵ^t in figure 4.12. The real eigenvalues are isolated and accumulated near 1. Their corresponding

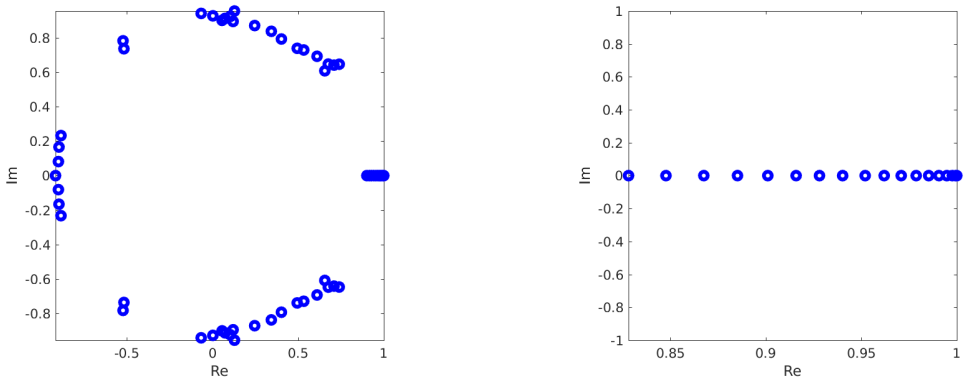

Figure 4.12: Largest magnitude eigenvalue for the Duffing-type system (4.44) for parameter $p = -1$ (left) and largest real eigenvalues (right).

eigenvectors are shown in figure 4.13, where we only visualize the four largest. These are rings of almost-invariant sets which depict the stationary behavior of the system. Note the center pattern defined in (4.19). The latter carries the center fixed point $(0, 0)$. The set-oriented bifurcation will be investigated by focusing on the changes of both real eigenvalues and eigenvectors shown, respectively, in figure 4.12 and figure 4.13.

To study the spectral signature of the pitchfork bifurcation shown in figure 4.11, we vary p in the interval $[-0.5, 0.5]$, first. Then we track the changes of the real eigenvalues and

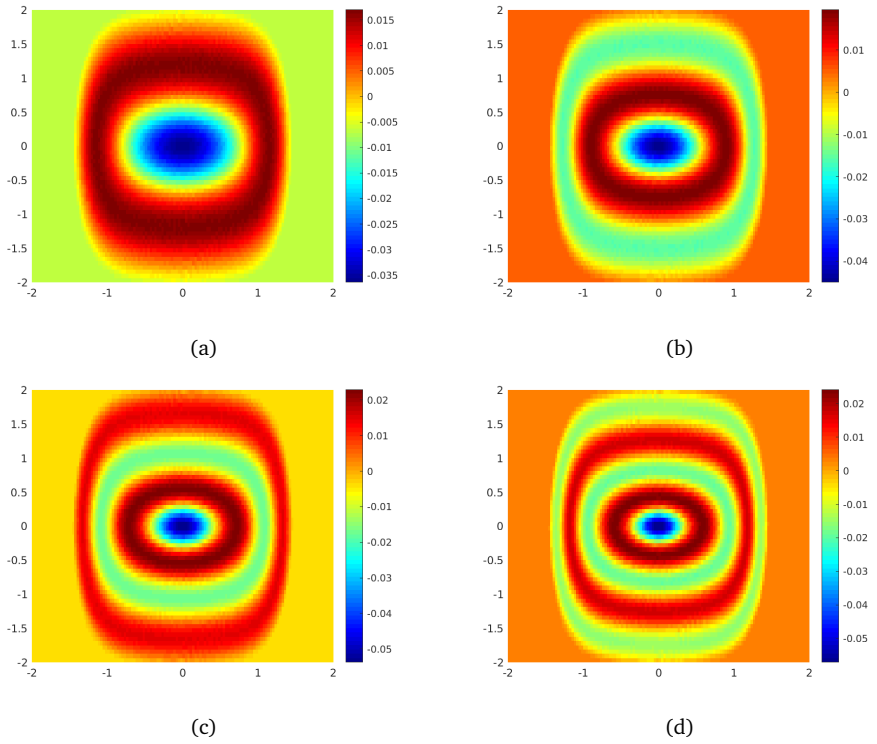

(a) (b)

(c) (d)

Figure 4.13: Four largest real eigenvectors for the Duffing-type system (4.44) for parameter $p = -1$.

their corresponding eigenvectors for different parameters p.

In figure 4.14, the trends of the nine largest real eigenvalues are shown for $p \in [-0.5, 0.5]$. Each panel corresponds to the changes over p of three different eigenvalues. For instance, left panel (figure 4.14(a)) shows the trends of $\{\lambda_1^\epsilon(t,p), \lambda_2^\epsilon(t,p), \lambda_3^\epsilon(t,p)\}$, middle panel (figure 4.14(b)) yields $\{\lambda_4^\epsilon(t,p), \lambda_5^\epsilon(t,p), \lambda_6^\epsilon(t,p)\}$. Finally, in the right panel (figure 4.14(c)), we illustrate the changes of $\{\lambda_7^\epsilon(t,p), \lambda_8^\epsilon(t,p), \lambda_9^\epsilon(t,p)\}$.

Looking at figure 4.14(a)-(c), a particularly common shape seems to repeatedly show up. Indeed, a peek of the eigenvalues trend $\lambda_j^\epsilon(t,p),\ j = 1, 2, ..., 9$ at the critical parameter $p = 0$ can be seen as we slide from one panel to another. This peek becomes sharper as we go down to smaller magnitude eigenvalues. To better visualize this particular slope, we plot the zoomed version of figure (4.14) for $p \in [-0.05, 0.05]$. The corresponding zoomed picture is shown in figure (4.15).

The spectral signature of the pitchfork bifurcation of the system (4.44) is illustrated in Figure 4.14. The spectral outcome of the critical slowing down is visible when p is close to 0. Indeed, one can see that when p enters what we call a critical interval as

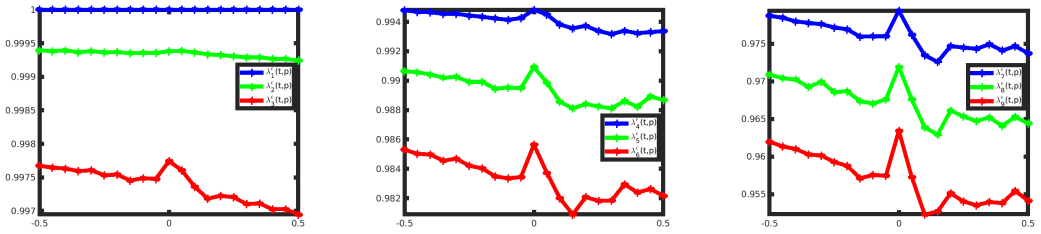

(a) (b) (c)

Figure 4.14: Nine largest real eigenvalues for the Duffing-type system (4.44), for parameter $p \in [-0.5, 0.5]$ in the x-axis and $\lambda_j^\epsilon(t,p)$, $j = 1, 2, ..., 9$ in the y-axis. (a):$\{\lambda_1^\epsilon(t,p), \lambda_2^\epsilon(t,p), \lambda_3^\epsilon(t,p)\}$, (b):$\{\lambda_4^\epsilon(t,p), \lambda_5^\epsilon(t,p), \lambda_6^\epsilon(t,p)\}$, (c):$\{\lambda_7^\epsilon(t,p), \lambda_8^\epsilon(t,p), \lambda_9^\epsilon(t,p)\}$.

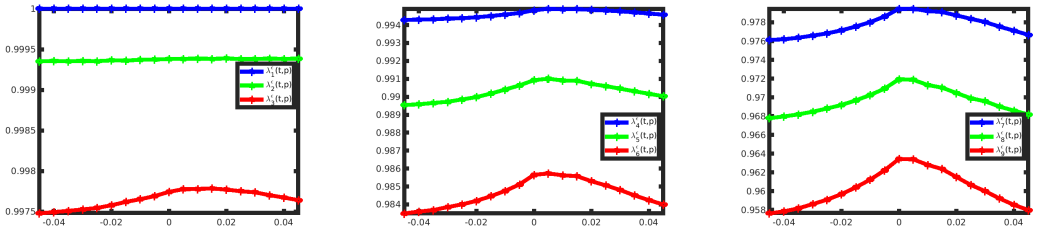

(a) (b) (c)

Figure 4.15: Nine largest real eigenvalues for the Duffing-type system (4.44), for parameter $p \in [-0.05, 0.05]$ in the x-axis and $\lambda_j^\epsilon(t,p)$, $j = 1, 2, ..., 9$ in the y-axis. (a):$\{\lambda_1^\epsilon(t,p), \lambda_2^\epsilon(t,p), \lambda_3^\epsilon(t,p)\}$, (b):$\{\lambda_4^\epsilon(t,p), \lambda_5^\epsilon(t,p), \lambda_6^\epsilon(t,p)\}$, (c):$\{\lambda_7^\epsilon(t,p), \lambda_8^\epsilon(t,p), \lambda_9^\epsilon(t,p)\}$.

shown in Figure 4.15, eigenvalues start increasing continuously towards 1. This is fairly comparable to the deterministic version of criticality in (4.47) where all leading real parts eigenvalues of P^t converge to 1 as p approaches 0. Note also that in Figure 4.14 and more clearly in figure 4.15, the further the eigenvalue is away from 1, the earlier its increasing process starts. The explanation to that is twofold. First, each eigenvalue measures how porous are the different almost-invariant sets generated by its corresponding eigenvector. Based on this fact, the set-oriented dynamics measures transport between different almost-invariant sets. Note that the external perturbation is responsible for the transport between almost-invariant sets. Second, the almost-invariant sets appear, in this context, as ring shapes surrounding a central almost invariant pattern supported on $(0, 0)$ (see panels (a),(b),(c) and (d) in Figure 4.13 as an example). Therefore, the further an eigenvalue is away from 1, the stronger is the transport between ring patterns. Thus, they are more porous, under external perturbations. This implies that the undergoing dynamics of the system (4.44) is better captured by the smaller eigenvalues. Hence,

when the dynamics of the latter system slows down, transport between rings decreases as well. This results in an increase of the corresponding eigenvalues towards 1, which explains the critical slowing down before the bifurcation. As a consequence, if one only tracks the second leading eigenvalue, one may not see a spectral signature when the parameter crosses its critical value. This is due to the fact that second leading eigenvalue is already pretty close to 1 and cannot be 1 because, due to the underlying dynamics and the stochastic perturbation applied, the transition matrix is irreducible. The continuous growth of eigenvalues, which are further away from 1, is better visualized in Figure 4.14(b)-(c). The latter is a zoomed out version of Figure 4.15(b)-(c).
In figure 4.16, we plot the changes of the eigenvectors corresponding to eigenvalues in figure 4.14. Without missing any qualitative detail in the analysis, we only chose the eigenvectors corresponding to eigenvalues $\lambda_2^\epsilon(t,p)$ and $\lambda_9^\epsilon(t,p)$ and visualize them before, at, and after the bifurcation. That is, for parameter values $p=-0.5$, $p=0$, and $p=0.15$.
Figure 4.16 shows that the ninth eigenvector corresponding to the eigenvalue $\lambda_9^\epsilon(t,p)$ (see figure 4.16(b),(d),(f)) has more ring-like patterns that are also finer than the ring-like patterns displayed by the second eigenvector $\lambda_2^\epsilon(t,p)$ (see figure 4.16(a),(c),(e)). Therefore, under external perturbations, the transport between rings is stronger in figure 4.16(b),(d),(f) than in figure 4.16(a),(c),(e). This explains why smaller magnitude eigenvalues are more sensitive to changes of parameter p near the bifurcation point. However, a bifurcation of almost-invariant sets in the sense of pattern splitting is not clear with this approach. Indeed, after the bifurcation at $p=0.14$, the second eigenvector does not show any split-like shape (see 4.16(e)). A pattern split can only be seen in the ninth eigenvector pattern (see 4.16(f)) similar to figure 4.11(right), and this is explained by the fact that the eigenvector sign pattern partitions the phase space into finer almost-invariant sets. Thus, the partition element supported in the neighborhood of the fixed point $(0,0)$, say the particular invariant set defined in (4.19), will capture the local qualitative change following the bifurcation.

4.6.2 Infinitesimal generator approach

In this section, we want to confirm the spectral signature of the pitchfork bifurcation of (4.44) from the spectrum of a randomly perturbed infinitesimal generator. The latter can thus be understood as the perturbed version of the generator defined earlier in (4.4). Recall that with the latter operator we could investigate the spectral signature of the bifurcation that occurred in system (4.12) in example 10 with the deterministic infinitesimal operator. The approach was based on the trace formula (4.10)-(4.11) which

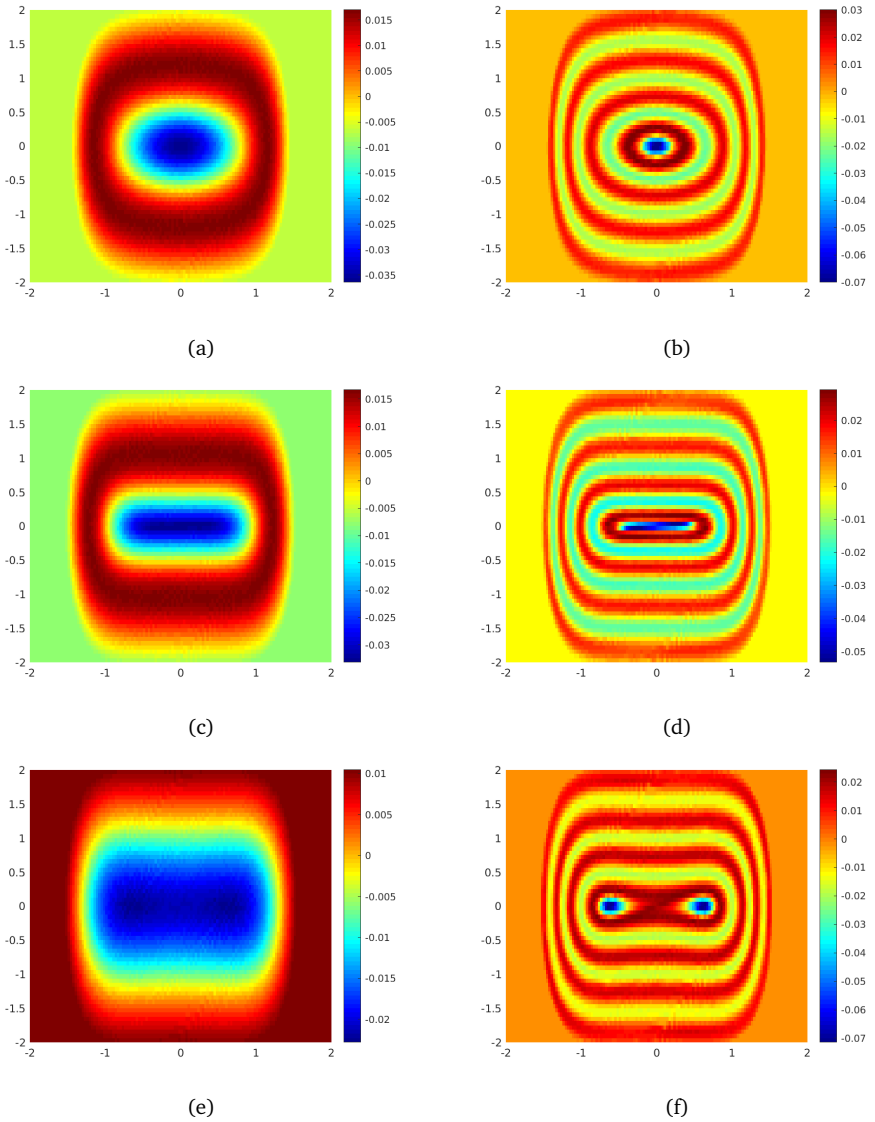

Figure 4.16: Changes of almost-invariant patterns for $p \in [-0.5, 0.5]$. Eigenvector of $\lambda_2^\epsilon(t,p)$ (a)(left) and eigenvector $\lambda_9^\epsilon(t,p)$ (b)(right) for $p = -0.5$. Eigenvector of $\lambda_2^\epsilon(t,p)$ (c)(left) and eigenvector $\lambda_9^\epsilon(t,p)$ (d)(right) for $p = 0$. Eigenvector of $\lambda_2^\epsilon(t,p)$ (e)(left) and eigenvector $\lambda_9^\epsilon(t,p)$ (f)(right) for $p = 0.14$.

is a method that requires existence of hyperbolic stationary fixed points. Hence, changes of the discrete spectrum of (4.4) which is computed via the trace formula applied to system (4.12) are shown in figure 4.3. Moreover, the Spectral Mapping Theorem (4.6) can be used to have the changes of the eigenvalues of the deterministic Frobenius-Perron operator P^t defined in (4.3) as shown in figure 4.4 .

However, in this set-oriented case study, we are using perturbed transfer operators P_ϵ^t which yield real eigenvectors generating almost-invariant sets (see figure 4.13 and figure

4.16) and corresponding eigenvalues that yield signatures of the qualitative change of (4.44) (see figure 4.14 and figure 4.15).
Adding external perturbations to a deterministic systems such as (4.44) is usually done to respond to the undergoing physical realities of the phenomena that are being modeled. Indeed, external perturbations are present in many real world situations. Besides, it may be difficult to have a complete knowledge of those perturbations. Therefore a deterministic model might be inappropriate to model those physical system. One should rather consider the perturbations by adding external relatively small random perturbations into the mathematical model being used. As a matter of fact, two types of random perturbations may be used depending on the question being addressed. For, instance, consider the system defined in (4.1). A discontinuous random perturbation consists of adding random noise at initial data before applying the flow map (4.2) and adding random noise at image data after applying the flow map (4.2). This leads to the transfer operator P_ϵ^t, which is compact and suitable for numerical approximations. The discontinuous perturbation of this kind does not only yield a compact operator but it is also a way of formulating mathematically robust almost-invariant sets which are more suitable for real life modeling of invariant patters such as ocean vortices.
A continuous random perturbation, however, considers a random (ODE) built from the deterministic (ODE) (4.1). That is, we deduce a stochastic differential equation (SDE)

$$\dot{x} = F(x,p) + \epsilon \frac{dW_t}{dt}, \tag{4.49}$$

from (4.1). The noise amplitude ϵ is positive and W is the Wiener process. In this work, we will not go through SDE analysis, as it is indeed not in the spectrum of our research study. For more details about this approach, see [49], Chapter 10.
In the following, we briefly define the perturbed generator and its numerical approximation before exploring its spectrum for different parameters p.
The solutions of (4.49) are continuous time Markov processes (diffusion processes) $X_t,\ t \geq 0$ with density $f(t,x)$ satisfying

$$\mathbb{P}(X_t \in C) = \int_C f(t,x)dx.$$

However, this density can be found without any explicit knowledge concerning the process X_t. Indeed, the density $f(t,x)$ appears as a solution of the Fokker Planck equation

$$\frac{\partial f}{\partial t} = \frac{\epsilon^2}{2}\Delta f - \nabla \cdot (Ff) =: \mathcal{G}_\epsilon f. \tag{4.50}$$

As a consequence, with initial condition at initial time t_0, i.e. initial density function $f(t_0, x) = f(x)$, the Partial differential equation (4.50) has a solution

$$f(t, x) = \int_X \Gamma(t, x, y) f(y) dy \tag{4.51}$$

and for every $g \in L^2(D, \Sigma, \mu)$, (4.51) is called the generalized solution of (4.50) ([49], Chapter 11).
Having the fundamental solution Γ, we define a family of transfer operators $\left\{\mathcal{P}_\epsilon^t\right\}$ such that for a given initial density $f(t_0, x) = f(x)$, we have

$$\mathcal{P}_\epsilon^0 f(x) = f, \quad \mathcal{P}_\epsilon^t f(x) = \int_X \Gamma(t, x, y) f(y) dy. \tag{4.52}$$

The family of operators $\left\{\mathcal{P}_\epsilon^t\right\}$ forms a semigroup of transfer operators referred to as stochastic semigroups (see [49], Chapter 11). Moreover, $\mathcal{G}_\epsilon$ is the infinitesimal generator of the transfer operator $\left\{\mathcal{P}_\epsilon^t\right\}$, with Neumann boundary conditions [32].
Our main interest is the discrete spectrum of $\mathcal{G}_\epsilon$ and almost-invariant sets; mainly changes of these eigenvalues with respect to p. The framework of finding almost invariant sets from the spectrum of the operator $\mathcal{G}_\epsilon$ was widely developed in [33], both analytically and numerically. Indeed, in [33] it is shown that a μ-measurable set A is almost-invariant if

$$r_\epsilon(A) := \frac{\mathbb{P}\left(X_0 \in A, X_t \in A\right)}{\mathbb{P}\left(X_0 \in A\right)} \approx 1,$$

for modest times t with X_0 and X_t denote initial and final random variables solutions of the SDE (4.49). This can be characterized by using the generator $\mathcal{G}_\epsilon$. Indeed, we define the functional $\mathcal{G}_{\epsilon,A} \colon \mathcal{D}\left(\mathcal{G}_\epsilon\right) \mapsto \mathbb{R}$ by

$$\mathcal{G}_{\epsilon,A} f := \lim_{t \to 0} \int_A \frac{\mathcal{P}_\epsilon^t f - f}{t} d\mu \;\; f \in \mathcal{D}\left(\mathcal{G}_\epsilon\right), \tag{4.53}$$

where $\mathcal{D}\left(\mathcal{G}_\epsilon\right)$ is the linear subspace of $L^2(D, \Sigma, \mu)$ where the above limit exists. Let $f_A = f\chi_A / \left(\int f \chi_A\right)$ with the density $f \in \mathcal{D}\left(\mathcal{G}_\epsilon\right)$. Then for a μ-measurable set A and $t \to 0$, it is proven in [33] that

$$r_\epsilon(A) = 1 + \mathcal{G}_{\epsilon,A} f_A + o(t).$$

As a consequence, a μ-measurable A is almost-invariant if

$$\mathcal{G}_{\epsilon,A} f_A \approx 0.$$

The connection between almost-invariant set and spectrum of $\mathcal{G}_\epsilon$ is established in the following way.
If $\mathcal{G}_\epsilon$ has a real eigenvalue $\lambda < 0$ with corresponding eigenfunction f, then $\int f = 0$. Moreover, if $A^+ = \{f \geq 0\}\,,\ A^- = \{f < 0\}$. Then

$$\mathcal{G}_{\epsilon,A^+}|f_{A^+}| + \mathcal{G}_{\epsilon,A^-}|f_{A^-}| = \lambda.$$

Hence the above equality yields $\mathcal{G}_{\epsilon,A^\pm}|f_{A^\pm}| \approx 0$ for ≈ 0, which means that A^+ and A^- will be almost-invariant sets generated by the eigenvector f. Hence, this sets a connection between almost invariant sets and the spectrum $\mathcal{G}_\epsilon$. For spectral signatures of bifurcation, we will focus on real eigenvalues of $\mathcal{G}_\epsilon$ which are close to 0 and their corresponding eigenfunctions.
The finite dimensional approximation of $\mathcal{G}_\epsilon$ was provided in [33]. It is mainly based on the discretization of phase space into boxes but, unlike (4.35), a trajectory computation is not needed. That is actually a huge advantage of using the infinitesimal generator. In fact, only the knowledge of the vector field is enough to approximate $\mathcal{G}_\epsilon$. Once the phase space is discretized into boxes, the velocity field is considered and inflow/outflow rates between boxes are computed to yield the matrix approximation of $\mathcal{G}_\epsilon$. Note also that, an explicit noise amplitude ϵ is required for the numerical computations.
We thus, directly compute the spectrum of finite dimensional approximation of $\mathcal{G}_\epsilon$ proposed in [33]. We will then analyze the spectral signature of the bifurcation of (4.44). The phase space $[-2, 2] \times [-2, 2]$ is discretized in 200×200 boxes B_i of equal size. We use a noise amplitude $\epsilon = 10^{-5}$. In figure, we show the 60 smallest magnitudes eigenvalues of $\mathcal{G}_\epsilon$ as the bifurcation parameter p changes in $[-0.5, 0.5]$. Near $\overline{p} = 0$, the real parts eigenvalues tend to accumulate to 0 similar to the imaginary parts converge to 0 as well. Real eigenvalues trends in figure 4.17 is similar are similar to eigenvalues trend in figure 4.3. Hence, despite the random perturbation added to the dynamics, the spectral signatures for pitchfork bifurcation persist and, in the eigenvalues level, the set-oriented approach does not violate this spectral characterization of the pitchfork bifurcation. Moreover, the spectrum shown in figure 4.17 has strictly real eigenvalues. Indeed, in figure 4.18 the six smallest magnitudes eigenvalues are shown. These eigenvalues are real as the imaginary parts are all zero. The signatures of the real eigenvalues as p changes is the same the eigenvalues trends of the diffused transfer operator shown in figure 4.14 and figure 4.15. Therefore, the spectral signature of the pitchfork bifurcation of system 4.44 is robust under discontinuous additive noise and continuous additive noise. In figure 4.19 we show the changes of the second and third eigenvectors for $p = -0.5$, $p = 0$ and $p = 0.5$. With

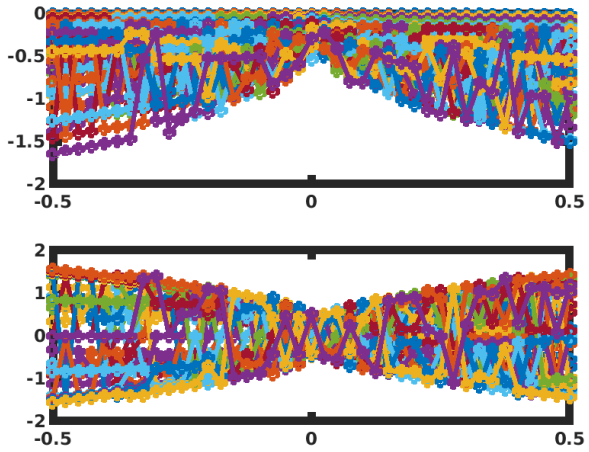

Figure 4.17: Numerically approximated 60 smallest magnitudes complex eigenvalues of $\mathcal{G}_\epsilon$ for $p \in [-0.5, 0.5]$. Real parts eigenvalues (Top), imaginary parts eigenvalues (Bottom).

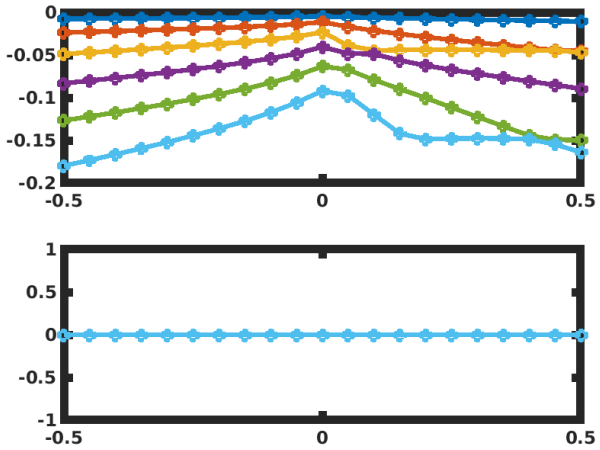

Figure 4.18: Numerically approximated 6 smallest magnitudes eigenvalues of $\mathcal{G}_\epsilon$ for $p \in [-0.5, 0.5]$. Real parts eigenvalues (Top), imaginary parts eigenvalues (Bottom).

the continuous noise added to the dynamics, the spectrum of the infinitesimal generator exhibit real eigenvectors patterns for $p \in [-0.5, 0.5]$ in figure 4.19, which are similar to the real eigenvectors patterns of P_ϵ^t shown in figure 4.16.

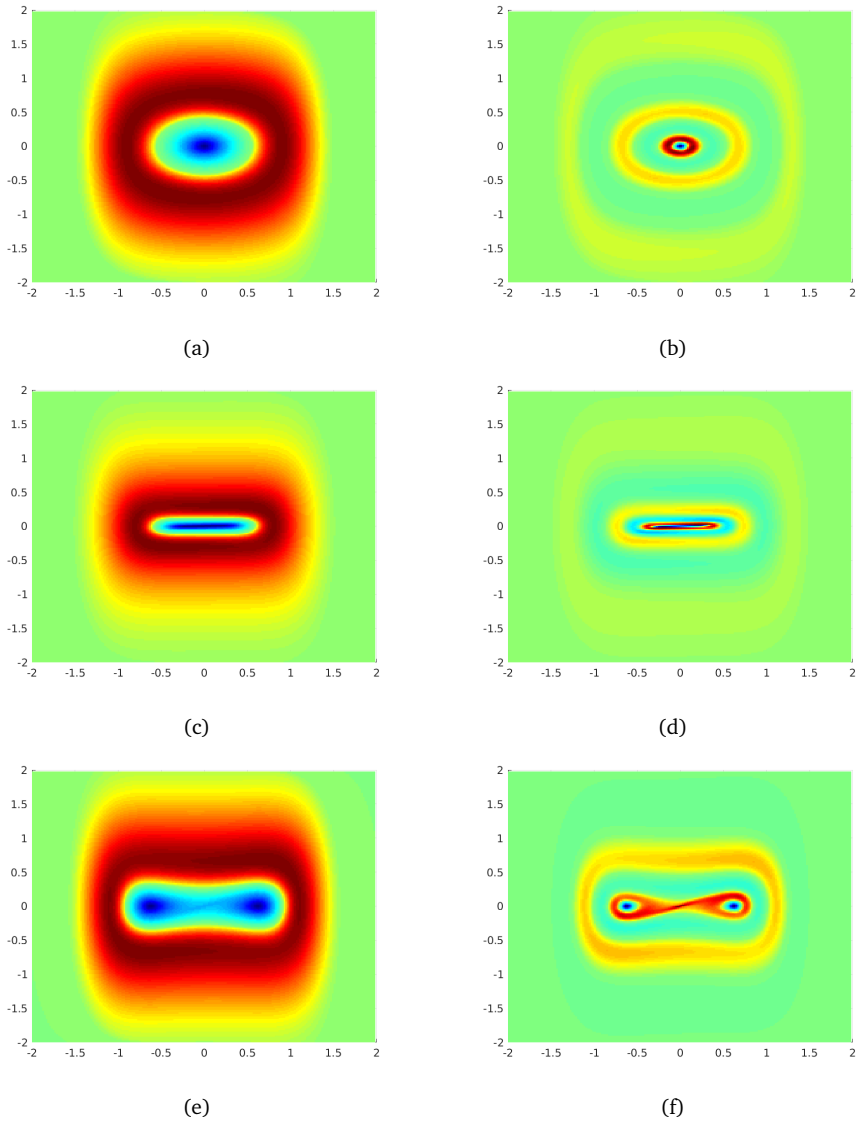

Figure 4.19: Changes of almost-invariant patterns for $p \in [-0.5, 0.5]$. (a) eigenvector of $\lambda_2^\epsilon(t,p)$, (b) eigenvector $\lambda_6^\epsilon(t,p)$ for $p = -0.5$. (c) eigenvector of $\lambda_2^\epsilon(t,p)$, (d) eigenvector $\lambda_6^\epsilon(t,p)$ for $p = 0$. (e) eigenvector of $\lambda_2^\epsilon(t,p)$, (f) eigenvector $\lambda_6^\epsilon(t,p)$ for $p = 0.14$.

4.7 Summary

This chapter discusses transfer-operator based ideas to characterize spectral signatures of bifurcations of an autonomous dynamical system by using changes of almost-invariant patterns. We have restricted our study to a special class of systems such as (4.44). The reason for this choice is justified by our findings in real world systems. Indeed, we want to predict the sudden change of Antarctic vortex break up in September 2002, from

satellite velocity data, see figure 1.1.

Our approach is inspired by results in [17, 48] where a statistical analysis of a deterministic dynamical system was used to characterize bifurcations. In [17], the pitchfork bifurcation was studied and spectrally characterized from the discrete spectrum of the infinitesimal generator (4.4). In this work we also consider the statistical evolution of the underlying dynamical system but we focused on macroscopic almost-invariant measurable sets. Thus, in practice, our approach is different from [17]. Indeed, while in [17] the discrete spectrum is used altogether to observe changes as the bifurcation parameter is varied, in our work we use a perturbed transfer operator and select a subset of its discrete spectrum which approximates almost-invariant sets. That is, we are only interested in changes of a part of the discrete spectrum (eigenvalues, eigenfunctions) since the latter yield dominant patterns which are supported on the critical point. Moreover, this part of the spectrum is composed only of real eigenvalues and real eigenfunctions which exhibit sign patterns that can be used to extract robust almost-invariant sets. In order to characterize the qualitative changes of the latter, we track the changes of the corresponding real eigenvalues as we vary the bifurcation parameter p. Our findings were very interesting as near the critical parameter (i.e. $\overline{p} = 0$), we see particular trends of the eigenvalues which truly characterize the transport dynamics occurring between almost-invariant sets. Moreover, these spectral changes agree with the ones in [17].

Most importantly, our findings help us understand how we should specifically define the notion of bifurcation of almost-invariant sets. Indeed, near the critical parameter we have evidence of a bifurcation from observing the changes of the eigenvalues as shown by figure 4.14 and figure 4.15. However, the corresponding eigenvectors in figure 4.16(b)-(d), for instance, do not show any qualitative change near $\overline{p}$. Looking at figure 4.16(e), we only become aware of changes of patterns when p is far from its critical value after the bifurcation. Therefore, the local pitchfork bifurcation as shown by figure 4.11 is not characterized by dominant patterns, even if it is characterized by the corresponding eigenvalues.

Hence, we state that a bifurcation of almost-invariant set must be simultaneously characterized by both eigenvectors and corresponding eigenvalues. The next chapter will bring more details to proving our statement.

5 Predicting set-oriented bifurcation of almost-invariant patterns

From chapter 4, it is clear that a spectral characterization of bifurcations of almost-invariant sets should simultaneously concern dominant real eigenvalues and corresponding eigenvectors. Moreover, the discrete approximation of a diffused transfer operator is a stochastic matrix whose real leading eigenvectors exhibit sign patterns which approximate almost invariant sets. The corresponding eigenvalues showed very well signatures of the pitchfork bifurcation but the eigenvectors did not. Hence, in this study, we are going to develop a bifurcation theory of almost-invariant sets, which will be strictly based on the qualitative changes of the almost-invariant patterns, instead of the critical value of the bifurcation parameter. Indeed, the latter approach makes sense, since the pitchfork bifurcation is a point bifurcation, while we are interested in the changes of macroscopic sets.

The aim of the chapter is to provide further methodological steps towards a better understanding of such global bifurcations. The approach is based on a purely discretized dynamical systems where the evolution of the flows yield stochastic matrices.

In this chapter, we are going to we rigorously study two explicit dynamical models, a Duffing-type oscillator and a single gyre flow, and identify early warning signals for splittings of patterns through the trends of eigenvalues with respect to a bifurcation parameter. The results of this chapter have been submitted for publication in the SIAM Journal for Applied Dynamical Systems [57].

5.1 Set-oriented approach and almost-invariant patterns

In this chapter, we follow similar dynamical settings as chapter 4. Indeed, we consider a p-parametrized ODE as described in (4.1) and the flow map (4.2) which is denoted here

by ϕ^t and defined in the same measure space (D, Σ, μ). In addition, (4.1) is supposed to model the evolution of a rotating incompressible steady fluid flow such as a vortex, throughout the present chapter. The Lebesgue measure μ is, thus, invariant.

5.1.1 Finite number of almost-invariant sets

Following [21], the *invariance ratio* of a measurable set A_i, $i = 1, 2, \ldots, k$ is defined as

$$\rho_\mu(A_i) = \frac{\mu(A_i \cap \phi^{-t}(A_i))}{\mu(A_i)}. \tag{5.1}$$

This is interpreted as the probability of a point in A_i to stay in A_i under the mapping ϕ^t . Hence, any measurable invariant set A satisfies $\rho_\mu(A) = 1$. As defined in chapter 2 and analytically constructed in chapter 3, $\{A_1, A_2, \ldots, A_k\}$ is a family of almost-invariant sets that partitions the phase space D if $D = \cup_{i=1}^{k} A_i$ and

$$\rho_\mu(A_i) \approx 1 \ \ \forall \ i = 1, 2, \ldots, k. \tag{5.2}$$

Finding such a family of almost-invariant sets is intractable in practice. Instead one seeks optimal solutions of a relaxed problem based on the description of the dynamics in terms of a finite-state Markov chain and its spectral properties.

5.1.2 Discretization and stochastic matrices

The time evolution of the dynamical system on the discretized phase space yields the transition matrix

$$(P_N^t)_{ij} = \frac{m(B_i \cap \phi^{-t}(B_j))}{m(B_i)}, \tag{5.3}$$

which is already established in chapter 4. Recall that P_N^t is actually a finite rank approximation of the Perron-Frobenius operator [22], each (i, j)-th entry is the probability that a randomly selected point $x \in B_i$ has its image in B_j, and P_N^t is a row stochastic matrix and is interpreted as the transition matrix associated with an N-state Markov chain over the finite states $\left\{B_i\right\}_{i=1}^{N}$. Let us define the lumped finite state [21]

$$\mathcal{C}_N = \left\{ \ A \subset D \ : \ A = \bigcup_{j \in \mathcal{I}} B_j, \ \mathcal{I} \subset \{1, 2, \ldots, N\} \right\}.$$

The Markov chain (5.3) is not in general reversible. However, reversible transition matrices yield important spectral properties which are dynamically efficient in terms of checking how mass is transported in both forward and backward time. Moreover, as we are ultimately interested in the macroscopic dynamics of patterns such as the transport and critical transition of optimal almost-invariant patterns, it is more relevant to use a reversibilised Markov chain. The latter comes as straightforward transformation of (5.3) as

$$Q = \frac{(L+P)}{2}, \tag{5.4}$$

where $L = \left(\frac{\pi_j P_{ji}}{\pi_i}\right)_{i,j=1}^{N}$ is the transition matrix of the reversed Markov chain and $P := P_N^t$ is assumed to have a unique positive stationary distribution $\pi = [\pi_1, \pi_2, \ldots, \pi_N]$ with $\pi P = \pi$; in our case it holds that $\pi_i = m(B_i)$ with m being normalized Lebesgue measure. Note that Q is exactly the approximation of the operator Q_ϵ in chapter 3 with $\epsilon = 0$. It follows the approximation of the invariance ratio as follows

$$\begin{aligned} \rho_\mu^N(A) &= \frac{\sum_{i,j\in\mathcal{I}} \pi_i (Q_N^t)_{ij}}{\sum_{i\in\mathcal{I}} \pi_i},\ \mathcal{I} \subset \{1,2,\ldots,N\},\ \text{ invariance ratio,} \\ &= 1 \ \text{ if } \ A \ \text{ is invariant,} \\ &\approx 1 \ \text{ if } \ A \ \text{ is almost-invariant.} \end{aligned} \tag{5.5}$$

Q is a transition matrix as the weighted average of two transition matrices P and L. Moreover, Q is reversible since it satisfies the so-called detailed balance condition, $\pi_j Q_{ji} = \pi_i Q_{ij}$. Further important properties of Q include:

1. Q is diagonalized by a basis of π-orthogonal right eigenvectors.
2. Q has only real eigenvalues contained in $[-1,\ 1]$. Moreover, for any given eigenvalue with a corresponding right eigenvector x, there is an associated left eigenvector y such that $y = \mathcal{D}_N x$, where $\mathcal{D}_N = \text{diag}([\pi_1, \pi_2, \ldots, \pi_N])$.
3. Q is symmetric or self-adjoint with respect to the weighted Euclidean space $\langle\cdot,\cdot\rangle_\pi$ defined in $\mathbb{R}^N$ such that $\langle x, y\rangle_\pi = \sum_{i=1}^N x_i y_i \pi_i$, and two vectors x, y are orthogonal if $\langle x, y\rangle_\pi = 0$.

Moreover, it is easy to verify that the adjoint of L with respect to $\langle\cdot,\cdot\rangle_\pi$ is the transition matrix P. Therefore, Q is just the average of two adjoint matrices. Besides, in terms of

transport, Q is checking how mass is transported in forward and backward at stationarity. For more details on Markov chains we refer to e.g. [23]. In this work, we will use the reversibilized transition matrix to almost-invariant patterns and their bifurcations.

5.2 Perturbed invariant patterns and spectral configurations

In this section, we consider a k-state, $k > 2$, reducible Markov chain which becomes irreducible when it is subjected to small perturbations. Then we assume the existence of disjoint strongly connected lumped states $\{A_i\}_{i=1}^k$ and their perturbed versions $\{A_i(\epsilon)\}_{i=1}^k$, $\epsilon \in \mathbb{R}$. Thus, under some convenient reordering within the states, the unperturbed and perturbed Markov chains are respectively given by

$$Q = \begin{pmatrix} Q_1 & 0 & \cdots & 0 \\ 0 & Q_2 & \cdots & 0 \\ \vdots & \vdots & \ddots & \vdots \\ 0 & 0 & \cdots & Q_k \end{pmatrix}, Q(\epsilon) = \begin{pmatrix} Q_1(\epsilon) & E_{12} & \cdots & E_{1k} \\ E_{21} & Q_2(\epsilon) & \cdots & E_{2k} \\ \vdots & \vdots & \ddots & \vdots \\ E_{k1} & E_{k2} & \cdots & Q_k(\epsilon) \end{pmatrix}, k > 2. \quad (5.6)$$

Every Q_i, $i = 1, \ldots, k$, is a primitive $n_i \times n_i$ reversible transition matrix over the "cloud" of states A_i. Moreover, due to the reducibility of Q, a system described by Q will always stay in state A_i once it is initialized in A_i. This means that the conditional transition probability to map to A_j when in A_i, $w(A_j, A_i) = \frac{\sum_{i\in I, j\in J} \pi_i Q_{ij}}{\sum_{i\in I} \pi_i}$, is the Kronecker symbol δ_{ij}, $j = 1, \ldots, k$, . Besides, the matrix Q has an eigenvalue 1 of multiplicity k. One may think of the matrix Q as the reversibilized of version (5.3) generated from (**??**).

The transition matrices $Q(\epsilon)$, $\epsilon \in \mathbb{R}$ are, however, irreducible and the magnitude of the off-diagonal blocks E_{ij} is very small relative to 1 with respect to any chosen matrix norm. This implies, $w(A_j(\epsilon), A_i(\epsilon)) \approx \delta_{ij}$, $i, j = 1, \ldots, k$, and means that when the dynamical system enters A_i, it will stay in A_i for a long time with high probability before it leaves. The patterns $A_i(\epsilon)$ are referred to as almost-invariant patterns. Following the settings in [24], $Q(\epsilon)$ is considered as an operator-valued function of ϵ, which is analytic in $E \subset \mathbb{R}$, $0 \in E$. Thus it can be, in general, expressed as $Q(\epsilon) = Q(0) + \epsilon Q^{(1)}$, which is the first order Taylor expansion of $Q(\epsilon)$. As a consequence of this regularity condition, the eigenvalues of $Q(\epsilon)$ are continuous in ϵ. From this continuity and the fact that the $Q_i(\epsilon)$ are nearly stochastic matrices [34], we have that the spectrum of $Q(\epsilon)$ includes three parts:

(a) the Perron root $\lambda_1(\epsilon) = 1$,

(b) the set of $k-1$ non-unit eigenvalues, $\{\lambda_2(\epsilon), \ldots, \lambda_k(\epsilon)\}$ that are clustered near 1.

(c) the remaining part of the spectrum which is bounded away from 1, for small ϵ.

Throughout this work, we set the ordering $1 = \lambda_1(\epsilon) > \lambda_2(\epsilon) \geq \ldots \geq \lambda_k(\epsilon)$. Note that this section is motivated by the fact that the class of models we consider in this study yield invariant sets in their dynamical evolutions. This means that the almost-invariant patterns will be just considered as perturbed invariant sets.

Example 17 *To illustrate this setting, we consider a* 60*-state Markov chain with* $\mathcal{S} = \{1, 2, \ldots, 60\}$*. This is chosen to be reducible with three disjoint invariant patterns* $A_1 = \{1, 2, \ldots, 10\}$*,* $A_2 = \{11, 12, \ldots, 40\}$ *and* $A_3 = \{41, 42, \ldots, 60\}$*. The corresponding transition matrix is shown in figure 5.1 (left) with the blue dots highlighting the nonzero entries. An example of a perturbed Markov chain, allowing for small amounts of transport between the three patterns, is shown in figure 5.1 (right), as the corresponding irreducible transition matrix* $Q(\epsilon)$*. The corresponding eigenvalues of both matrices are shown in figure 5.2. As*

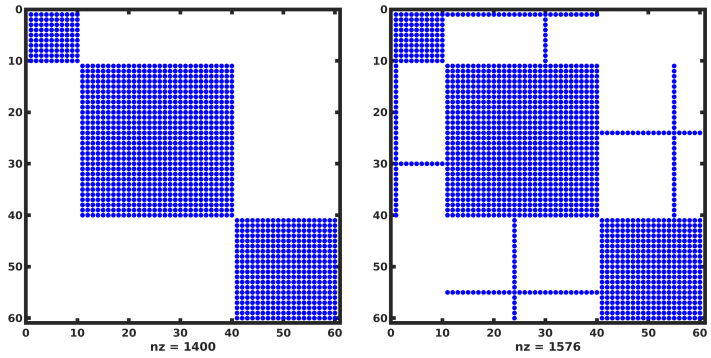

Figure 5.1: Reducible and irreducible transition matrices Q (left) and $Q(\epsilon)$ (right) of a 60-state Markov chain (example 17) exhibiting three invariant or three almost-invariant patterns, respectively.

expected, the unperturbed matrix has an eigenvalue 1 *of multiplicity* 3 *(figure 5.2 (left)), while the perturbed matrix has two eigenvalues near the Perron root (figure 5.2 (right)).*

Due to reducibility, the global stationary distribution of the unperturbed transition matrix Q in (5.6) is not unique. Indeed, each vector V_i, where

$$V_i = (0, \ldots, 0, \pi^{(i)}, 0, \ldots, 0), \;\; i = 1, \ldots, k, \;\; \text{with } \pi^{(i)} Q_i = \pi^{(i)}, \tag{5.7}$$

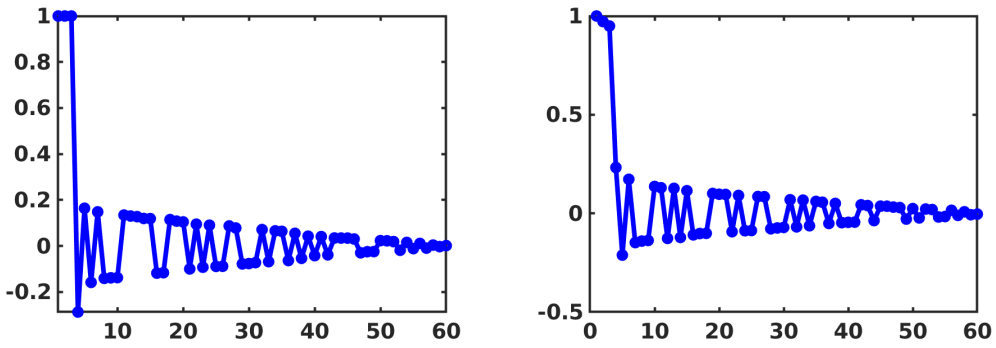

Figure 5.2: Eigenvalues (ordered by magnitude) of the unperturbed matrix Q (left) and the perturbed matrix $Q(\epsilon)$ (right) for the 60-state Markov chain model in example 17. The perturbation results in two eigenvalues very close to one (right, see also inlet) which originate from the three-fold eigenvalue 1 (left) in the unperturbed situation.

is a left eigenvector of Q corresponding to the k-fold eigenvalue $\lambda_1 = 1$ of (5.6). The eigenspace E_{λ_1} is, thus, spanned by $\{V_i,\ i = 1, \ldots, k\}$. The eigenvectors V_i are only supported on A_i where they have a constant sign. However, there exists other eigenvector bases $\{U_i,\ i = 1, \ldots, k\}$ of E_{λ_1} given by

$$U_i = \sum_{j=1}^{k} \alpha_{ij} V_j,\ i = 1, \ldots, k,\ \alpha_{ij} \in \mathbb{R}. \tag{5.8}$$

Thus, depending on the choice of α_{ij}, each U_i may partition the "clouds" $\{A_i\}_{i=1}^k$ into configurations via its sign structure.

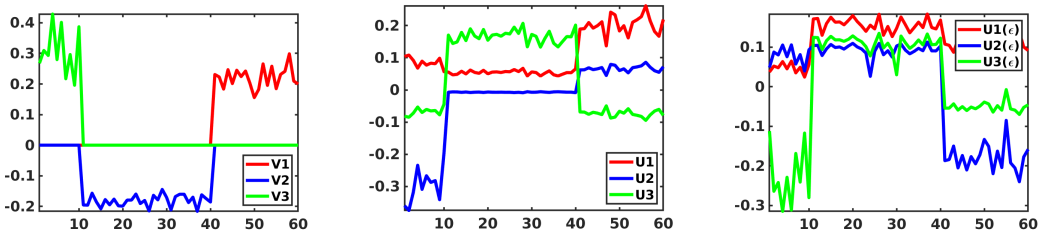

Figure 5.3: Eigenvectors V_i (left) and U_i (middle), $i = 1, 2, 3$, to the 3-fold eigenvalue 1 of the unperturbed matrix Q of the 60-state Markov chain (example 17), and eigenvectors to leading eigenvalues $U_i(\epsilon)$, $i = 1, 2, 3$, for the perturbed matrix $Q(\epsilon)$ (right).

Example 18 (cont.) *The eigenvectors V_i, $i = 1, 2, 3$ corresponding to the three-fold eigenvalue 1 of the unperturbed matrix are only supported on the respective invariant patterns*

(figure 5.3 (left)). In figure 5.3 (middle), the eigenvector U_1 is constructed to have a constant positive sign on the whole state space $\mathcal{S}$; it can be interpreted as a stationary distribution. U_2 yields a 2-partition of $\mathcal{S}$ by lumping together A_1 and A_2. Finally U_3 yields a 3-partition of $\mathcal{S}$, which corresponds exactly to the three invariant patterns that exist in the state space. In figure 5.3 (right) the leading eigenvectors for the perturbed matrix $Q(\epsilon)$ are shown. From their sign structures a 3-partition of $\mathcal{S}$ into almost-invariant patterns is obtained.

In the presence of perturbations, an explicit formula of the k analytic eigenvectors corresponding to the dominant eigenvalues – the eigenvalues clustered near 1 – can be found as

$$\begin{aligned} U_1(\epsilon) &= \pi(\epsilon) = [\pi_1(\epsilon), \pi_2(\epsilon), \ldots, \pi_N(\epsilon)],\ \pi_i(\epsilon) > 0, \\ U_i(\epsilon) &= \sum_{j=1}^{k} (\alpha_{ij} + \epsilon\beta_{ij}) V_j \\ &\quad + \epsilon \sum_{j=k+1}^{N} \frac{1}{1-\lambda_j(\epsilon)} \langle U_j, Q^{(1)} U_i \rangle_{\pi(\epsilon)}\ + O(\epsilon^2),\ i = 2, \ldots, k,\ \alpha_{ij}, \beta_{ij} \in \mathbb{R}. \end{aligned} \tag{5.9}$$

Formula (5.9) was stated and proven in [35] for the right eigenvectors of $Q(\epsilon)$. The proof is mainly based on ([24], Chp. 2) but with a particular focus on reversible stochastic matrices. Here, we only use left eigenvectors of $Q(\epsilon)$ since left and right dominant eigenvectors are both analytic for $\epsilon \in \mathbb{R}$ and are related by $U_i(\epsilon) = \mathcal{D}_N X_i(\epsilon)$, where $\mathcal{D}_N = \text{diag}([\pi_1, \pi_2, \ldots, \pi_N])$ and $\{X_i(\epsilon),\ i = 1, \ldots, N\}$ are the $\pi(\epsilon)-$orthogonal right eigenvectors of $Q(\epsilon)$. Note that $\text{sign}(U_i(\epsilon)) = \text{sign}(X_i(\epsilon))$.

The first term in the second equation in (5.9) suggests that the $U_i(\epsilon)'$s are actually ϵ-up-or-down-shifts of the basis V_j in equation (5.7), which were each supported on invariant patterns A_j. Thus, this shifting does not affect the sign structure of the unperturbed eigenvectors; see equation (6.14). However, the second term depends on the spectral gap $\frac{1}{1-\lambda_j(\epsilon)}$ between the Perron root 1 and the $N-k$ small magnitude eigenvalues of $Q(\epsilon)$. Therefore, this second term may have an influence on the sign structure of the unperturbed eigenvector, but only when a relatively small ϵ is chosen [35].

With this setting of the Markov chain and the lumped almost-invariant states, the sign structure of each dominant eigenvector in equation (5.7) yields a partition of the state space. Indeed, each $U_i(\epsilon)$ defines a partition into i nearly disjoint aggregates for $i = 2, \ldots, k$, via its sign structure. In addition, k dominant eigenvalues are a consequence of the occurrence of k almost-invariant patterns given by the supports of $U_k(\epsilon)$. Finally,

note that the remaining $N-k$ eigenvectors, corresponding to the spectrum $\{\lambda_j(\epsilon), j = k+1, \ldots, N\}$ bounded away from 1, cannot be interpreted as (5.9). Indeed, the supports of these eigenvectors do not correspond to invariant patterns. However, they may play an important role when it comes to studying the changes of the dominant almost-invariant patterns with respect to an external bifurcation parameter.

5.3 Incompressible 2D flows and almost-invariant sets

Since our study is motivated by geophysical applications including the splitting pattern of the Antarctic polar vortex in September 2002 in figure 1.1, we focus on models exhibiting vortices in their incompressible dynamics. As a first illustrative example, let us consider the following two-dimensional system of ordinary differential equations:

$$\begin{aligned} \dot{x}(t) &= -\pi \sin(\pi x)\cos(\pi x) \\ \dot{y}(t) &= \pi \cos(\pi x)\sin(\pi y) \end{aligned} \tag{5.10}$$

From the stationary behavior of (5.10), it is clear that every single orbit is periodic, see

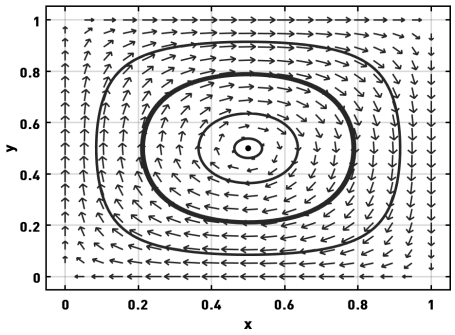

Figure 5.4: Phase plane of system (5.10) consisting of periodic orbits.

figure 5.4. Hence, the ensemble evolution of a set of initial points under the flow map ϕ^t yields a bundle of closed curves for sufficiently large t. Under this rotational dynamics, one can always extract a finite number of disjoint ring-like sets $\{A_1, A_2, \ldots, A_k\}$ that partition the phase space D so that the invariance equation $\rho_\mu(A_i) = 1$ holds, for every A_i, $i = 1, \ldots, k$. In this context, one may think of a set A_i as a bundle of invariant orbits. Note that this partition is not unique, given the particular behavior of (5.10). We will, nevertheless, choose to work with a fixed partition of k invariant sets. Therefore, as in section 5.1, let us suppose that the stationary dynamics within the discretized phase space yields a reducible diagonal block transition matrix P_N with k blocks. That is, the

reversibilized transformation Q_N in (5.4) has the form (5.6). In other words, the k block matrices of Q_N consist of clustered states such that each lumped state yields an invariant set $A_i,\ i = 1, 2, \ldots, k$.

In what follows, we will add an external perturbation to the reducible macroscopic dynamics so that the invariant sets persist but become almost-invariant sets $\{A_1(\epsilon), A_2(\epsilon), \ldots, A_k(\epsilon)\} \subset \mathcal{C}_N$. That is, $\rho_\mu(A_i(\epsilon)) \approx 1,\ i = 1, 2, \ldots, k$ as defined in equation (5.5). In [16, 36] an explicit model of the perturbation was introduced and analytically formulated. It consists of "shaking" every box B_i before and after applying the flow map ϕ^t. As a consequence, only those invariant sets that resist perturbations will continue to exist as robust almost-invariant sets and are, thus, relevant in real world settings. Under the perturbed dynamics, the transition matrix is given by

$$(P_N^t(\epsilon))_{ij} = \frac{m(B_\epsilon(\phi^t(B_\epsilon(B_i))) \cap B_j)}{m(B_\epsilon(\phi^t(B_\epsilon(B_i))))}. \tag{5.11}$$

B_ϵ is the ball centered at zero with radius ϵ, which can be thought of as the perturbation amplitude. $P_N^t(\epsilon)$ is actually the finite rank approximation of the explicitly diffused Perron-Frobenius operator; see [36] for more details and the numerical implementation.

As in section 5.2, the added perturbation yields a reversible row stochastic transition matrix $Q_N^t(\epsilon)$ from $P_N^t(\epsilon)$ analogously to (5.4), where $\pi(\epsilon)$ denotes the unique stationary density of $P_N^t(\epsilon)$. Hence, $Q_N^t(\epsilon)$ has k eigenvalues $\{\lambda_i^t(\epsilon)\}_{i=1}^k$ that satisfy the properties **(a)**, **(b)** and **(c)** outlined in section 5.2. The corresponding eigenvectors, denoted as $\{U_i^t(\epsilon)\}_{i=1}^k$, can be expressed as in equation (5.9).

Let $\{X_i^t(\epsilon)\}_{i=1}^k$ be the right eigenvectors of $Q_N^t(\epsilon)$ corresponding to the eigenvalues $\{\lambda_i^t(\epsilon)\}_{i=1}^k$. Then due to the self-adjoint property of $Q_N^t(\epsilon)$ with respect to the inner product $\langle \cdot, \cdot \rangle_{\pi^t(\epsilon)}$, we have for $j = 2, \ldots, k$

$$\lambda_j^t(\epsilon) = \max_{x \neq 0,\, x \in \mathbb{R}^N} \left\{ \frac{\langle Q_N^t(\epsilon)x, x \rangle_{\pi^t(\epsilon)}}{\|x\|^2_{\pi^t(\epsilon)}} \right\}, \tag{5.12}$$

under the $\pi^t(\epsilon)$-orthogonal constraint

$$\langle x, \mathbf{1} \rangle_{\pi^t(\epsilon)} = \langle x, X_2^t(\epsilon) \rangle_{\pi^t(\epsilon)} = \ldots = \langle x, X_{j-1}^t(\epsilon) \rangle_{\pi^t(\epsilon)} = 0.$$

Note that $\mathbf{1} = X_1^t(\epsilon) = [1, 1, \ldots, 1]$ denotes the right stationary distribution of $Q_N^t(\epsilon)$. Besides, (5.12) is a finite dimensional approximation of (3.28) in chapter 3. In [16, 36],

the eigenvalue $\lambda_2^t(\epsilon)$ and the corresponding left eigenvector $U_2^t(\epsilon) = \mathcal{D}_N X_2^t(\epsilon)$, $\mathcal{D}_N = \text{diag}([\pi^t(\epsilon)_1, \pi^t(\epsilon)_2, \ldots, \pi^t(\epsilon)_N])$ were used to approximate two robust maximal almost-invariant sets. Indeed, due to the $\pi^t(\epsilon)$-orthogonality relations among the right eigenvectors $\{X_i^t(\epsilon)\}_{i=1}^k$ and the positive sign of $X_1^t(\epsilon)$, the sign structure of $U_1^t(\epsilon)$ is given as

$$\text{sgn}(U_1^t(\epsilon)) = (+,+,+,+,\ldots,+,+,+,+,+,\ldots,+).$$

We can therefore predict the sign structure of $U_2^t(\epsilon)$ as follows

$$\text{sgn}(U_2^t(\epsilon)) = (+,+,+,+,\ldots,+,-,-,-,-,-,\ldots,-),$$

subject to a convenient box reordering. Hence, it follows that $U_2^t(\epsilon)$ yields positive and negative level sets, which partition the phase space into two dominant almost-invariant sets, whenever $\lambda_2^t(\epsilon) \approx 1$. Similarly, since further $k-2$ eigenvalues are clustered near 1, each eigenvector $U_j^t(\epsilon)$ yields a sign structure that may be sorted so that j almost-invariant sets are obtained. In [35], all $k-1$ leading eigenvectors are used to compute almost-invariant sets. This method does not need the corresponding eigenvalues, but only the sign structures of the eigenvectors. However, in this work we use the eigenvectors separately, because we ultimately need to study the trends of the corresponding eigenvalues to understand bifurcation of patterns.

Given (5.10), we can numerically compute and visualize the eigenvector patterns $U_j^t(\epsilon)$, $j = 1, 2, \ldots, k$, as well as their corresponding eigenvalues $\lambda_j(\epsilon)$. For this we use GAIO[37], which is a MATLAB-based software package for set-oriented numerics in dynamical systems. We approximate the flow map by using a fourth order Runge

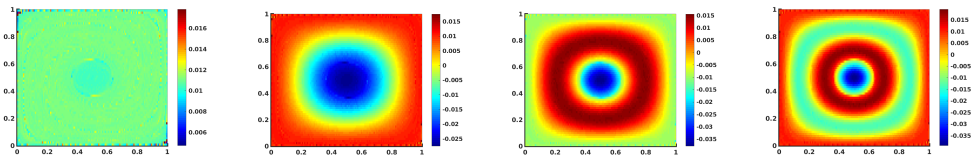

$U_1^t(\epsilon)$ $U_2^t(\epsilon)$ $U_3^t(\epsilon)$ $U_4^t(\epsilon)$

Figure 5.5: First 4 dominant eigenvectors of $Q_N^t(\epsilon)$ for model (5.10).

Kutta ODE solver with a time interval of length 1 and step size of $h = 0.01$, i.e 100 time steps. The domain is subdivided into 2^{depth} rectangular grid sets (boxes). Here, we use $depth = 13$, which gives $N = 2^{13} = 8192$ boxes B_i that partition the phase space D. In each box 900 test points are uniformly sampled as initial data for constructing the

transition probabilities of the $N \times N$-transition matrix.

In figure 5.5, the $k = 4$ dominant eigenvectors are plotted, with the corresponding eigenvalues shown in figure 5.6. These are all clustered near 1, as the result of additional external perturbations. Note that the numerical discretization induces a small amount of noise in the order of magnitude of the box diameters ([12], Lemma 2.2). That is, the numerical discretization directly yields an approximation of (5.11), and, hence, it is not necessary to add explicit diffusion in practice, although it is required on the theoretical level. Also note that the leading eigenvector $U_1(\epsilon)$ is approximately constant due to area preservation of the underlying system (5.10), with some small numerical artefacts at the boundary of the domain.

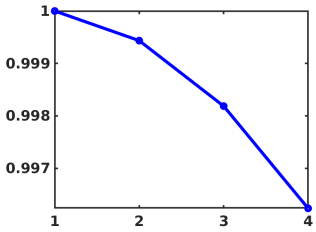

Figure 5.6: First 4 dominant eigenvalues of $Q_N^t(\epsilon)$ from system (5.10).

A set-oriented bifurcation analysis of a dynamical system will be exclusively based on studying the changes of the spectral data as a response to qualitative changes in the underlying dynamics. That is, one needs to focus on both the eigenvectors and their corresponding eigenvalues. In this way, trends of the spectral data can be used to understand whether or not there is hint of any qualitative changes of patterns generated by the corresponding eigenvectors. But, beforehand, we will first consider some toy models and investigate bifurcations of patterns in an experimental manner.

5.4 Numerical experiments of bifurcation

Now, we start to dive into the main purpose of this work through an experimental approach. We study the changes in the trends of the dominant spectrum when the almost-invariant patterns undergo different qualitative changes. This may be understood as a ”bifurcation analysis” of the stationary macroscopic dynamics of the Markov chain. The process resulting in qualitative changes of a pattern can only occur in two ways: Either it starts from the inside towards the outside of the pattern or the other way round.

Example 19 *We revisit the* 60*-states Markov chain with the perturbed* 3 *invariant patterns as introduced in example 17. In this experiment, we want to understand how the spectrum behaves when the change of the pattern starts from its boundary. Thus, as shown in figure*

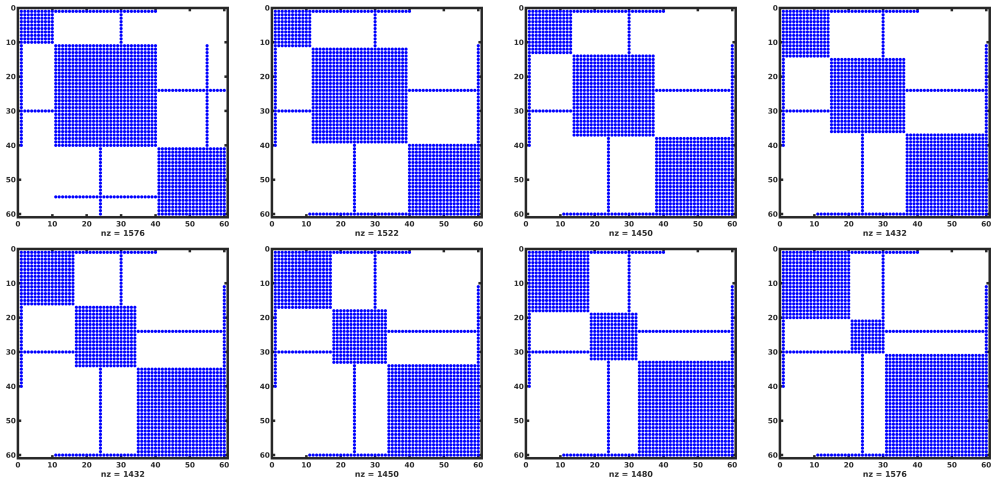

Figure 5.7: Different transition matrices of example 19, where the outer two almost-invariant patterns grow at the expense of the center one.

5.7, we manually decrease uniformly the size of the middle invariant pattern A_2*, while increasing the size of both* A_1 *and* A_3*, simultaneously. These changes are captured by the dominant spectrum as illustrated in figure 5.8. Eigenvalue* $\lambda_3(\epsilon)$ *decreases in magnitude as*

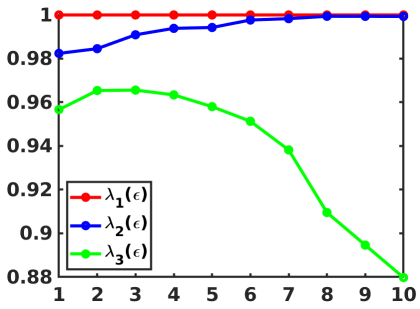

Figure 5.8: Spectral signature of the shrinking of one almost-invariant pattern in example 19, with two other patterns growing and becoming more invariant.

the middle pattern A_3 *shrinks in size. This shrinking process is captured in the eigenvector* $U_3(\epsilon)$*, where the support of* $U_3(\epsilon)$ *in* A_3 *is becoming smaller and smaller, as demonstrated in figure 5.9. The opposite is noticed in the changing process of* $U_2(\epsilon)$*. The corresponding eigenvalue* $\lambda_2(\epsilon)$ *approaches* 1 *as* $\lambda_3(\epsilon)$ *decreases. In this process, one can clearly see that the system tends to become nearly reducible with two growing lumped states* $A_1(\epsilon)$ *and*

$A_3(\epsilon)$. *That explains the growth of* $\lambda_2(\epsilon)$ *towards* 1. *It is necessary to understand the*

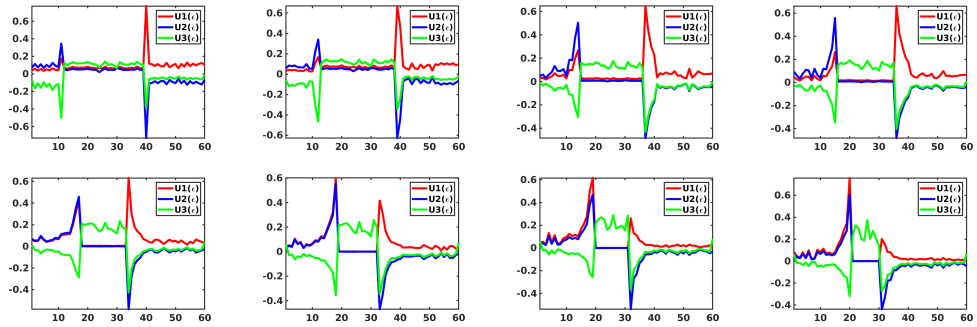

Figure 5.9: Changes in the three dominant eigenvectors for the transition matrices shown in figure 5.7.

behavior of the eigenvalues and their correct interpretation with respect to the dynamics of the almost-invariant patterns. Indeed, this experiment clearly suggests a relationship between the eigenvalues and the size of the patterns.

Example 20 *Here the qualitative change is provoked from the interior of the middle pattern* A_2. *The aim is to experiment the behavior of the spectrum with respect to a sudden growing change from a local region. The corresponding transition matrices of the gradually changed Markov chain are shown in figure 5.10. The evolution of the dominant eigenvalues shown in figure 5.11 indicates the importance of the eigenvalue* $\lambda_4(\epsilon)$, *which is not part of the dominant spectrum at first. It increases very quickly in magnitude until it crosses* $\lambda_3(\epsilon)$. *The corresponding eigenvector,* $U_4(\epsilon)$, *is supported on the newly born almost-invariant pattern as illustrated in figure 5.12.*

Unlike the first example, there is no variation in the trends of the eigenvalues $\lambda_i(\epsilon)$, $i = 1, 2, 3$. *This is because the shapes of the first three invariant patterns* A_i, $i = 1, 2, 3$ *have not been affected by the sudden birth of the new pattern* A_4. *Therefore, in this experiment we clearly see that the trends of the three dominant eigenvalues are not relevant in order to predict the changes occurring in the dynamics. This can be understood by the fact that the change is primarily local and is only happening inside* A_3. *Again, the variation in the size of the almost-invariant patterns seems to be a crucial component for understanding the trends of the eigenvalues.*

Example 21 *Finally, in this experiment we summarize the behaviors observed in the two previous examples 19-20 within one toy model. At the beginning there are two coexisting*

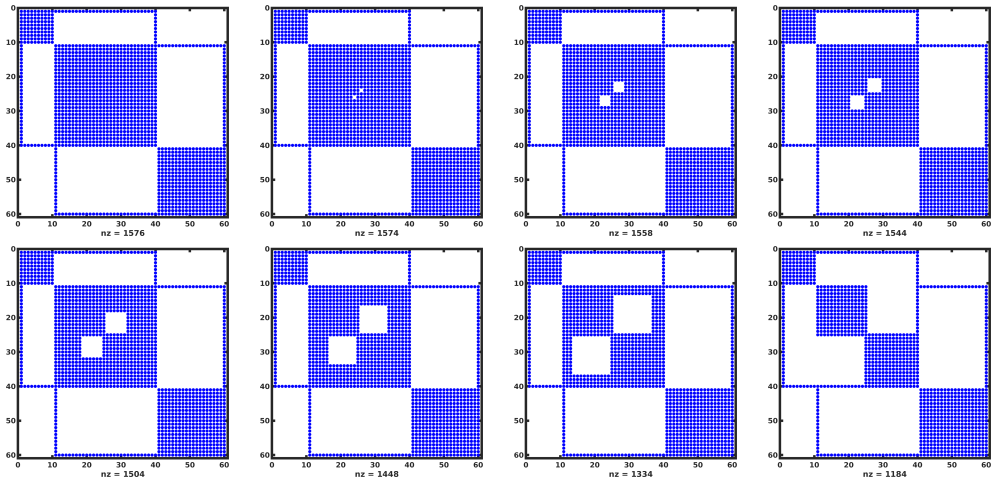

Figure 5.10: Different transition matrices of example 20, where the split of the central almost-invariant pattern is provoked locally in its interior.

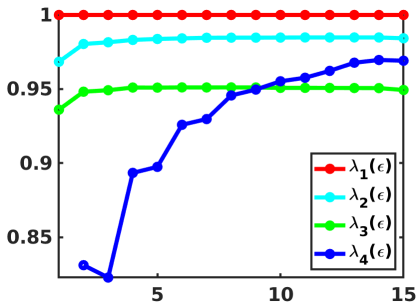

Figure 5.11: Spectral signature of the splitting of an almost-invariant pattern in example 20.

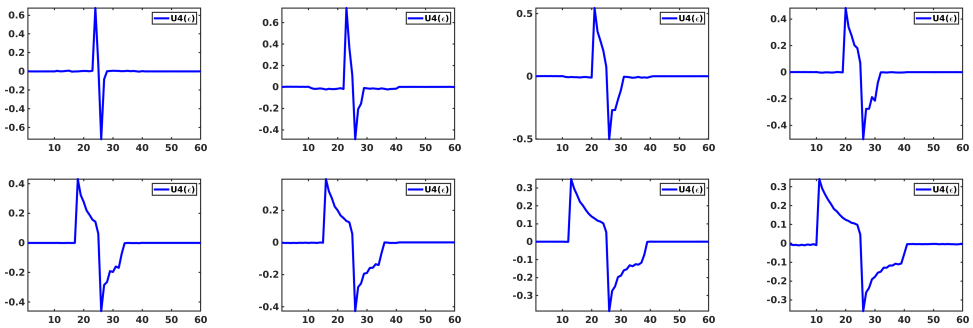

Figure 5.12: Changes of the previously subdominant eigenvector $U_k(\epsilon)$ (i.e. $k = 4$) in example 20.

almost-invariant patterns. Due to implicitly tuning an parameter, which is external to the model, a new pattern arises continuously inside one of these almost-invariant sets. While this new pattern grows, the two other almost-invariant sets shrink. This is captured in the behavior of the dominant eigenvalues, see figure 5.13. Indeed, as in equation (5.9)*,* $\lambda_3(\epsilon)$

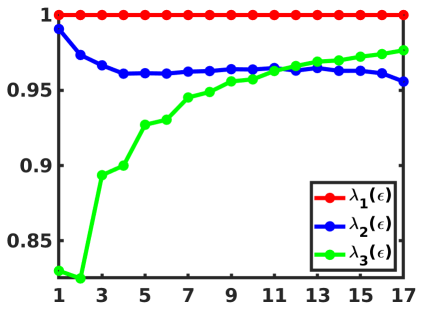

Figure 5.13: Spectral signature of a splitting of an almost-invariant pattern while another pattern is decreasing in size as described in example 21.

appears to rise from the small magnitude eigenvalues $\{\lambda_j(\epsilon),\ j = k+1,\ldots,N\}$*, finally crossing* $\lambda_2(\epsilon)$*, which is decreasing.*

Although we have only shown very specific settings in examples 19-21, the spectral effects of the pattern changes that we have illustrated are universal. In particular, it becomes clear that the study of qualitative changes of patterns, which are visible in the dominant eigenvectors, depends strongly on an understanding of the trends of corresponding eigenvalues. Moreover, any changing process within the almost-invariant patterns $A_i(\epsilon)$, $i = 1,\ldots,k$ will be first sensed in the smallest dominant eigenvalue and corresponding eigenvector eigenvector $U_k(\epsilon)$. Indeed, the sign structure of the eigenvector $U_k(\epsilon)$ describes the k existing almost-invariant patterns, exhaustively. For instance, in figure 5.5, the 4^{th} eigenvector corresponds to the partition of the state space into four almost-invariant patterns. In particular, if $k = 2$, then $U_2(\epsilon)$ partitions the state space into two almost-invariant patterns. This particular case has been used in many works [15, 16, 36] in the context of the numerical computation optimal almost-invariant sets from the global evolution of a dynamical system. The ultimate goal is to be able to recognize early warning signals of these critical changes of almost-invariant patterns.

The trends of the eigenvalues and behavior of the state space as summarized in table 5.1 will facilitate the understanding of spectral behavior for more realistic systems. Note that here, we focused a lot on the splitting and/or shrinking behavior in state space, because we are ultimately interested in understanding such scenarios in real world systems.

Behavior in state space	Spectrum	Eigenvectors
$A_i(\epsilon)$ shrinks and disappears. At least one $A_j(\epsilon)$, $j \neq i$ grows.	$\lambda_i(\epsilon) \searrow$ while $\lambda_j(\epsilon) \nearrow$.	Support of $U_i(\epsilon)$ decreases, support of $U_j(\epsilon)$ increases.
$A_i(\epsilon)$ splits inside due to new growing $A_{k+1}(\epsilon)$. $A_j(\epsilon)$, $j \neq i$ are unaffected.	$\lambda_{k+1}(\epsilon) \nearrow$ and transport in $A_i(\epsilon)$ decreases due to increasing barrier inside $A_i(\epsilon)$.	$U_{k+1}(\epsilon)$ is supported on growing new sets inside $A_i(\epsilon)$.
$A_i(\epsilon)$ shrinks because $A_{k+1}(\epsilon)$ increases from inside $A_i(\epsilon)$.	$\lambda_i(\epsilon) \searrow$ while $\lambda_{k+1}(\epsilon) \nearrow$, eventually crossing each other. Then $\lambda_{k+1}(\epsilon) > \lambda_i(\epsilon)$.	$U_{k+1}(\epsilon)$ is supported on growing new sets inside $A_i(\epsilon)$. Support of $U_i(\epsilon)$ decreases.

Table 5.1: Summarized results of the toy model experiments 19-21.

5.5 Bifurcation of almost-invariant patterns

Now we study bifurcations of almost-invariant patterns generated by explicit mathematical models. We will consider the setting where there is initially a particular almost-invariant pattern centered at $(0,0)$ and surrounded by ring-like patterns, for each eigenvector of the k dominant eigenvectors such as in figure 5.5. The motivation for this is that this particular pattern mimics real world vortices. Following our experiments in examples 19-21, which are summarized in table 5.1, we will track the changes of the k dominant eigenvectors and eigenvalues with respect to a concrete external bifurcation parameter p. Thus, for the feasibility of this continuation task, we assume a fixed perturbation strength ϵ during all of the process. That is, the variations of the k eigenvalues and eigenvectors will only depend on the bifurcation parameter $p \in \mathbb{R}$.

As a first case study, we consider the p-parametrized two-dimensional system

$$\begin{aligned} \dot{x} &= y \\ \dot{y} &= px - x^5 \end{aligned} \tag{5.13}$$

$p \in \mathbb{R}$. System (5.13) is a conservative Duffing-type oscillator and was introduced in chapter 4. Recall that the classical bifurcation occuring in (5.13) consists of the qualitative change of the unique elliptic fixed point $(0,0)$, for $p < 0$, into a local saddle fixed point, for $p > 0$. That is, a pitchfork bifurcation occurs when $p = 0$, which has global effects on the dynamics. For $p < 0$, the stationary dynamics consists of rotating periodic orbits centered at the unique fixed point $(0,0)$. These are destroyed, for $p > 0$, with the emergence of

two symmetric elliptic fixed points at $(\sqrt[4]{p}, 0)$ and $(-\sqrt[4]{p}, 0)$, as illustrated in figure 5.14.

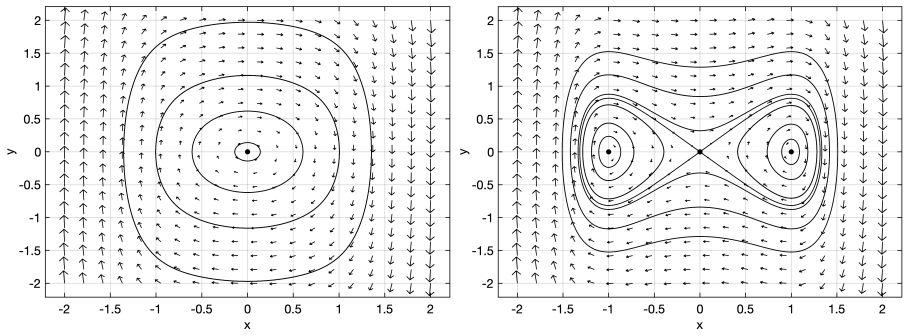

Figure 5.14: Phase plane of system (5.13) for parameters $p = -1$ (left) and $p = 1$ (right).

To prepare for our spectral analysis, a p-parametrized version of equation (5.9) may now be restated as follows: For each p, the stationary distribution is given as

$$\pi(\epsilon, p) \equiv U_1(\epsilon, p) = [\pi_1(\epsilon, p), \pi_2(\epsilon, p), \ldots, \pi_N(\epsilon, p)], \ \pi_i(\epsilon) > 0, \ \forall \ p,$$

and for each $i = 2, \ldots, k$,

$$\begin{cases} U_i(\epsilon, p) = \sum_{j=1}^{k} (\alpha_{ij} + \epsilon\beta_{ij}) V_j(p) \\ \qquad\qquad + \epsilon \sum_{j=k+1}^{N} \dfrac{1}{1 - \lambda_j(\epsilon, p)} \langle U_j(p), Q^{(1)} U_i(p) \rangle_{\pi(\epsilon,p)} + O(\epsilon^2), \ \alpha_{ij}, \beta_{ij} \in \mathbb{R}, \\ \\ \lambda_i(\epsilon, p) > \lambda_j(\epsilon, p), \ j = k+1, \ldots, N. \end{cases} \tag{5.14}$$

Note that with a fixed ϵ, the additional inequality constraint in (5.14)

$$\lambda_i(\epsilon, p) > \lambda_j(\epsilon, p), \ i = 1, 2, \ldots, k, \ j \geq k+1 \tag{5.15}$$

is always satisfied whenever the changes in p leave the qualitative behavior of system (5.13) unaffected. Indeed, due to the perturbation effect, $\lambda_j(\epsilon, p) < 1$, $j = k+1, \ldots, N$ are the small magnitude real eigenvalues which converge to 0 when ϵ increases. However, when ϵ is fixed, the changes in p may qualitatively affect the underlying dynamics. Thus, it makes sense to measure a susceptible radical growth scenario of the $\lambda_j(\epsilon, p) < 1$, $j = k+1, \ldots, N$, among many other possible scenarios.

5.5.1 Spectral signature of the classical bifurcation

Unlike the dominant eigenvectors (as shown in figure 5.5 for system (5.10)) the remaining $N-k$ eigenvectors $U_j(\epsilon,p)$, $j=k+1,\ldots,N$ may not be supported on the whole state space. They are referred as the "weak modes" eigenvectors and may not carry dynamically useful information, compared to the k "dominant modes" eigenvectors. However, due to the nature of the global behavior of (5.13) illustrated in figure 5.14, the global classical bifurcation yields a radical change only within a local isolated neighborhood of $(0,0)$. We refer to the latter as the critical neighborhood $\mathcal{D}$. Indeed, far from $\mathcal{D}$, closed trajectories still remain qualitatively the same before and after the bifurcation; see figure 5.14. Therefore, we will first find a spectral version of the classical bifurcation by means of the non-dominating $N-k$ part of the spectrum. That is, we will consider "weak modes" eigenvectors which are only supported on $\mathcal{D}$. Note that a special technique to finding those particular eigenvectors is still an open question. Their existence was noticed earlier in [19], but no particular further study about them was made, whatsoever. In this work, we use them to design a spectral bifurcation diagram of the global classical bifurcation occurring in (5.13). They will also play an import role when studying the bifurcation of "dominant mode" eigenvectors pattern.

The numerical approximation of the spectra is done with exactly the same settings as in section 5.3. However, the system (5.13) is open, which means that some test points will leave the domain of interest under the evolution of the flow map. To fix this issue, an additional box is added in order to capture all the image points that are being mapped out of the initial domain D when computing the transition matrix. Finally, this temporary box will be removed from the eigenvector entries by just considering the 2^{depth} first entries. Figure 5.15 shows the changes of two small magnitude eigenvalues that belong to $\{\lambda_j(\epsilon,p), j=k+1,\ldots,N\}$. We denote by $\lambda_1'(\epsilon,p)$ the green curve of eigenvalues with corresponding eigenvectors $U_1'(\epsilon,p)$, in figure 5.16. Likewise, $\lambda_2'(\epsilon,p)$ corresponds to the red curve in figure 5.15; their corresponding eigenvectors $U_2'(\epsilon,p)$ are shown in Figure 5.17.

In figures 5.16-5.17, the patterns of $U_1'(\epsilon,p)$ and $U_2'(\epsilon,p)$ change in size, as the bifurcation parameter p varies. Note that their sign structure remains the same. Besides, these eigenvector patterns are only supported on a small isolated neighborhood of $(0,0)$, according to the discretization depth of the phase space. In figure 5.15, the eigenvalues $\lambda_1'(\epsilon,p)$ and $\lambda_2'(\epsilon,p)$ are initially very small compared to 1. They increase linearly fast together side-by-side until $p=0$. Then they part ways: $\lambda_1'(\epsilon,p)$ continues to increase,

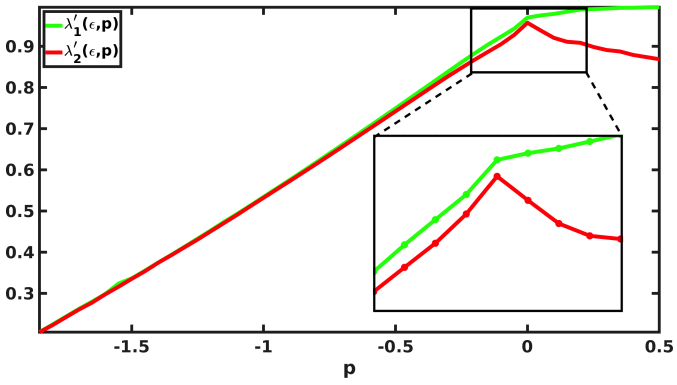

Figure 5.15: Spectral version of the classical bifurcation diagram with a zoomed diagram in the vicinity of the bifurcation (inlet). Two subdominant eigenvalues $\lambda_1'(\epsilon, p)$ and $\lambda_2'(\epsilon, p)$ rise towards one.

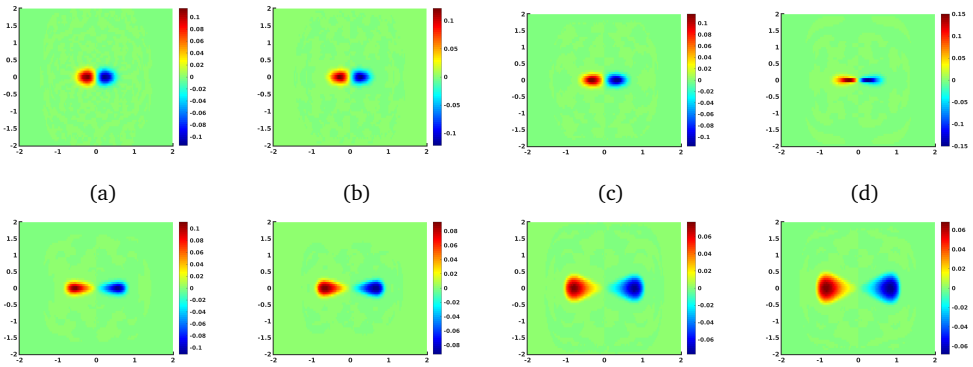

Figure 5.16: Changes of the first "weak modes" patterns from $U_1'(\epsilon, p)$ for increasing p.

while $\lambda_2'(\epsilon, p)$ starts to decrease. That is why figure 5.15 is referred to as the spectral version of the classical pitchfork bifurcation diagram of system (5.13) in analogy to the classical pitchfork bifurcation diagram (see e.g. [10], Chapter 3, p. 146).

In figures 5.16-5.17, one sees that the sign structure of $U_1'(\epsilon, p)$ is symmetric with respect to the y-axis, while the sign structure of $U_2'(\epsilon, p)$ is symmetric with respect to the x-axis. As $p < 0$ increases towards zero, both eigenvector patterns expand slowly and symmetrically along the x-axis, but remain nearly constant in the y-direction. This is intrinsic to the underlying dynamical system, see figures 5.16-5.17 (a)-(c). At $p = 0$, the fixed point $(0, 0)$ bifurcates, which is particularly well observed in figures 5.16-5.17 (d).

Another way to see the classical bifurcation is illustrated in figure 5.18. Indeed, the linearization of (5.13) around the fixed point $(0, 0)$ yields a two-dimensional matrix

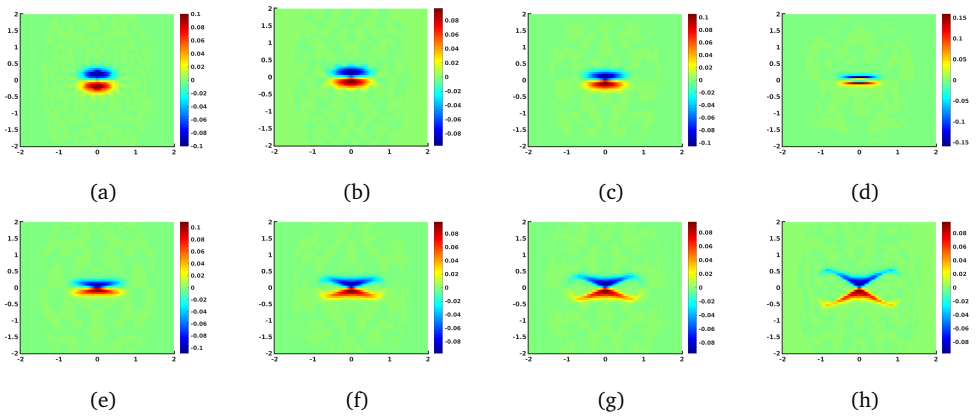

Figure 5.17: Changes of the second "weak modes" patterns from $U_2'(\epsilon, p)$ for increasing p.

whose eigenvalues are purely imaginary. With $\gamma_1 = i\sqrt{-p}$ and $\gamma_2 = -i\sqrt{-p}$ being the eigenvalues of the linearized system, the corresponding (generalized) eigenvectors are $v_1 = [x,\, y = \gamma_1 x]^\intercal$ and $v_1 = [x,\, y = \gamma_2 x]^\intercal$, respectively. Let $E_1^c(p)$ and $E_2^c(p)$ be the (generalized) eigenspaces of v_1 and v_2, respectively, depicted as the two intersecting red lines in figure 5.18(a)-(c). Then $E^c(p) = E_1^c(p) \bigoplus E_2^c(p)$ yields the two-dimensional subspace spanned by $E_1^c(p)$ and $E_2^c(p)$. In figure 5.18(a)-(c), $E^c(p)$ is the plane generated by the intersection of the two red lines. Therefore, there exists an invariant manifold denoted by $W^c(p)$ that is tangent to $E^c(p)$ at $(0, 0)$. This is known as the center manifold theorem ([10], Chapter 3, p. 127) and its main purpose is to isolate the complicated asymptotic behavior of the flow by locating such an invariant manifold W^c. In system (5.13), for negative p, every closed orbit is a boundary of a center manifold which is tangent to $E^c(p)$ at $(0, 0)$.

Notably, closed orbits are given by q-level sets of the derived Hamiltonian functions $H_q(x, y, p)$ for different p. Therefore, there is a constant $\bar{q}$ small enough such that $\{H_{\bar{q}}(x, y, p) = \bar{q}\}$ isolates the asymptotic dynamics of the flow near $(0, 0)$ from the rest. The blue closed curve shows $\{H_{\bar{q}}(x, y, p) = \bar{q}\}$ in figure 5.18(a)-(d). For negative p, the eigenspace plane $E^c(p)$ partitions the interior of the closed curve $\{H_{\bar{q}}(x, y, p) = \bar{q}\}$ into four regions which are two-by-two symmetric similar to $U_1'(\epsilon, p)$ and $U_2'(\epsilon, p)$ in figure 5.16 and figure 5.17, respectively. As p increases towards 0, the slopes and the intersection angles of $E_1^c(p)$ and $E_2^c(p)$ decrease and the closed curve expands horizontally, while remaining constant vertically. Again, this is analogous to the variations of $U_1'(\epsilon, p)$ and $U_2'(\epsilon, p)$, for negative p. In this way, the local behavior of the flow near the origin

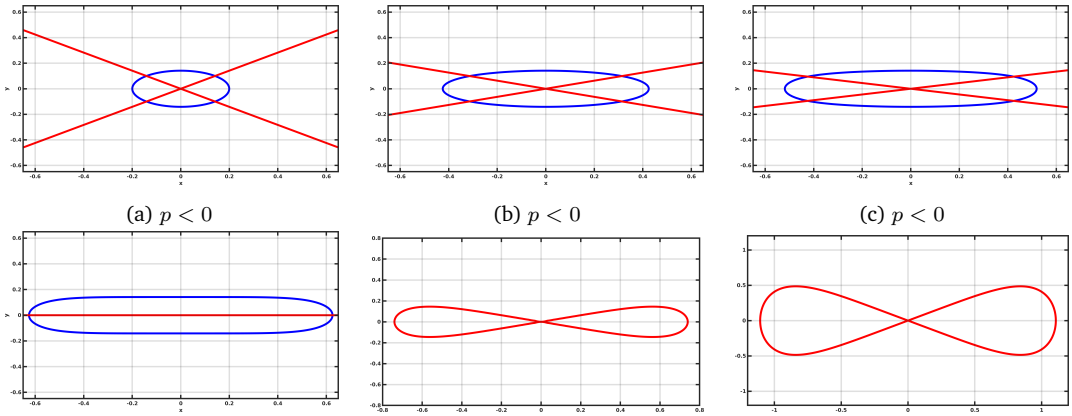

(a) $p < 0$ (b) $p < 0$ (c) $p < 0$

(d) $p = 0$ (e) $p > 0$ (f) $p > 0$

Figure 5.18: Local dynamics of system (5.13) near the origin. For $p \leq 0$ we obtain center manifolds, for $p > 0$ homoclinic manifolds.

is cast into $U_1'(\epsilon, p)$ and $U_2'(\epsilon, p)$ for negative p. This is another way of providing a better understanding of complicated asymptotic dynamics near $(0, 0)$, from a probabilistic approach. Note that the choice of $\bar{q}$ is heuristic since there no way to have an exact $\bar{q}$ in order to have the exact local manifold that supports the corresponding eigenvectors.

For $p = 0$, $E_1^c(p)$ and $E_2^c(p)$ disappear as a consequence of the classical bifurcation. Note that figure 5.18(d) is also in agreement with figure 5.16(d) and figure 5.17(d). For p positive, there are three fixed points: Two elliptic fixed points $(-\sqrt[4]{p}, 0)$ and $(\sqrt[4]{p}, 0)$ and one saddle fixed point $(0, 0)$.

The qualitative behavior of the dynamics changes radically with the emergence of two symmetric homoclinic orbits, as shown in 5.18(e). We refer to the latter as the homoclinic manifold, since neighboring trajectories are periodic and tangent to it. As p increases, the homoclinic manifold increases in size (see figure 5.18(e)-(f)) because $g(p) := \sqrt[4]{p}$ is an increasing function of p. Nearby solution curves tend to be attracted through the y-direction and repelled through the x-direction. Indeed, figure 5.18(e)-(f) shows that the homoclinic manifold is concave in the y-direction and convex in the x-direction. Besides, the larger p gets, the more does the curvature of the homoclinic manifold grow.

This implies immediately that the global behavior of the dynamics becomes attractive along the y-direction. Thus, the support of $U_2'(\epsilon, p)$ shrinks symmetrically on both sides of x-axis, as shown in figure 5.17(e)-(h) and, as a matter of fact, the eigenvalues $\lambda_2'(\epsilon, p)$ decrease. On the other hand, the dynamics repels along the x-direction. Thus, the support

of $U_1'(\epsilon, p)$ expands symmetrically on both sides of the y-axis and is simultaneously enrolled into the two newly co-existing homoclinic orbits; see figure 5.14. The latter expand as p increases from zero. As a consequence, the eigenvectors $U_1'(\epsilon, p)$ carry almost-invariant sets bounded by the homoclinic orbits, for $p > 0$. Moreover, the corresponding eigenvalues $\lambda_1'(\epsilon, p)$ increase towards 1, see figure 5.15.

Recall that these eigenvalues belong to the set of $N-k$ small magnitude spectrum. Hence, the continuous rise of $\lambda_1'(\epsilon, p)$ towards 1, as a consequence of the classical bifurcation, will eventually question the well-definiteness of k dominant eigenvectors and their corresponding eigenvalues. Indeed, (5.14) is no longer valid if the additional inequality constraint fails. In the next subsection, this will play a key role for us to characterizing bifurcations of almost-invariant sets.

5.5.2 Predicting bifurcation of almost-invariant patterns

Here, we will characterize bifurcations of almost-invariant patterns and deduce the corresponding generic early warning signs. As mentioned before, we are interested in the changes of the particular pattern centered in $(0, 0)$ and located in each dominant eigenvector pattern. As shown in figure 5.5, given any dominant eigenvector $U_j(\epsilon, p)$, $j = 2, \ldots, k$, the particular almost-invariant pattern, denoted $\mathcal{P}_j$, $j = 2, \ldots, k$, is the j^{th} partition element surrounded by all ring patterns. Indeed, every $U_j(\epsilon, p)$, $j = 2, \ldots, k$ yields j almost-invariant patterns which partition the state space. In particular, for $j = 2$, the second dominant eigenvector yields two almost-invariant patterns partitioning the state space. Besides, one of the patterns yields $\mathcal{P}_2$, which is known as the maximal almost-invariant set [16]; see figure 5.5(b). Moreover, $(U_2(\epsilon, p), \mathcal{P}_2)$ is usually a good candidate for modelling real world isolated patterns such as atmospheric vortices.

Given the bifurcation diagram in figure 5.15 and the inequality constraint (5.15), we set the relation

$$\lambda_1'(\epsilon, p) < \lambda_j(\epsilon, p), \;\; j = 2, \ldots, k, \tag{5.16}$$

which is true whenever $p \leq 0$. Moreover, for $p \leq 0$, the dominant patterns are stable in the sense that there is no qualitative change in their sign structure. In figure 5.19, we plot eigenvector patterns for $p \leq 0$. Note that the leading eigenvector is constant and therefore not shown. Even though there is a classical bifurcation in (5.13) at $p = 0$, one notices that the dominant eigenvector patterns $U_2(\epsilon, p)$ and $U_3(\epsilon, p)$ in figure 5.19 are

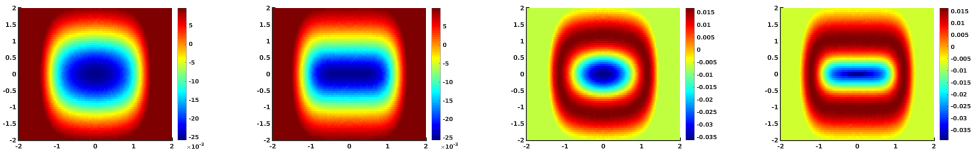

$U_2(\epsilon, p < 0)$ $U_2(\epsilon, p = 0)$ $U_3(\epsilon, p < 0)$ $U_3(\epsilon, p = 0)$

Figure 5.19: $U_j(\epsilon, p \leq 0),\ j = 2, 3.$

qualitatively the same for $p < 0$ and $p = 0$. As a matter of fact, it suffices to investigate the bifurcation of almost-invariant patterns for positive values of p, as it can only happen in that parameter range. Indeed, when p becomes positive, $\lambda_1'(\epsilon, p)$ continues to increase monotonically to eventually become the second dominant eigenvalue after the eigenvalue 1. In fact, $\lambda_1'(\epsilon, p)$ will cross, in cascade, all the $k - 1$ nontrivial dominant eigenvalues, as illustrated in figure 5.20.

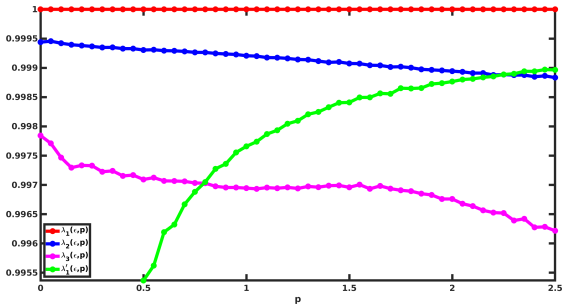

Figure 5.20: Spectral indicators of bifurcations of almost-invariant patterns in system (5.13). Three dominant eigenvalues $\lambda_1(\epsilon, p) = 1$ (red), $\lambda_3(\epsilon, p) < \lambda_2(\epsilon, p) < 1$ (magenta, blue) and the rising eigenvalue $\lambda_1'(\epsilon, p)$ (green) which intersects first the $\lambda_3(\epsilon, p)$-curve and then the $\lambda_2(\epsilon, p)$-curve.

For $p > 0$, the global dynamics attracts along the y-axis and repels along the x-axis. As a consequence, the pattern generated by $U_1'(\epsilon, p)$ expands in size, since it is supported in the region bounded by the two homoclinic orbits. On the other hand, the attractivity through the y-axis causes a shrinking process of the $k - 1$ dominant eigenvectors patterns $U_j(\epsilon, p),\ j = 2, \ldots, k$. Thus, as explained in the toy model experiments 19-21, we can define a set-oriented version of a degeneracy as

$$\lambda_1'(\epsilon, p) = \lambda_j(\epsilon, p),\ \ j = 2, \ldots, k,\ \ \forall\ p > 0. \tag{5.17}$$

It follows that $\mathcal{P}_j,\ \ j = 2, \ldots, k$, bifurcates in the sense of a splitting, whenever equation (5.17) holds. Thus, according to figure 5.20, there is a cascade of two bifurcations.

Every bifurcation occurs at a parameter $p > 0$ where the support of $U_1'(\epsilon, p)$ expands far enough to erupt out of $\mathcal{P}_j,\ j = 2, 3$. Indeed, at $p = 0$ the support of $U_1'(\epsilon, p)$ is, a priori, contained in the support of each $U_j(\epsilon, p),\ j = 2, 3$, specifically in $\mathcal{P}_j,\ j = 2, 3$. This scenario changes radically the sign structures of $U_j(\epsilon, p),\ j = 2, 3$ and, hence, the latter can no longer be expressed as in (5.9). The crossings occur in cascade from the smallest dominant eigenvalue to the biggest eigenvalue. In figure 5.22 (left), one can see that $\lambda_3(\epsilon, p)$ is crossed first. Later figure 5.22 (right) shows the last crossing scenario where $\lambda_1'(\epsilon, p) = \lambda_2(\epsilon, p)$ after which $\lambda_1'(\epsilon, p)$ becomes the dominant eigenvalue after the eigenvalue 1. The eigenvector patterns from $U_2(\epsilon, p)$ and $U_3(\epsilon, p)$ undergo, respectively, a splitting process of $\mathcal{P}_3$ in figure 5.21 and of $\mathcal{P}_2$ in figure 5.23. Note that the splitting of the patterns $\mathcal{P}_j,\ j = 2, 3$ does not occur suddenly but gradually. In fact, one observes the decreasing process of $\lambda_j(\epsilon, p),\ j = 2, 3$ before the crossing, which could be classified as an early warning signal.

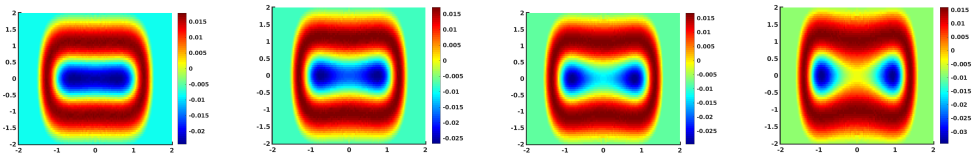

Figure 5.21: Splitting process of the pattern $\mathcal{P}_3$ for increasing $p \geq 0$.

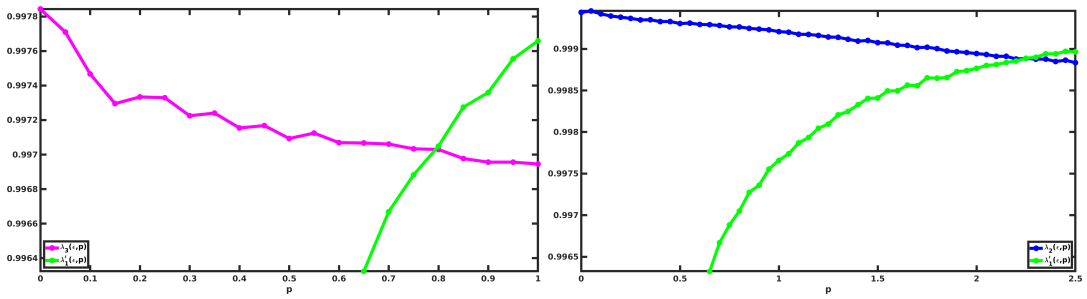

Figure 5.22: Crossings of previously dominant eigenvalues when patterns $\mathcal{P}_3$ and $\mathcal{P}_2$ bifurcate under variation of p. Left: $\lambda_3(\epsilon, p)$ (magenta) vs. $\lambda_1'(\epsilon, p)$ (green); right: $\lambda_2(\epsilon, p)$ (blue) vs. $\lambda_1'(\epsilon, p)$ (green).

When the cascade of crossing eigenvalues (bifurcations) ends, $\lambda_1'(\epsilon, p)$ becomes the second dominant eigenvalue after the eigenvalue 1. Indeed, the global dynamics of (5.13) becomes nearly reducible with two coexisting symmetric vortices. The dominant eigenvector pattern for $p > 0$ is shown in figure 5.24. The corresponding transition matrix

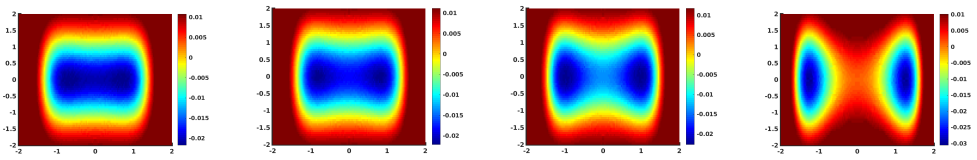

Figure 5.23: Splitting process of the pattern $\mathcal{P}_2$ for increasing $p \geq 0$.

is shown in figure 5.25 and it is nearly reducible in accordance with the post-bifurcation global dynamics. In fact, one can see that the global behavior of the system is now completely described by the support of $U_1'(\epsilon, p)$.

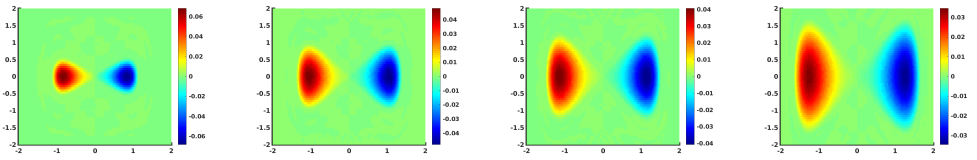

Figure 5.24: Dominant eigenvector pattern $U_1'(\epsilon, p)$ post-bifurcation.

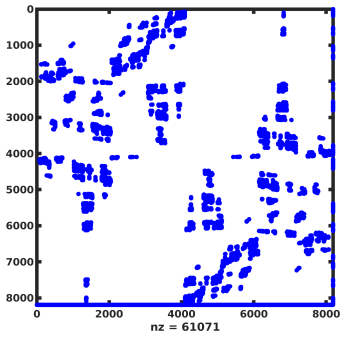

Figure 5.25: Transition matrix post-bifurcation.

5.5.3 Transition from one vortex to a double vortex dynamics

In this case study, we want to show an example of a transition of vortices that is not a bifurcation in the sense of a splitting. The aim is to reinforce the results about the spectral indicators before a pattern splitting. We study an incompressible two-dimensional vortex transition toy model known as the double gyre. Here, a single gyre pattern transitions to a double gyre pattern without any splitting process, which is in contrast to the setting that was studied in the previous paragraphs. The velocity field for the system under

consideration is given by

$$V(x,t) = (-\frac{\partial \Psi}{\partial y}, \frac{\partial \Psi}{\partial x})$$

with

$$\Psi(x,y,p) = p\sin(2\pi x)\sin(\pi y) + (1-p)\sin(\pi x)\sin(\pi y).$$

being the parameter-dependent stream function with $p \in [0,\, 1]$. We obtain the two-dimensional ordinary differential equation

$$\begin{aligned} \dot{x}(t) &= -(1-p)\pi\sin(\pi x)\cos(\pi y) - \pi p\sin(2\pi x)\cos(\pi x) \\ \dot{y}(t) &= (1-p)\pi\cos(\pi x)\sin(\pi y) + 2\pi p\cos(2\pi x)\sin(\pi y) \end{aligned} \tag{5.18}$$

Note that the right hand side of (5.18) is a convex combination of two velocity fields. For $p = 0$, the dominant velocity field yields a single rotating vortex centred in the elliptic fixed point $(0, 0)$, obtaining the system (5.10) used earlier in section 5.3 and figure 5.5. For $p = 1$, we have the coexistence of two counter-rotating vortices. These two values of p correspond to the pre- and post-transition global dynamics of (5.18). The transition from a single rotating gyre to a rotating double gyre occurs for $p \in (0\,1)$, where the onset of the emergence of the second gyre right is observed at $p = 1/3$. What happens when $p \in (0,\, 1/3)$ is that the single vortex only moves to the left side of the domain $M = [0,\, 1] \times [0,\, 1]$, see figure 5.26, where we illustrate the changes of the velocity field of (5.18) with respect to p. Note that the motion of this single vortex to the left, before the transition, does not imply its expansion or shrinking.

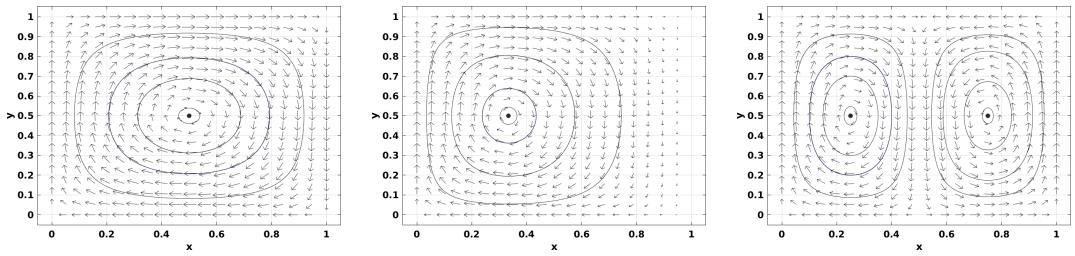

$p = 0$ $p = 1/3$ $p = 1$

Figure 5.26: Changes of the velocity field in system (5.18) for different p.

Again, we use GAIO to numerically simulate the set-oriented dynamics of (5.18) and find dominant patterns corresponding to the almost-invariant sets. For different values of p, the second and third dominant eigenvectors are shown in figure 5.27.

The corresponding eigenvalues are shown in figure 5.28. One clearly sees that the

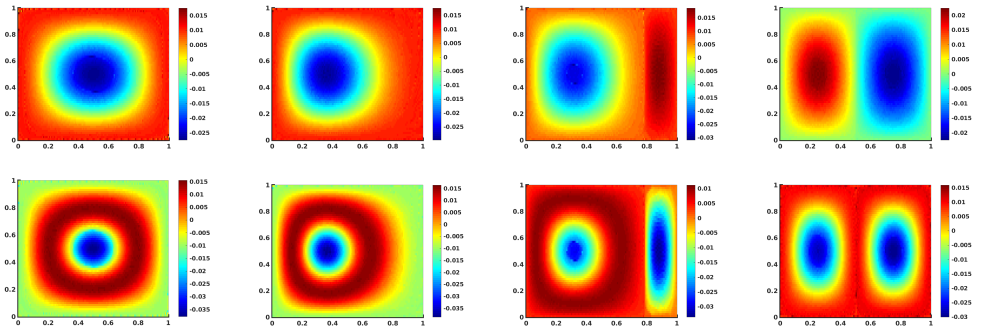

Figure 5.27: Changes of $U_2(\epsilon, p)$ (top) and $U_3(\epsilon, p)$ vs. p .

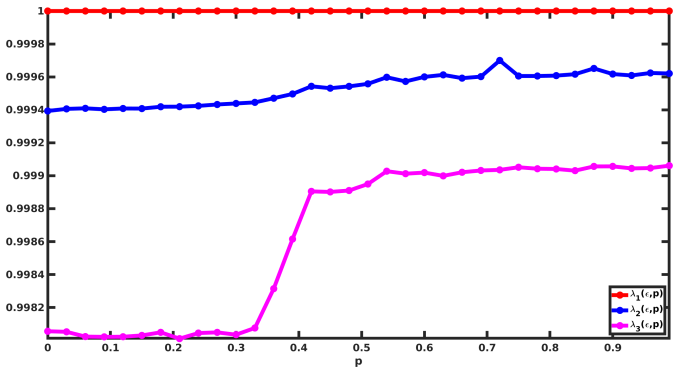

Figure 5.28: Spectral signature of the double gyre transition.

changes in the eigenvalues capture very well the behavior of the global dynamics. Indeed, for $p \in [0,\ 1/3]$ $\lambda_2(\epsilon, p)$ and $\lambda_3(\epsilon, p)$ remain constant, since the single vortex only moves to the left, without shrinking or expanding. That explains why the eigenvalues have not decreased. For $p \in (1/3,\ 1]$, the birth of the second vortex separates the global dynamics into two distinct flow patterns. That is, the corresponding transition matrix becomes nearly reducible and it follows that the eigenvalues $\lambda_2(\epsilon, p)$ and $\lambda_3(\epsilon, p)$ increase to become closer to 1. The rise of the eigenvalues $\lambda_2(\epsilon, p)$ and $\lambda_3(\epsilon, p)$ at $p > 1/3$ can be compared to the trends of $\lambda_1'(\epsilon, p)$ in figure 5.20.

This simple transition in the dynamics of (5.18) is clearly different from the critical transition caused by a splitting in the global dynamics of (5.13) as illustrated by figures 5.21 and 5.23. In particular, a decrease of dominant eigenvalues while another previously weak mode eigenvalue rises appears to be a spectral indicator of a splitting of almost-invariant patterns.

5.6 Summary

From a set-oriented approach, we studied bifurcations of particular almost-invariant patterns, which are supported in a neighborhood of an elliptic fixed point. These almost-invariant sets result from invariant sets when the underlying stationary dynamical system is diffusively perturbed. Near the splitting of patterns, generic indicators consist of a decrease of the dominant eigenvalues whose corresponding eigenvector patterns are in concern. In fact, the Duffing-type oscillator illustrates a cascade of splittings of the pattern supported in the neighborhood of the initially elliptic fixed point. The splitting occurs at the crossing between the dominant eigenvalues and a particular rising eigenvalue that initially belonged to the weak mode eigenvalues. It becomes the largest eigenvalue after the eigenvalue 1 and its corresponding eigenvector is supported on the dominant phase space pattern post-bifurcation.

Patterns emerging from complex dynamics of real- orld systems, such as the Antarctic polar vortex break up in late September 2002, suggest an analogous nonstationary framework. That is, in order to apply this set-oriented formulation of bifurcation analysis into real world applications, one may need to reconsider nonautonomous dynamical systems instead. Thus, inspired by the present study, the next chapter will address a characterization of finite-time bifurcations of coherent sets, which emerge from a nonautonomous dynamical system. This will allow us to deduce finite-time generic early warning signals for sudden vortex splittings. These results will be used to spectrally describe and characterize the Antarctic polar vortex splitting event from the recorded velocity data, see figure 1.1.

6 Early warning signs and critical transitions of coherent sets

This chapter is a nonautonomous extension of chapter 5. Nonautonomous dynamical systems are more relevant to model complex systems due to the explicit time parameter in the velocity field, as explained in chapter 2.
In the present chapter, we study the finite time bifurcation of coherent sets with the main goal of establishing a better understanding of early warning signals for sudden pattern splitting. The latter is motivated by the Antarctic polar vortex sudden break up in September 2002, as illustrated in figure 1.1. To this end, we study specific classes of nonautonomous systems who mimic the Antarctic polar vortex dynamics. To the best of our knowledge the bifurcation analysis of coherent sets as formulated in this chapter, has remained a widely unexplored topic. The previous chapter considers the bifurcation and splitting of almost-invariant sets, which are interpreted as dominant patterns in autonomous incompressible flows, see also [57]. There, almost-invariant sets are built around a global stationary state, whose bifurcation yields the qualitative change of the underlying flow patterns. The results of this chapter are currently being prepared for submission to Chaos [60].

6.1 Nonautonomous dynamics and coherent sets

In this work consider the time-dependent ODE (2.18) its corresponding nonautonomous flow map (2.19) which fulfills the cocycle property [58, 59]:
1. $\phi(t,t,x) = x$;
2. $\phi(t_2,t,x) = \phi(t_2,t_1,\phi(t_1,t,x)),\ \forall\ t,t_1,t_2 \in \mathbb{R}$ and $x \in \mathbb{R}^d$. In this chapter, we will study explicit nonautonomous flow maps generated by time-dependent ODEs.
Subsets M of the extended phase space $\mathbb{R}\times\mathbb{R}^d$ are referred to as nonautonomous sets and

the set $M(t) = \{x \in \mathbb{R}^d : \ (t, x) \in M\}$ is called the t-**fiber** of M. Thus, a nonautonomous set M is called invariant w.r.t. (2.18) if $\phi(t + \tau, t, M(t)) = M(t + \tau)$ for all $t, \tau \in \mathbb{R}$. Moreover, M is closed, compact or linear if all t-fibers are closed, compact or linear.

We are interested in the finite time evolution of macroscopic objects. Thus, we restrict the time domain to an interval of finite length $\mathbb{I} \subset \mathbb{R}$ and the space domain at initial time t is restricted to a compact manifold $X_t \subset \mathbb{R}^d$. We set $Y_{t+\tau} = \phi(t + \tau, t, X_t) \subseteq \mathbb{R}^d$ to be the image state space at final time $t + \tau$. The backward process is denoted by $\phi(t, t + \tau, y) = x$, for $y \in Y_{t+\tau}$ and $x \in X_t$. Notably, such evolved subsets correspond to compact and invariant nonautonomous sets in the extended phase space $\mathbb{I} \times \mathbb{R}^d$.

6.1.1 Multiple coherent sets

In this work, we focus on the changes of phase space regions that are minimally dispersive or maximally coherent over finite time intervals. We introduce the probability measure space (X_t, Σ_t, μ_t) where Σ_t denotes the Borel-σ algebra and μ_t is interpreted as the initial mass distribution of the quantity we are tracking with respect to the underlying dynamics. Examples include the advective dynamics describing the horizontal distribution of mass such ozone concentration within the stratosphere or the concentration of salt in the ocean water.

The measure μ_t is transformed, via the flow map ϕ, to a final measure $\nu_{t+\tau}$, which is supported on the corresponding measure space $(Y_{t+\tau}, \Sigma_{t+\tau}, \nu_{t+\tau})$. This means $\nu_{t+\tau}(A) = \mu_t \circ \phi(t, t + \tau, A), \ \forall \ A \in \Sigma_{t+\tau}$. The measure $\nu_{t+\tau}$ represents the mass distribution of objects of interest at time $t + \tau$. Both measures are absolutely continuous with respect to Lebesgue measure ℓ.

Let t be the initial time, τ be the flow time and X_t the initial domain. The notion of coherent set was already introduced in chapter 2 for a single pair of measurable sets. $\{A_t^1, A_t^2, ..., A_t^k\} \subset X_t$ and $\{A_{t+\tau}^1, A_{t+\tau}^2, ..., A_{t+\tau}^k\} \subset Y_{t+\tau}$ form one-to-one pairs of coherent sets if $\mu_t(A_t^i) = \nu_{t+\tau}(A_{t+\tau}^i)$ and $A_{t+\tau}^i \approx \phi(t + \tau, t, A_t^i), \ i = 1, 2, ..., k$. More precisely, the coherence ratio of two measurable sets $(A_t^i, A_{t+\tau}^i)$ is defined as[15]

$$r(A_t^i, A_{t+\tau}^i) = \frac{\mu_t(A_t^i \cap \phi(t, t + \tau, A_{t+\tau}^i))}{\mu_t(A_t^i)}, \ i = 1, 2, \ldots, k. \tag{6.1}$$

Then $(A_t^i, A_{t+\tau}^i)$ is a pair of coherent sets, whenever

$$r(A_t^i, A_{t+\tau}^i) \approx 1 \text{ and } \mu_t(A_t^i) = \nu_{t+\tau}(A_{t+\tau}^i). \tag{6.2}$$

Moreover, (6.1) is interpreted as the conditional probability of a point initially in $A_t^i \subset X_t$ to be mapped forward into $A_{t+\tau}^i \subset Y_{t+\tau}$ at time $t+\tau$. In this work, we suppose that $\{A_t^1, A_t^2, ..., A_t^k\} \subset X_t$ and $\{A_{t+\tau}^1, A_{t+\tau}^2, ..., A_{t+\tau}^k\} \subset Y_{t+\tau}$ are disjoint partitions of X_t and $Y_{t+\tau}$, respectively.

Recall that the main purpose of this work is to find early warning signals for finite time bifurcations [58] of coherent sets [15] in the sense of splitting. For setting up the theory, which should cover realistic scenarios, we are primarily seeking sets that have the following properties:

1. Coherent sets that are robust under external perturbations.

2. Coherent sets that are supported in a neighborhood of a critical point or orbit (i.e. one that changes its stability type). This hypothesis is crucial for setting up the coherent set analogue of a finite time bifurcation as introduced in [58].

3. In conservative flows, the surface to volume ratio of coherent sets is minimal.

6.1.2 Coherent sets-oriented numerical framework

From now on, we work with discrete phase spaces. That is, the following study will be based on finite time transition probabilities between macroscopic states instead of the finite time evolution of single trajectories. In fact, eventually computed transition matrices are just finite dimensional approximations of time-dependent transfer operators defined in chapter 3. We subdivide X_t and $Y_{t+\tau}$ into finite state spaces $\mathcal{S}_t = \left\{B_1, B_2, \ldots, B_m\right\}$ and $\mathcal{S}_{t+\tau} = \left\{C_1, C_2, \ldots, C_n\right\}$, respectively. The partition elements (boxes) satisfy $\ell(B_i) = \ell(B_j)\ i, j \leq m$ and $X_t = \cup_{j=1}^m B_j$ with $\ell(B_i \cap B_j) = 0$; the measure ℓ denotes the normalized Lebesgue measure on $\cup_{j=1}^m B_j$. The same applies to the boxes $C_j \subset Y_{t+\tau},\ j = 1, 2, \ldots, n$. We define the initial and final time lumped finite state spaces as [14]

$$\mathcal{B}_m = \left\{ A \subset X_t \,:\, A = \bigcup_{j \in \mathcal{I}} B_j,\ \mathcal{I} \subset \{1, 2, ..., m\} \right\} \tag{6.3}$$

and

$$\mathcal{C}_n = \left\{ A \subset Y_{t+\tau} \,:\, A = \bigcup_{j\in\mathcal{J}} C_j,\ \mathcal{J} \subset \{1,2,...,n\} \right\} \tag{6.4}$$

respectively. Then, we construct the finite time transition matrix [15]

$$P_{ij}^{t,\tau} = \frac{\ell(B_i \cap \phi(t, t+\tau, C_j))}{\ell(B_i)}, \tag{6.5}$$

from the nonautonomous flow. $P^{t,\tau}$ is an m-by-n row stochastic matrix. Each entry $P_{ij}^{t,\tau}$ is the probability that a randomly chosen point in B_i at time t will be mapped forward to C_j at time $t+\tau$. The matrix (6.5) is actually an Ulam based finite rank approximation [22] of the Perron-Frobenius operator [15, 49] introduced in chapter 3, section 3.2.1. The numerical estimation of the entries in equation (6.5) is given by [15]

$$P_{ij}^{t,\tau} \approx \frac{\#\{x_k \in B_i :\ \phi(t+\tau, t, x_k) \in C_j\}}{N}, \tag{6.6}$$

which is the proportion of the uniformly distributed initial test points $\{x_k\}_{k=1}^N$ in box B_i at time t that are mapped to box C_j at time $t+\tau$. The computation of the transition matrix is implemented in the MATLAB-based software package GAIO[37].

6.2 Singular vectors and coherent partitions

In this section, we are interested in finding coherent partitions from (6.5). In other words, from the transition matrix $P := P^{t,\tau}$, we wish to approximate coherent sets, whenever they exist. Let us define an initial probability distribution $p > 0$ as $p_i = \mu_t(B_i)$, $i = 1, 2, \ldots, m$; p is the probability vector that approximates the initial distribution μ_t of mass being tracked over a finite time interval. The probability vector $q = pP$ is positive and represents the distribution of mass at final time $t+\tau$. With these approximations, we say that $\{A_t^1, A_t^2, \ldots, A_t^k\} \subset \mathcal{B}_m$ and $\{A_{t+\tau}^1, A_{t+\tau}^2, \ldots, A_{t+\tau}^k\} \subset \mathcal{C}_n$ form one-to-one pairs of coherent sets over the finite time interval $[t,\, t+\tau]$, if the following relations are satisfied: There exists index partitions $\{\mathcal{I}_1, \mathcal{I}_2, \ldots, \mathcal{I}_k\} \subset \{1, 2, \ldots, m\}$ with $A_t^i = \cup_{j\in\mathcal{I}_i} B_j$

and $\{\mathcal{J}_1, \mathcal{J}_2, \ldots, \mathcal{J}_k\} \subset \{1, 2, \ldots, n\}$ with $A^i_{t+\tau} = \cup_{j\in\mathcal{J}_i} C_j$ such that

$$\begin{aligned} \mu_t(A^i_t) &= \sum_{j\in\mathcal{I}_i} p_j \approx \nu_{t+\tau}(A^i_{t+\tau}) = \sum_{j\in\mathcal{J}_i} q_j \ \text{ and} \\ r(A^i_t, A^i_{t+\tau}) &= \frac{\sum_{l\in\mathcal{I}_i, r\in\mathcal{J}_i} p_l P_{lr}}{\sum_{l\in\mathcal{I}_i} p_l} \approx 1, \ i = 1, 2, \ldots, k, \ k \geq 2. \end{aligned} \tag{6.7}$$

In order to numerically approximate coherent sets we seek particular vectors built around the transition matrix P. This requires a reformulation of (6.5) in terms of separate initial and final time transition matrices. In the following, we assume there are $k \geq 2$ pairs of coherent sets that partition $\mathcal{B}_m$ and $\mathcal{C}_n$, respectively. From P, let us define the transition matrix

$$L_{ij} = \frac{p_i P_{ij}}{q_j}, \ i = 1, ..., m, \ \ j = 1, ..., n. \tag{6.8}$$

The matrix L is simply the normalization of P and – as P itself – depends both on the initial time t and the flow time τ. It represents the transition matrix of the macroscopic dynamics with respect to the initial and final mass distributions p and q. Note that, p and q are assumed to be positive and L satisfies $\mathbf{1}L = \mathbf{1}$ [16]. Now we introduce the inner products $\langle x, y\rangle_p = \sum_{i=1}^m x_i y_i p_i$ in $\mathbb{R}^m$ and $\langle x, y\rangle_q = \sum_{i=1}^n x_i y_i q_i$ in $\mathbb{R}^n$. Two vectors x and y are said to be p-orthogonal resp. q-orthogonal if $\langle x, y\rangle_p = 0$ resp. $\langle x, y\rangle_q = 0$. The matrix L may be roughly interpreted as the forward time transition matrix between the Hilbert space $\left(\mathbb{R}^m, \langle\cdot,\cdot\rangle_p\right)$ to the Hilbert space $\left(\mathbb{R}^n, \langle\cdot,\cdot\rangle_q\right)$. That is, any uniformly distributed density p on $\left(\mathbb{R}^m, \langle\cdot,\cdot\rangle_p\right)$ is mapped by L to a uniform density q on $\left(\mathbb{R}^n, \langle\cdot,\cdot\rangle_q\right)$. Let L^* denote the dual of L with respect to the defined inner products. Then $\langle xL, y\rangle_q = \langle x, yL^*\rangle_p$ and it is straightforward to show that

$$L^* = P^\intercal. \tag{6.9}$$

Thus, L^* represents the n-by-m backward time transition matrix. Equation (6.8) and (6.9) are actually a finite dimensional approximations of the transfer operator (3.13) and its adjoint, respectively. It follows that $Q^t := LL^*$ is an m-by-m column stochastic matrix defined on the finite state space $\left(\mathbb{R}^m, \langle\cdot,\cdot\rangle_p\right)$ at initial time t. It can also be interpreted as the forward-backward time transition matrix at time t in the sense that any probability distribution in $\left(\mathbb{R}^m, \langle\cdot,\cdot\rangle_p\right)$ is mapped forward with L then mapped backward using L^*. On the other hand, $Q^{t+\tau} := L^*L$ is an n-by-n column stochastic matrix defined on

$\left(\mathbb{R}^n, \langle\cdot,\cdot\rangle_q\right)$. Likewise, L^*L is the backward-forward time transition matrix describing the macroscopic behavior of the dynamics at time $t+\tau$. It is easy to show that both Q^t and $Q^{t+\tau}$ are positive definite self-adjoint matrices. With this construction, a coherent pair $(A_t^i, A_{t+\tau}^i)$ can be functionally characterized by $\mathbf{1}_{A_t^i} Q^t \approx \mathbf{1}_{A_t^i}$ and $\mathbf{1}_{A_{t+\tau}^i} Q^{t+\tau} \approx \mathbf{1}_{A_{t+\tau}^i}$, i.e. coherent sets remain almost invariant under the forward-backward and backward-forward dynamics [36].

As introduced in [15, 16, 36] coherent sets are approximated by signed vectors, which are eigenvectors of Q^t and $Q^{t+\tau}$ to eigenvalues close to one. These can be also viewed as the singular vectors obtained from SVD of L in (6.8), taking into account the weighted inner product structures. The corresponding SVD of L (see [15, 16] for the exact construction) yields the singular values

$$\sigma_l := (\lambda_l)^{1/2},\ l = 1, 2, \ldots, \min(m, n). \tag{6.10}$$

where the λ_l's are the eigenvalues of both Q^t and $Q^{t+\tau}$. These are obtained from the so-called minimax principles applied to Q^t or $Q^{t+\tau}$ see (Theorem 9.2.4, p212, [62] and [15, 16]). Let $\{u_l,\ l = 1, 2, \ldots, \min(m, n)\}$ such that $\lambda_l u_l = u_l Q^t$ and $\{v_l,\ l = 1, 2, \ldots, \min(m, n)\}$ such that $\lambda_l v_l = v_l Q^{t+\tau}$ are the corresponding eigenvectors of Q^t and $Q^{t+\tau}$, respectively. In the language of SVD, the u_l's are the left singular vectors of L, while the v_l's are the right singular vectors. Moreover, both left and right singular vectors are orthogonal with respect to $\langle\cdot,\cdot\rangle_p$ and $\langle\cdot,\cdot\rangle_q$, respectively and

$$\sigma_l v_l = u_l L. \tag{6.11}$$

Since Q^t and $Q^{t+\tau}$ are both stochastic matrices, we have $\sigma_1 = 1$, $u_1 = \mathbf{1}$ and $v_1 = \mathbf{1}$. As a consequence of the orthogonality relation $\langle u_1, u_2\rangle_p = \langle v_1, v_2\rangle_q = 0$, the sign patterns of the second left and right singular vectors are

$$\text{sgn}(u_2) = (+, +, +, +, \ldots, +, -, -, -, -, \ldots, -)$$

$$\text{sgn}(v_2) = (+, +, +, +, \ldots, +, -, -, -, -, \ldots, -),$$

after a convenient reordering of the entries. Thus, positive and negative level sets of u_2 and v_2 partition $\mathcal{B}_m$ and $\mathcal{C}_n$, respectively. In other words, $\mathcal{B}_m$ can be subdivided into two sets that are the support of the positive and negative sign of u_2, respectively. The same holds for $\mathcal{C}_n$ with v_2. We can then pick $(A_t^1, A_{t+\tau}^1) = (\operatorname{supp} u_2^+, \operatorname{supp} v_2^+)$ as the positive

level sets of u_2, v_2 and $(A_t^2, A_{t+\tau}^2) = (\operatorname{supp} u_2^-, \operatorname{supp} v_2^-)$ as the negative level sets. Let us suppose that $\sigma_2 = 1$ in (6.11), then from the above construction it immediately follows that $\phi(t+\tau, t, A_t^1) = A_{t+\tau}^1$ and $\phi(t+\tau, t, A_t^2) = A_{t+\tau}^2$. In particular, any choice of (A_t^1, A_t^2) with their images $(A_{t+\tau}^1 = \phi(t+\tau, t, A_t^1), A_{t+\tau}^2 = \phi(t+\tau, t, A_t^2))$ would define perfectly coherent sets and thus the problem of finding coherent pairs turns out to be ill-posed. However, we are interested in coherent sets that are robust with respect to perturbations. While including diffusion regularizes the mathematical problem of finding optimal sets [16], it also makes the setting better applicable to real-world systems with are naturally influenced by noise.

6.3 Robust coherent sets under perturbations

In this section, we discuss the structure and spectral properties of the self-adjoint stochastic matrices $Q^t = LL^*$ obtained from the discretization of the transfer operators and relate them to coherent behavior of the underlying system. In particular, we address the situation of perfectly coherent sets and the influence of small random perturbations.

6.3.1 Perfectly coherent sets

We suppose, with respect to the underlying dynamics, the existence of k pairs of disjoint coherent sets that partition the discrete state spaces $\mathcal{B}_m$ and $\mathcal{C}_n$, respectively. That is, there exist families of sets $\{A_t^1, A_t^2, \ldots, A_t^k\} \subset \mathcal{B}_m$ and $\{A_{t+\tau}^1, A_{t+\tau}^2, \ldots, A_{t+\tau}^k\} \subset \mathcal{C}_n$ that satisfy (6.7). In particular, we primarily impose the relation $r(A_t^i, A_{t+\tau}^i) = 1$, i.e. the considered pairs of sets are perfectly coherent. A convenient reordering of the transition probabilities between initial and final states (B_i, C_j), where $B_i \in \mathcal{B}_m$, $i = 1, \ldots, m$, and $C_j \in \mathcal{C}_n$, $j = 1, \ldots, n$, yields a block-diagonal self-adjoint matrix $Q^t = LL^*$ with a k-level partition

$$Q^t = \begin{pmatrix} Q_1^t & 0 & \cdots & 0 \\ 0 & Q_2^t & \cdots & 0 \\ \vdots & \vdots & \ddots & \vdots \\ 0 & 0 & \cdots & Q_k^t \end{pmatrix}, \quad k > 2. \tag{6.12}$$

Each Q_i^t is an m_i-by-m_i irreducible row stochastic matrix over the aggregates states A_t^i and $\sum_{i=1}^k m_i = m$. We define the forward-backward time conditional transition probabilities between the initial time coherent sets $\{A_t^i,\ i = 1, 2, \ldots, k\}$ as $w\Big(A_t^i, A_t^j\Big) = \frac{\sum_{i\in I, j\in J} \pi_i Q_{ij}^t}{\sum_{i\in I} \pi_i}$.

Under the forward-backward time dynamics, the system will always stay in the state A_t^i in which it was initialized. In this case, $w\Big(A_t^i, A_t^j\Big)$ is simply the Kronecker symbol $\delta_{ij},\ j = 1, \ldots, k$, since the initial time coherent sets are isolated disjoint aggregates. In particular, there is zero transition probability between any two distinct aggregates (A_t^i, A_t^j), $i \neq j$.
Given (6.12), $\lambda_1 = 1$ is an eigenvalue of Q^t with algebraic multiplicity k. Thus Q^t has k left eigenvectors $u_i = u_i Q^t$ such that

$$u_i = (0, 0, \ldots, \mathbf{1}_i, 0, \ldots, 0),\ i = 1, 2, \ldots, k \tag{6.13}$$

with $\mathbf{1}_i = \mathbf{1}_i Q_i^t$. In this way, every left eigenvector u_i, which is also the left singular vector of L as stated previously, may be interpreted as a characteristic function of the aggregate A_t^i. Hence, due to (6.10), the singular value $\sigma_1 = 1$ is also k-fold and the right singular vector $v_i = u_i L$ may be interpreted as a characteristic function of $A_{t+\tau}^i$, for $i = 1, 2, \ldots, k$.

Let $E_{\lambda_1} = \text{span}\{u_1, u_2, \ldots, u_k\}$ be the eigenspace spanned by (6.13). Then, there exists another basis $\{U_i,\ i = 1, \ldots, k\}$ of E_{λ_1} such that every basis element is an eigenvector of Q^t with eigenvalue 1 and is given by a linear combination of the $u_i,\ i = 1, 2, \ldots, k$. That is,

$$\begin{aligned} U_i &= \sum_{j=1}^{k} \alpha_{ij} u_j,\ i = 1, \ldots, k,\ \alpha_{ij} \in \mathbb{R} \\ &= (\alpha_{i1}, \alpha_{i1}, \ldots, \alpha_{i1}, \alpha_{i2}, \alpha_{i2}, \ldots, \alpha_{i2}, \ldots, \alpha_{ik}, \alpha_{ik}, \ldots, \alpha_{ik}). \end{aligned} \tag{6.14}$$

Thus, depending on the signs of the α_{ij}, each U_i partitions the aggregates $\{A_t^i\}_{i=1}^k$ into unions of aggregates or "clouds". Likewise,

$$V_i = \sum_{j=1}^{k} \beta_{ij} v_j = \sum_{j=1}^{k} \beta_{ij} u_j L,\ i = 1, \ldots, k,\ \beta_{ij} \in \mathbb{R}. \tag{6.15}$$

are the corresponding right singular vectors and yield a partition consisting of the final time coherent sets $\{A_{t+\tau}^i,\ i = 1, 2, ..., k\}$ via the sign structures of the vector entries. From this simplified setting, it is clear that under the described finite time dynamics, the sign patterns of the left singular vectors in (6.14) and the sign patterns of the right singular vectors in (6.15) yield, each, a partition of the discretized initial and final time state spaces into union of aggregates or coherent sets. The construction of those aggregates from singular vectors sign patterns is similar to construction of almost-invariant aggregates in

chapter 5.

6.3.2 Robust coherent sets

Robustness of the coherent sets is provoked by adding small random perturbations into the finite time dynamics. Perturbations can be thought of as "shaking" their initial and final time state spaces, which are now partitioned by the present, unperturbed coherent sets. Under the perturbation influence, we suppose that the self-adjoint transition matrix in (6.12) becomes

$$Q^t(\epsilon) = \begin{pmatrix} Q_1^t(\epsilon) & E_{12} & \cdots & E_{1k} \\ E_{21} & Q_2^t(\epsilon) & \cdots & E_{2k} \\ \vdots & \vdots & \ddots & \vdots \\ E_{k1} & E_{k2} & \cdots & Q_k^t(\epsilon) \end{pmatrix}, \quad k > 2, \tag{6.16}$$

where $\epsilon \in \mathbb{R}$ is the perturbation amplitude. We suppose that the latter is such that $Q^t(\epsilon)$ becomes an irreducible row stochastic matrix. Thus, $Q^t(\epsilon)$ has a unique stationary distribution $\pi(\epsilon)$.

Let us first suppose that all the unperturbed coherent sets are robust under perturbations. This implies $w\Big(A_t^i, A_t^j\Big) = \frac{\sum_{i\in I, j\in J}\pi_i Q_{ij}^t(\epsilon)}{\sum_{i\in I}\pi_i} \approx \delta_{ij}$, which means that mass may leave a coherent set to enter another coherent set with very low probability due to the perturbation effect. Additionally the off-diagonal matrices $E_{ij},\ i,j = 1,2,\ldots,k$ are very small in magnitude relative to 1, i.e.,
$\|E_{ij}\|_\infty = \max_l \sum_m e_{lm}^{ij} \ll 1$. The matrices $Q_i^t(\epsilon),\ i = 1,...,k$ are then nearly stochastic. Therefore, we have the following spectral properties of $Q^t(\epsilon)$ [34, 35]:

(a) The Perron root $\lambda_1(\epsilon) = 1$,

(b) the set of $k-1$ non-unit eigenvalues $\{\lambda_2(\epsilon) \leq \ldots \leq \lambda_k(\epsilon)\}$, which are clustered near 1,

(c) the remaining set of $N-k$ eigenvalues which are bounded away from 1, for small ϵ.

Thus, under the perturbation effect we have a set $\{\sigma_2(\epsilon), \ldots, \sigma_k^t(\epsilon)\}$ of k singular values clustered near the singular value $\sigma_1(\epsilon) = 1$. The corresponding p-orthogonal left singular

vectors $\{U_j(\epsilon)\}_{j=1}^k$ satisfy

$$\sigma_j(\epsilon)V_j(\epsilon) = U_j(\epsilon)L(\epsilon). \tag{6.17}$$

$\{V_j(\epsilon)\}_{j=1}^k$ are the corresponding q-orthogonal right singular vectors. These perturbed vectors can be estimated from the unperturbed ones[35, 57]. Note that $U_1(\epsilon) = \mathbf{1} = (1, 1, ..., 1)$ and $V_1(\epsilon) = \mathbf{1} = (1, 1, ..., 1)$. A particular example includes $(1, \sigma_2(\epsilon))$ where, due to orthogonality, we have

$$\text{sgn}(U_2(\epsilon)) = (+, +, +, +, \ldots, +, - - --, \ldots, -)$$

$$\text{sgn}(V_2(\epsilon)) = (+, +, +, +, \ldots, +, - - --, \ldots, -).$$

It follows that relation (6.17) with $l = 2$ yields an approximation of the two largest aggregates which partition each state space into two coherent sets.

Indeed, in most practical problems, it is enough to study the second dominant singular value and the corresponding singular vectors. In [16, 36], ϵ was explicitly modeled and only $\sigma_2(\epsilon)$ and $(U_2(\epsilon), V_2(\epsilon))$ were used for one time interval with the purpose of illustrating how singular vectors can approximate coherent sets. The sign structure of the second dominant left and right singular vectors are the first patterns to investigate for finding coherent patterns, whenever $\sigma_2(\epsilon) \approx 1$.

However, in this work, we need all the $k - 1$ singular vectors, because we investigate critical transitions of patterns supported on local critical solutions, which undergo finite time local bifurcations. Besides, due to the clustering of the $k - 1$ singular values near 1, all the $k - 1$ singular vectors yield coherent partitions of the state spaces. We will use them individually and focus on those singular vectors which are supported on the critical objects of interest.

6.4 Bifurcations of coherent sets and early warning signals

In this section, we study different example systems in order to develop a better understanding of the spectral footprints of coherent sets bifurcations.

6.4.1 Spectral analysis of a finite time bifurcation in 1D

We start the finite time bifurcation analysis of coherent sets with the one-dimensional ordinary differential equation

$$\begin{aligned}\dot{x} &= \arctan(t)x - x^3,\ (t,x) \in [-20,\, 20] \times [-2,\, 2],\\ &= x\Big(\arctan(t) - x^2\Big),\end{aligned} \tag{6.18}$$

which is a nonautonomous version of the supercritical pitchfork bifurcation normal form (see e.g., ref.[10], Chapter 3, p. 146). Its finite time dynamics is relatively simple to grasp. However, in this study, a set-oriented approach to analyze (6.18), is crucial for understanding the changes in the trends of the singular values with respect to the changes of the corresponding singular vectors pattern generated by the finite time dynamics. In particular, we experiment spectral analogues of notions such as finite time **expansion** and finite time **contraction** of coherent sets. For all $t \in [-20,\, 20]$, the right hand side vanishes for $x = 0$. For $t \leq 0$, it also vanishes for $x = \pm w(t)$ where

$$w(t) = \sqrt{\arctan(t)}.$$

We consider the nonautonomous set $M = \{(t, 0),\ t \in [-20,\, 20]\}$, which is invariant w.r.t. to (6.18). Thus, every t-fiber consists of the singleton $\{0\}$. The set M is finite time attractive[58], whenever $t \leq 0$, and finite time repulsive for $t > 0$. The supercritical **finite time pitchfork bifurcation** occurs when the dynamics of the critical solution shifts from the finite time attractive regime to the finite time repulsive regime, with the birth of two finite time attractive solutions $\{\pm w(t),\ t \geq 0\}$.

Our spectral analysis of (6.18) is realized using a set-valued approach. For this, we define the following interval-valued mapping

$$x \in [-2,\, 2] \mapsto [\phi(t+\tau, t, x) - \sigma,\, \phi(t+\tau, t, x) + \sigma] \subset [-2,\, 2], \tag{6.19}$$

where $\sigma > 0$. The trivial solution $\{0\}$ then becomes an interval-valued trivial solution $[\{0\} - \sigma,\, \{0\} + \sigma]$, which allows us to look at it as a pattern within a set-oriented analysis. A set-oriented finite time bifurcation is characterized from the spectral data obtained from approximated transition matrices defined in (6.8).

The numerical computation settings are as follows. We subdivide the domain $[-2,\, 2]$ into 2^8 disjoint sub-intervals $D_i,\ i = 1, \ldots, 2^8$ of equal length, which implicitly determines the

numerical perturbation parameter ϵ. The image of each D_i is discretized by 48 test points. We choose $\sigma = 0.4$ and represent $[-0.4,\, 0.4]$ by 5150 uniformly distributed random points. The time domain is subdivided into sub-intervals of length 1, i.e., $[-20,\, 20] = \bigcup_{t=-20}^{19} [t,\, t+1]$. The system is numerically integrated within every time interval $[t,\, t+1]$, $t = -20, \ldots, 19$ using a 4th order Runge-Kutta scheme and the corresponding transition matrices and SVDs are computed. This is referred to as the **sliding window approach**.

The first three dominant singular values with respect to each time interval $[t, t+1]$ with $t = -20, -19, \ldots, 19$ are shown in figure 6.1, where we observe a remarkable rise of the second and third singular values when approaching and passing the bifurcation point. We will come back to this later. The changes in the global dynamics are visible in the

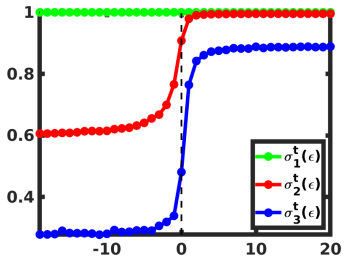

Figure 6.1: First three dominant singular values (depending of t) for different time windows $[t,\, t+1]$, $t = -20, -19, \ldots, 19$, with $t+1$ in the x-axis.

structure of the transition matrices L in figure 6.2 (a)-(c) and figure 6.3 (a)-(c). Note that the $x-$axes correspond to the reachable states at $t+\tau$, while the $y-$axes correspond to the initial state spaces at time t. For $t+\tau < 0$ the final state space is only a small subset of the initial state space as consequence of the **contraction** induced by the presence of the global attractor $\{0\}$. Indeed, subintervals C_j that are not part of the image of $[-2, 2]$ are simply removed during the computation.

In particular, the finite time global behavior of the dynamics for $t + \tau < 0$, without applying the interval-valued perturbation $[-0.4,\, 0.4]$, may be illustrated in terms of subinterval-wise transition probabilities as

$$\left\{B_1, B_2, ..., B_{\frac{m}{2}}\right\} \mapsto \left\{C_{n_1}, C_{n_2}\right\} \text{ and } \left\{B_{\frac{m}{2}+1}, B_{\frac{m}{2}+2}, ..., B_m\right\} \mapsto \left\{C_{n_3}, C_{n_4}\right\}, \quad (6.20)$$

where $C_{n_1} \cup C_{n_2} \cup C_{n_3} \cup C_{n_4}$ is the discretized neighborhood of the $t-$fiber $\{0\}$. To the left of $\{0\}$ are the subintervals $\left\{B_1, B_2, ..., B_{\frac{m}{2}}\right\}$ which are mapped to $C_{n_1} \cup C_{n_2}$, whereas to the right of $\{0\}$ are the subintervals $\left\{B_{\frac{m}{2}+1}, B_{\frac{m}{2}+2}, ..., B_m\right\}$ which are mapped to $C_{n_3} \cup C_{n_4}$. In this way, the mapping (6.20) shows the global behavior of (6.18) for

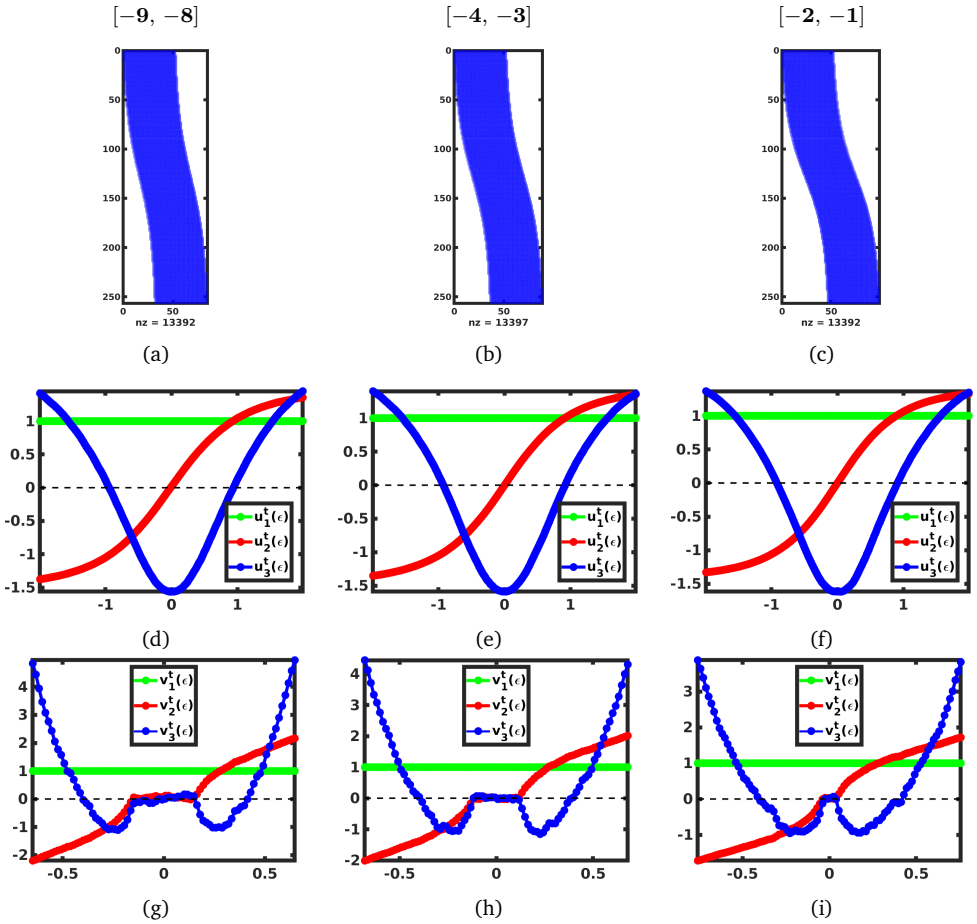

Figure 6.2: Changes of the transition matrices (6.8), dominant left and right singular vectors before the finite time bifurcation.

$t + \tau \leq 0$. Due to the convergence of all initial points to the trivial attractor, there are no coherent sets. As detailed in section 6.3, the magnitude of the singular values with respect to 1 determines the presence of coherent sets partitioning of the state space. Thus, given the singular values magnitude in figure 6.1, there are no coherent sets for $t + \tau < 0$, as the singular values are far from 1. The corresponding left and right singular vectors for $t + \tau < 0$ are shown in figure 6.2 (d)-(f) and (g)-(i), respectively. Moreover, using the left and right singular vectors $u_2^t(\epsilon)$ and $v_2^t(\epsilon)$ of $\sigma_2^t(\epsilon)$, we can numerically approximate the coherence ratio (6.1). This is plotted in figure 6.4 for different time intervals. Indeed, one observes fluctuations of the coherence ratios with a maximum magnitude less than 0.9, for different time windows with $t + \tau < 0$. As a consequence, the second condition of equation (6.7) is not fulfilled in this regime, which means there are no coherent sets.

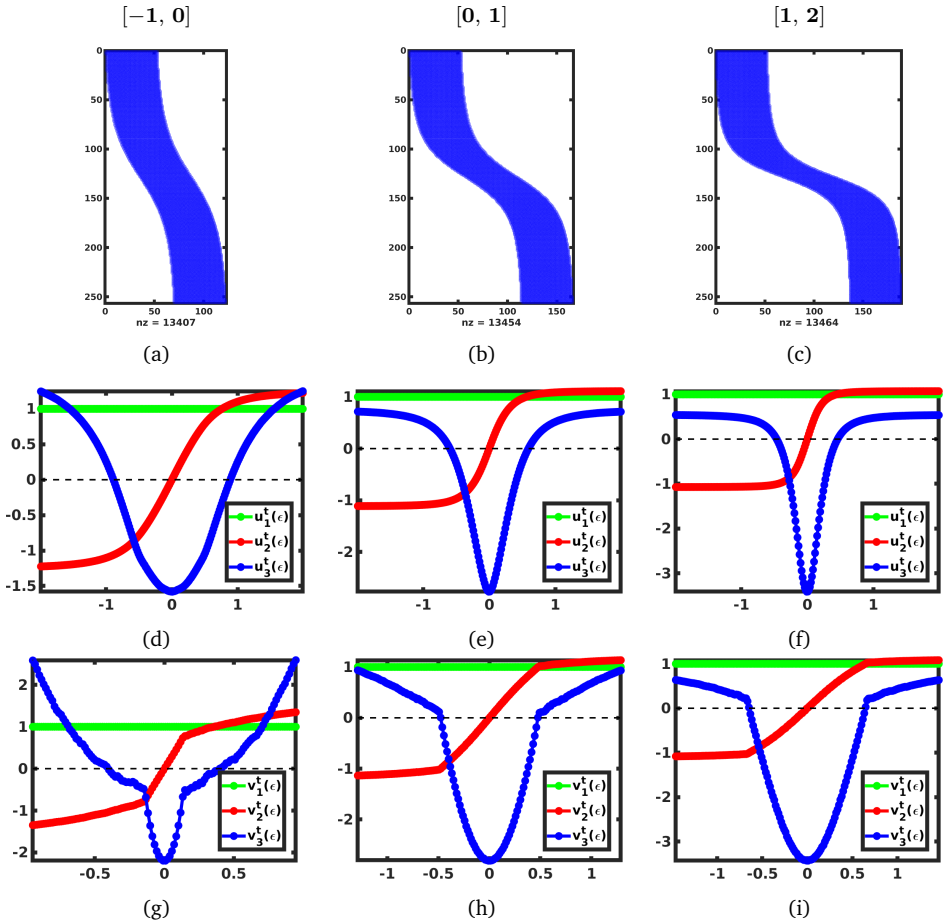

Figure 6.3: Changes of the transition matrices (6.8), dominant left and right singular vectors near and after the finite time bifurcation.

Let $\{x_{t,i}\}_{i=1}^{N}$ denote the initial test points (used for estimating the transition matrix) at time t and $\{x_{t+\tau,i}\}_{i=1}^{N}$ the image test points at time $t+\tau$ under the deterministic flow map (**??**) of (6.18). Thus, for $t+\tau<0$, we have that $\{x_{t+\tau,i}\}_{i=1}^{N}$ are accumulated near $x=0$, from both negative and positive sides. Before applying the set-valued transformation (6.19), let us subdivide the image test points into negative set of data $\{x_{t+\tau,i}^{(-)}\}_{i=1}^{N_1}$ and positive set of data $\{x_{t+\tau,i}^{(+)}\}_{i=1}^{N_2}$ with $N_1+N_2=N$. Now, we apply the set-valued mapping (6.19) to obtain $\{x_{t+\tau,i}^{(-)}\}_{i=1}^{N_1}+[-0.4,\,0.4]=\mathcal{S}_{-}^{(-)}\cup\mathcal{S}_{+}^{(-)}$ and $\{x_{t+\tau,i}^{(+)}\}_{i=1}^{N_2}+[-0.4,\,0.4]=\mathcal{S}_{-}^{(+)}\cup\mathcal{S}_{+}^{(+)}$. Here $\mathcal{S}_{-}^{(-)}$ and $\mathcal{S}_{+}^{(-)}$ denote, the new negative and positive data obtained from the former negative data points $\{x_{t+\tau,i}^{(-)}\}_{i=1}^{N_1}$, respectively; analogously for the positive data points $\{x_{t+\tau,i}^{(+)}\}_{i=1}^{N_2}$. The test points $\{x_{t+\tau,i}\}_{i=1}^{N}+[-0.4,\,0.4]$ are, thus, distributed in the state space according to two classes of data $\left\{\mathcal{S}_{-}^{(-)},\mathcal{S}_{-}^{(+)}\right\}$ and $\left\{\mathcal{S}_{+}^{(-)},\mathcal{S}_{+}^{(+)}\right\}$. For $t+\tau<0$, this is, in fact, a bimodal distribution, separated by a **critical region** around

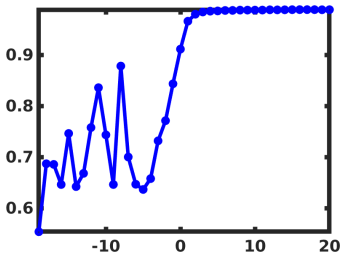

Figure 6.4: Coherence ratios (6.1) (depending on t) for different time windows $[t,\, t+1]$, $t = -20, -19, \ldots, 19$, with $t+1$ in the x-axis.

the attractor $\{0\}$, which is a result of the set-valued mapping.

The size of this critical region will be a crucial indicator for tracking the qualitative change of the attractor from the singular vectors patterns, as we slide the time window $[t,\, t+\tau]$ towards zero. The result of transforming deterministic image data into classes via (6.19) is captured through the second and third right dominant singular vectors $v_i^t(\epsilon)$, $i = 2, 3$. Indeed, the second right singular vector $v_2^t(\epsilon)$ yields very negative entries left of the critical region, very positive entries right of the critical region and almost zero entries in the critical region; see figure 6.2 (g)-(i).

On the other hand, $v_3^t(\epsilon)$ provides a more detailed classification with two wells holding the majority of the points in $\mathcal{S}_-^{(+)}$ and $\mathcal{S}_+^{(-)}$ each with negative entries, very positive entries holding separately the majority of the points in $\mathcal{S}_-^{(-)}$ and $\mathcal{S}_+^{(+)}$, and almost zero entries in the critical region; see figure 6.2 (g)-(i). In figure 6.2 (d)-(f) and (g)-(i), one notices that, despite the contraction of the support of $v_i^t(\epsilon)$, $i = 1, 2, 3$, the second and third left and right singular vectors curves are similar in shape everywhere but in the critical region, which is the spectral response following the addition of the set-valued transformation (6.19). Moreover, it is a graphical illustration of the absence of coherent partitions for $t + \tau < 0$. Note that, as shown in figure 6.2 (g), the widest critical region exists for $t + \tau \ll 0$, where the attractor is the strongest.

The singular values in figure 6.1, the coherence ratios in figure 6.4, and the critical region highlighted by the right singular vector **patterns** in figure 6.2 (g)-(i) are simultaneously used as observables for identifying early signals prior to the finite time bifurcation of (6.18).

As $[t,\, t+\tau]$ slides towards 0, the critical region depicted by $v_2^t(\epsilon)$ and $v_3^t(\epsilon)$ starts to **shrink**. The attractor $\{0\}$, which is an asymptotic pullback attractor [59], loses more and more its finite time attractivity. As a result the distribution of image test points under

the set-valued mapping becomes increasingly unimodal. This due to the fact, that less deterministic image points can be found in the neighborhood of $\{0\}$ but are mapped to it by the subsequent set-valued perturbation (6.19). Hence, the closer the time interval slides to 0, the less **resilient** becomes the attractor $\{0\}$.

The singular values $\sigma_2^t(\epsilon)$ and $\sigma_3^t(\epsilon)$ do not vary for $[t,\, t+\tau]$ negative and far from zero, as shown in figure 6.1. This is an indicator of strong resilience of the attractor 0. The coherence ratios are not close to 1 for $[t,\, t+\tau]$ when $t+\tau \ll 0$, as shown in figure 6.4. However, as the time window $[t,\, t+\tau]$ approaches zero $\sigma_2^t(\epsilon)$ and $\sigma_3^t(\epsilon)$ increase slowly then faster near $t+\tau = 0$; see figure 6.1. The same is observed for the coherence ratios in figure 6.4. Indeed, the monotone rise of the coherence ratios indicates the ultimate presence of coherent patterns as the attractor begins to lose its resilience. The finite time bifurcation occurs when $t+\tau = 0$. The trivial solution $\{0\}$ becomes, hence, non-hyperbolic, and then repelling. As a consequence, one sees a **radical change** in the structure of the right singular vectors $v_{2,3}^t(\epsilon)$ in figure 6.3 (g)-(i) and left singular vectors $u_{2,3}^t(\epsilon)$ in figure 6.3 (d)-(f). This is particularly noticeable in the third singular vectors $v_3^t(\epsilon)$ and $u_3^t(\epsilon)$. Note the change of $v_3^t(\epsilon)$ in the neighborhood of $\{0\}$, which **merges** the two wells that were visible for $t+\tau < 0$ into one single well. Finally, the **early rise** of the singular values near $[t,\, t+\tau] = [-1,\, 0]$, as shown in figure 6.1, can be considered an **early-warning signal** for a regime shift, with respect to our setting: The attractor loses its **resilience** near the critical transition or bifurcation. The same can be observed in the coherence ratios in figure 6.4.

For $t \geq 0$, the right hand side of (6.18) vanishes for $x \in \{-w(t), 0, w(t)\}$. $M = \{(t, 0),\, t \in [-20, 20]\}$ becomes finite time repulsive with the birth of the two symmetric finite time attractors $M_\pm = \{(t, \pm\omega(t)),\ t \geq 0\}$. As shown by the matrices of finite time transition probabilities in figure 6.3(a)-(c), the global dynamics yields transport between three aggregates each supported on one zero solution from the set $\{-w(t), 0, w(t)\}$. Indeed, the second and third singular values in figure 6.1 converge rapidly towards values close to 1. This implies the emergence of three coherent sets that partition the state space. In particular, $u_2^t(\epsilon)$ and $v_2^t(\epsilon)$ partition the phase space into two coherent sets. This is confirmed by the convergence of coherence ratios towards 1, as shown by figure 6.4 for $t+\tau > 0$. In addition, as detailed in section 6.2-6.3, the stochastic transition matrix Q^t is best suited to test, a priori, the occurrence of coherent sets. Indeed, robust coherent sets yield minimum dispersion when transported forward and backward via Q^t. Hence, besides the rise of the coherence ratios near 1 in figure 6.4, coherent sets that emerge

from the new dynamical regime are concretely visible in the structure of the matrix Q^t in figure 6.5. Singular vectors $u_3^t(\epsilon)$ and $v_3^t(\epsilon)$ yield a finer partition of three coherent sets

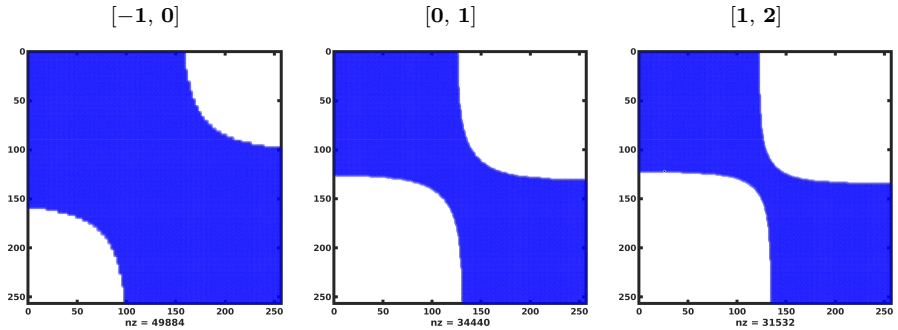

Figure 6.5: Changes of the transition matrices Q^t.

with one (in the middle) supported in the neighborhood of the repellor $\{0\}$, see figure 6.3(d)-(i) and figure 6.5. The support of $v_3^t(\epsilon)$ expands as the reachable phase space expands for $t + \tau > 0$ due to the repelling nature of the trivial solution, whose radius of repulsivity is bounded by the attracting pair of solutions. The rise of the singular values, as shown in figure 6.1, is also a consequence of the expansion of the image phase space for $t > 0$. This is similar to the eigenvalue trends in autonomous set-oriented bifurcations studied in [57].

The system (6.18) is used in this work in order to show how variations of the singular values and corresponding singular vectors can serve as relevant observables to depict finite time bifurcations and possible early warning signals. In what follows, we will be more realistic and closer to our main goal by studying nonautonomous two-dimensional incompressible systems, which undergo critical changes of coherent sets in their finite time evolution. A critical transition of a coherent set (or dominant flow pattern) in our interpretation is a **split** of a vortex similar to the Antarctic polar vortex break up. Thus, based on the behavior of the singular values (6.10) for different time windows $[t,\, t + \tau]$, we will study generic early warning-signals of a sudden split of a pattern.

6.4.2 Spectral signatures for the nonautonomous transition dynamics in the double gyre flow

We study the spectral signature of a vortex transition given the finite time dynamics of an incompressible two-dimensional toy model known as the double gyre flow. We consider

the ordinary differential equation

$$\begin{aligned}\dot{x}(t) &= -(1-s(t))\pi\sin(\pi x)\cos(\pi y) - \pi s(t)\sin(2\pi x)\cos(\pi x)\\ \dot{y}(t) &= (1-s(t))\pi\cos(\pi x)\sin(\pi y) + 2\pi s(t)\cos(2\pi x)\sin(\pi y).\end{aligned} \tag{6.21}$$

Here $s(t)$ is the time-dependent bifurcation parameter defined by

$$s(t) = \begin{cases} 0 & \text{if } t \leq 0 \Rightarrow \text{ single gyre pattern,} \\ t^2(3-2t) & \text{if } 0 < t < 1 \Rightarrow \text{ nonautonomous dynamics,} \\ 1 & \text{if } t \geq 1 \Rightarrow \text{ double gyre pattern.} \end{cases}$$

The system (6.21) is actually asymptotically autonomous, given that the bifurcation parameter, which induces the nonautonomous vector field of (6.21), is only a function of t in $(0,\, 1)$. As shown in figure 6.6 the system dynamics displays a single rotating vortex pattern for $t \leq 0$ then a double rotating vortex pattern for $t \geq 1$. The nonautonomous dynamics is restricted to $t \in [0,\, 1]$, where the transition from a single to a double gyre pattern happens. As in the previous section, singular values (6.10) are used to understand the finite time changes of the single vortex pattern given by the corresponding singular vectors (6.11), as the transition occurs. Though the transition of a vortex is different from a proper splitting, it is crucial to understand the behavior of the singular values during the changes of the first vortex pattern during this process. This is equivalent to apprehend the singular values as measures of the finite time changes of their corresponding singular vectors, provided that they are close to 1.

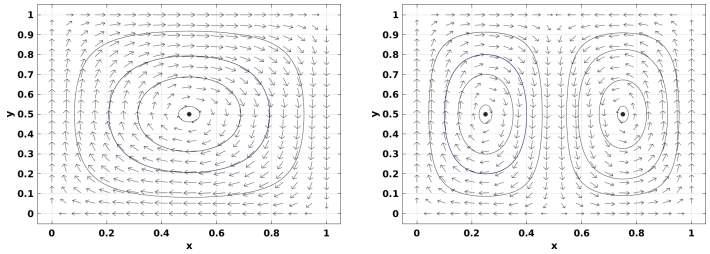

Figure 6.6: The velocity field of (6.21) for $t \leq 0$ (left) and $t \geq 1$ (right).

Regarding the numerical integration of (6.21), a time interval of length 1, i.e. $\tau = 1$ given the time interval $[t,\, t+\tau]$, turns out to be necessary to approximate a realistic pattern or gyre from the singular vectors (6.11). In order to study the changes of the different singular values within a sliding window approach, we choose the time intervals $[t,\, t+\tau]$

such that $\tau = 1$ but the initial times $t \leq 0$. The system (6.21) is integrated using a 4th order Runge-Kutta scheme and studied in the spatial domain $[0,\, 1] \times [0,\, 1]$. The latter is subdivided into 2^{12} equally sized box with 100 uniformly distributed test points initialized in each box. We set up the transition matrix (6.8) for each $[t,\, t+1]$ and compute the SVD to extract coherent patterns from the singular vectors and their corresponding singular values. We will then explore the spectral changes accompanying the pattern transition. More specifically, starting from a single pattern when $t + 1 < 0$, we track its behavior as time evolves.

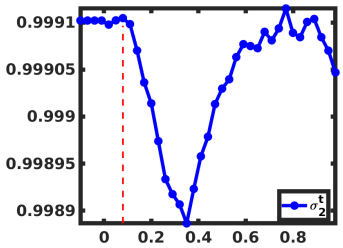

Figure 6.7: Second singular values of (6.8) for different time intervals $[t,\, t+1]$, plotted with respect to the final times $t + 1$.

Figure 6.7 shows the changes of the second singular values of the transition matrices (6.8) for different time windows $[t,\, t+1]$. We see three different trends of σ_2^t: A constant trend, a decreasing trend and an increasing trend. The constant trend corresponds to a stable regime in the sense that the left and right singular vectors patterns do not change as the time interval moves and are even both indistinguishable – they both look like the pattern shown in figure 6.8(a). The corresponding left and right singulars vectors of the decreasing trend of the singular values in figure 6.7 are shown in figure 6.8.

We clearly see that the left singular vectors (figure 6.8(a)-(d)) at initial times t and the respective right singular vectors (figure 6.8(e)-(h)) at final times $t + 1$ are no longer indistinguishable. Indeed, as the second gyre (red color) starts to rise from the right hand side of the domain at final times $t + 1$, we see that the initial gyre (the blue colored pattern) starts to shrink (figure 6.8(e)-(h)), while at initial times t it does not (figure 6.8(a)-(d)). This shrinking process of the initial vortex is captured by the singular values with a decreasing trend (figure 6.7). The more the second gyre emerges and increases in size, the more the initial gyre undergoes a fold like shrink. Finally, the rising singular values in figure 6.7 correspond to the singular vectors shown in figure 6.9.

The emerging regime of the second gyre is no longer causing the shrinking of the first gyre.

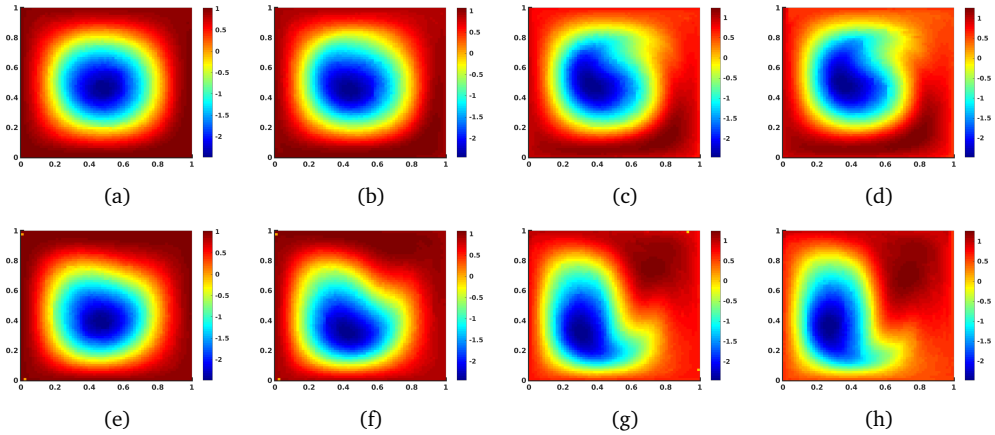

Figure 6.8: Changes of the second dominant left singular vectors (a)-(d) at initial times t, corresponding right singular vectors (e)-(h) at final times $t+1$, for the **decreasing trend** of the singular values in figure 6.7.

In fact, both gyres start to increase in size. This similar to the changes of the coherent sets generated by $v_2^t(\epsilon)$ in figure 6.3(e)-(f). The finite time evolution of the system is then similar to the post bifurcation behavior of the one-dimensional toy model (6.18). Indeed, the left singular vectors (figure 6.9(a)-(d)) at time t exhibit two coherent sets which are separately mapped, each, to the coherent sets at times $t+1$ (figure 6.9(e)-(h)). This case study is particularly interesting in explaining the trends of singular values with respect to the behavior of the corresponding singular vectors patterns. In the next section, we study the early warning signals of a proper pattern splitting.

6.4.3 Early-warning signals for a vortex splitting regime

We study a nonautonomous reformulation of the Duffing-type oscillator studied in [57]. It is defined by time-dependent vector field as

$$\begin{aligned} \dot{x} &= y \\ \dot{y} &= \arctan(t)x - x^5 \end{aligned} \tag{6.22}$$

The autonomous version of this model was studied in [57], where spectral indicators of the bifurcation of almost invariant sets were broadly investigated. Here, we explore early warning signals of the critical transition in the sense of splitting of coherent patterns that are supported in a neighborhood of the origin. The latter is the trivial critical point of (6.22) which – in the autonomous version – undergoes a pitchfork bifurcation. This bifurcation was used in [57] to study the splitting of dominant almost-invariant sets

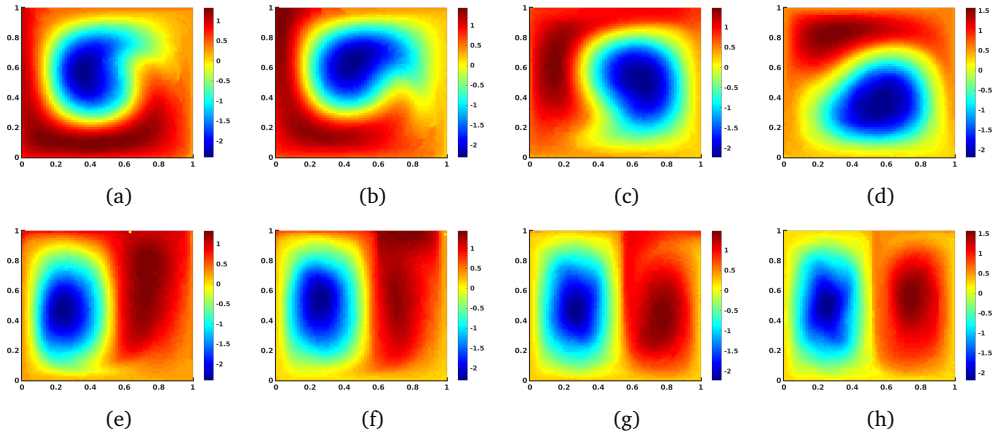

Figure 6.9: Changes of the second dominant left singular vectors (a)-(d) at initial times t, corresponding right singular vectors (e)-(h) at final times $t+1$, for the **increasing trend** of the singular values in figure 6.7.

supported in a neighborhood of $(0,0)$. The present work will also target coherent sets supported around $(0,0)$. In fact, since we are also seeking a critical transition which is related to the local bifurcation, even though the system is now time-dependent. In addition, we believe that the adequate coherent pattern generated by (6.22) is to the best of our knowledge, the most suitable simple approximation of the Antarctic polar vortex by a nonautonomous ordinary differential equation. Nevertheless, note that the only way to witness early warning signals is actually to let the system evolve in time.

We subdivide the time interval $[-10, 10]$ into subintervals $[t,\ t+1],\ t = -10, -9, \ldots, 9$ and integrate (6.22) with a 4th order Runge-Kutta scheme, that is, we use the sliding window approach again. The system is studied in the space domain $[-2,\ 2] \times [-2,\ 2]$, which is subdivided into 2^{14} square boxes with 400 uniformly distributed test points in each box. We then obtain the transition matrix (6.8) for each interval $[t,\ t+1]$, and compute the SVD for extracting coherent patterns from singular vectors and corresponding singular values.

Unlike the double gyre system studied in section 6.4.2, the patterns generated by the second dominant singular vectors, v_2^t and u_2^t, are not convenient to study the set-oriented critical transition for this system. Indeed, the singular vectors patterns are not supported in a neighborhood of $(0,0)$, as shown in figure 6.10.

As a matter of fact, the corresponding singular values in figure 6.11 (left) exhibit, for different time intervals $t,\ t+1]$, no trends that are suited to make any early warning predictions. Moreover, we can observe that the nonautonomous dynamics of the singular

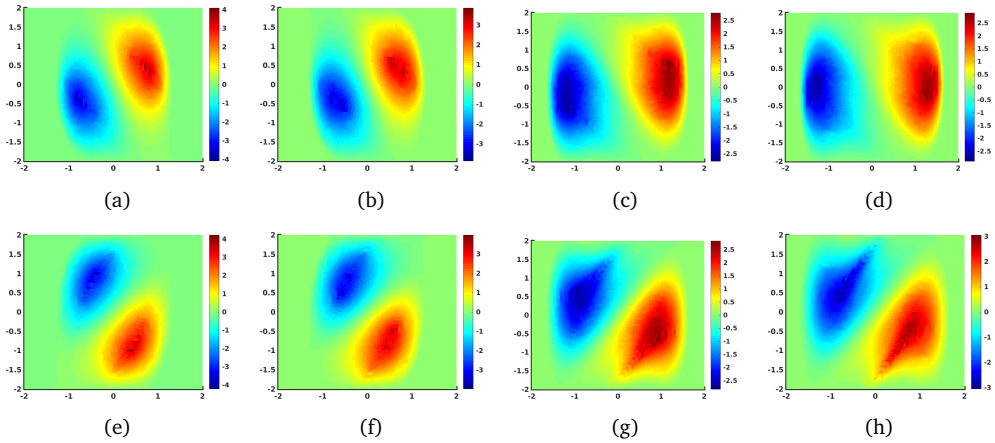

Figure 6.10: Changes of second dominant left singular vectors (a)-(d) at initial times t, corresponding right singular vectors (e)-(h) at final times $t+1$ for increasing time t.

vectors in figure 6.10 within one time interval $[t,\, t+1]$ (figure 6.10(a) and figure 6.10(e), for instance) yields a clock-wise rotation of the patterns by an angle $\theta < \pi$. Hence, it

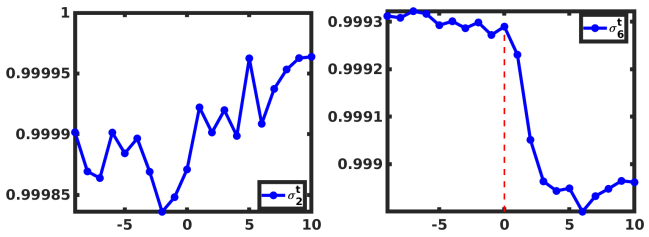

Figure 6.11: Second (left) and sixth dominant singular values (right) for different time intervals $[t,\, t+1]$. Final times $t+1$ in the $x-$axis.

is necessary to have the patterns supported around $(0,0)$, in order to sense the critical transition induced by the pitchfork bifurcation. We find that the sixth dominant singular vectors v_6^t, u_6^t fulfil this requirement.

Figure 6.11 (right) shows the changes of the sixth dominant singular values for each time interval $[t,\, t+1]$. One sees that, from both sides of $t+1=0$, the singular values in figure 6.11 exhibit two different behaviors separated by the red dashed vertical line: **nearly constant** singular values and **rapidly decreasing** singular values. The singular vector patterns corresponding to the nearly constant singular values are stable and look like those shown in figure 6.12 (a) and (e).

As $t+1$ becomes positive, the systems shows prior hints for a radical pattern splitting. This is clearly seen in figure 6.11 (right), where we see a **rapid decreasing** of the singular

values as an early warning signal for pattern splitting. The corresponding singular vectors are shown in figure 6.12, where we clearly see the splitting process of the coherent vectors pattern (in blue). The changes are captured by the corresponding singular values in figure 6.11 (right) with a fast decrease as the pattern is elongated and contracted by the finite time dynamics. Similar results were obtained in [57], where a bifurcation of almost-invariant sets was preceded by a decrease of eigenvalues of the transition matrix, see chapter 5. In the present work, a coherent pattern splitting is preceded by the same changes in the corresponding singular values. The same was found in section 6.4.2 in figure 6.8, where the dropping phase of the singular values in figure 6.7 was however not followed by a splitting. That is to say that the shrinking of the patterns before they split is captured in the singular values as a **generic** warning sign. In the next section, we will

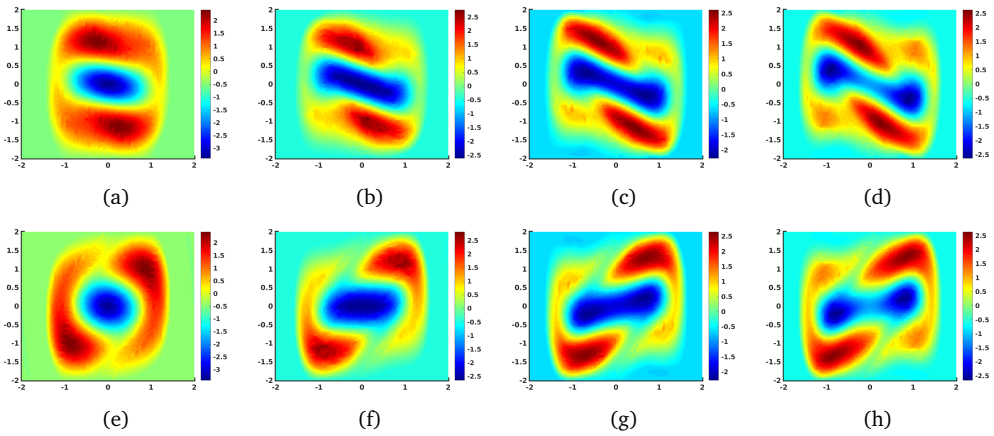

Figure 6.12: Changes of sixth dominant left singular vectors (a)-(d) at initial times t, changes of the corresponding right singular vectors (e)-(h) at final times $t+1$, for the **rapidly decreasing** singular values in figure 6.11.

confirm these indicators by predicting a concrete real-world application pattern splitting.

6.5 Predicting the Antarctic polar vortex sudden split of September 2002 from recorded satellite data

In the month of September 2002, an unusual critical transition occurred in the Antarctic polar vortex region: the ozone hole suddenly split into two rotating blobs of air, as a consequence of the stratospheric warming. This is particularly the first rare event of this kind, which is recorded in the meteorological history of the Southern Hemisphere [2].

Many scientific studies [7, 11, 38] have focused on understanding the main causes of the

splitting of the ozone layer. In [11], for instance, the vortex dynamics is associated to the evolution of chemical constituents such as ozone O_3 and chlorine monoxide (CIO), before, during and after the splitting. Furthermore, based on satellite velocity data, it is very well understood that the splitting occurred during the last week of September 2002, more precisely, it between September 24 and September 27, see figure 1.1.

In the present work, we are going to study the early-warning indicators of the sudden split by analyzing the finite time global dynamics of the vortex from recorded velocity data. Given the available velocity data from the ECMWF Interim data set[1], we track changes of the pattern corresponding to the daily ozone concentration, as illustrated in figure 1.1. The ozone hole can be identified as an isolated vortex of air slowly rotating over Antarctica. Using finite-time Lyapunov exponents, the different geometric shapes of the Antarctic polar vortex during the splitting event of September 2002 were studied [9].

The global ECMWF data is given at a temporal resolution of 6 hours and a spatial resolution of a 0.5° in longitude and latitude degree, respectively. We focus on the stratosphere over the southern hemisphere and consider the velocity data from September 1, 2002 to October 1, 2002 on a 600 K isentropic surface. Thus, the equation of motion of the atmospheric dynamics in that region is interpreted as a two-dimensional time-dependent ordinary different equation

$$\begin{aligned} \dot{x} &= u(x, y, t) \\ \dot{y} &= v(x, y, t) \end{aligned} \tag{6.23}$$

defined on discrete points (t, x, y). Using interpolation in space and time we can integrate solutions again by a 4th order Runge-Kutta scheme and obtain an approximate flow map (2.19). For the set-oriented analysis of the global dynamics, we use a square domain centered at the south pole with side lengths $12,000$km. We subdivide the domain using 2^{10} boxes. We choose $n = 25$ sample points uniformly distributed in each box and compute the transition matrices (6.8). The polar vortex at different times is then considered as a coherent set approximated by the singular vectors of (6.8) and the singular values are used to identify early warning signals.

Previous studies [15] suggest that an initial time interval of length greater or equal to two weeks is ideal in order to have a good approximation of coherent sets from the second dominant singular vectors. That is why we set our initial time interval to 15 days, i.e.

[1] http://data.ecmwf.int/data/index.html

September 1^{st}, 2002 to September 15, 2002. Hence, if the second time interval has the same length, then we will not be able to observe the desired critical transition. Therefore, we set the first 15 days as our reference time interval and use a new technique that we refer to as the **long trajectory approach** with **singular value scalings**.

The **long trajectory approach** works as follows: Let $t_0 =$ September 1 and $T =$ September 15, and $[t_0,\, T]$ is the reference time interval. We then fix t_0 and integrate (6.23) for increasing time intervals $[t_0,\, T+i]$, $i = 0, 1, 2 \ldots, 16$, given that $T + 16$ corresponds to October 1. For every time interval, an SVD of the corresponding transition matrices is computed. Since the initial time t_0 is fixed, the left singular vectors are not expected to vary noticeably for all the different time intervals. Therefore, we use the right singular vectors to study the changes of the polar vortex. The second dominant singular values $\hat{\sigma}_2^i$ change as well. But we cannot compare two different singular values, since the different time intervals under consideration have different lengths. To solve this problem we propose a **singular value scaling** technique in the following way:

In addition to the long term trajectories we use the short term sliding window approach with time intervals $[t,\, t+1],\ t = 15, 16, \ldots, 30$. These are time intervals of one day, starting at September 15. We then compute the SVD and collect the second dominant singular values $\tilde{\sigma}_2^t$. We neglect the short term singular vectors. Note that $t + 1 = T + i$, $i = 1, 2, \ldots, 16$, $t = 15, 16, \ldots, 30$. From the singular values $\hat{\sigma}_2^i$ and $\tilde{\sigma}_2^t$, the principle of the scaling consists of finding singular values that implicitly represent time intervals of the same length as the reference time interval $[t_0,\, T]$. That is, we fix $\sigma_2^0 := \hat{\sigma}_2^0$ corresponding to the reference time interval $[t_0,\, T]$ and scale the $\hat{\sigma}_2^i$, $i = 1, 2, \ldots, 16$ corresponding to $[t_0,\, T+i]$, in order to be able to compare them with σ_2^0. This is obtained from the scaling equation

$$\sigma_2^i = \frac{\hat{\sigma}_2^i}{\Pi_{j=1}^{i} \tilde{\sigma}_2^{T+j}},\ i = 1, \ldots, 16. \tag{6.24}$$

In this way, all the singular values σ_2^i, $i = 0, \ldots, 16$ represent time intervals of the same length as $[t_0,\, T]$. Moreover, they can be used to identify early warning signals.

Figure 6.13 shows the scaled singular values σ^i plotted with respect to the final time $T+i$, $i = 0, \ldots, 16$. One observes two separated behaviors: **increasing** singular values from September 15 to September 20 and **rapidly decreasing** singular values from September 21 to September 25.

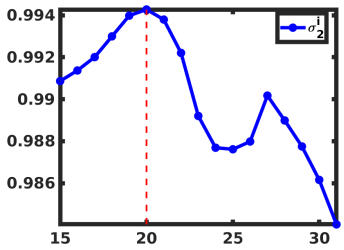

Figure 6.13: The scaled second singular values σ_2^i from (6.24) plotted with respect to final time $T + i$. The trends correspond to the different behaviors of the polar vortex.

The singular vectors corresponding to the increasing singular values are shown in figure 6.14. Note that, for more clarity, only certain negative level sets that correspond to the numerical approximation of the ozone hole were plotted.

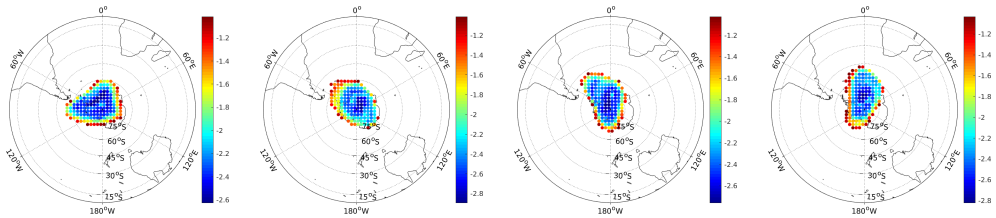

(a) (b) (c) (d)

Figure 6.14: Right singular vectors from (a)-(d) September 15, 18, 19, 20 corresponding to the increasing singular values in figure 6.13.

In the previous examples we have observed that rising singular values yield corresponding singular vectors whose support or level sets expand in size. We consider this as a stable regime, in the context of this work. Actually, the Antarctic polar vortex is very stable from September 15 to September 20. However, from September 20 to September 24, the singular values in figure 6.13 begin to decrease very fast. The corresponding right singular vectors are shown in figure 6.15. The shape changes of the right singular vector

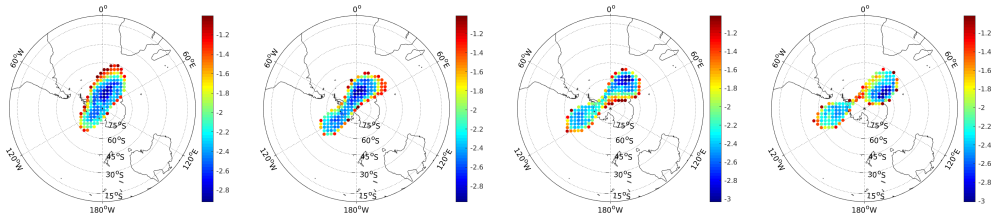

(a) (b) (c) (d)

Figure 6.15: Right singular vectors from (a) September 21 to (d) September 24 corresponding to the rapidly decreasing singular values in figure 6.13.

pattern are very similar to those in the high order nonautonomous Duffing oscillator in figure 6.12. The singular values in figure 6.13 have then successfully confirmed the generic early-warning signals with a rapid changes in magnitude. This sudden change is characterized by a fast drop in magnitude of the singular values, as shown in figure 6.13. Thus, an early-warning signal of the splitting occurs from (a) September 21 to (d) September 24, where we start to notice a break up of the rotating vortex into two blobs of air, as shown in figure 6.15.

The post splitting scenario begins at September 27. From this date onward, the northwestern blob of the ozone hole starts to disappear, while the southwestern blob begins to increase again in size to recover the initial shape before splitting. This can be classified as a reformation phase. Besides, the underlying ozone hole pattern is very well captured by the right singular singular vectors from September 27 to October 1; see figure 6.16. As shown in figure 6.13 the corresponding singular values exhibit a particularly distinguishable trend with a nearly constant rate of decrease in magnitude.

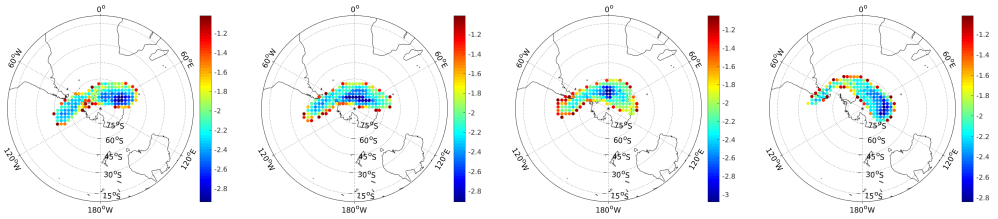

(a) (b) (c) (d)

Figure 6.16: Right singular vectors from (a)-(c) September 27, 28, 29 to (d) October 1 corresponding to the linearly decreasing singular values in figure 6.13.

6.6 Summary

At the end, one may realise that this study is mainly implemented around singular value decompositions of transition matrices as mentioned in chapter 3 (section 3.1.2 (3.4)), which are generated from finite time evolutions of time-dependent systems. Thus, dominant singular vectors and their sign patterns yield numerical approximations of slowly mixing regions, while corresponding singular values exhibit the potential to measure their shape changes. On this basis, trends of the singular values and sign patterns of singular vectors are mutually used, as observables, to design and anticipate imminent sudden changes in the nonautonomous dynamics of vortex-like patterns. This technique is used to identify early indicators of the sudden split of the Antarctic polar

vortex in September 2002, from recorded satellite velocity data. This real-world critical transition may be classified as a rare event. Nevertheless, our probabilistic approach can be applied to a wider family of incompressible flow patterns undergoing similar changes. In a theoretical perspective, future studies may address a combination of geometric methods and the above probabilistic approach to find lower bounds of the dominant singular values, in order to abstractly control the changes of the patterns.

7 Conclusion

In this thesis, we were preoccupied to answering the following question: Suppose we have at our disposal the Antarctic vortex rotating dynamics velocity data of the year 2002. Is it possible to design early-warning signs prior to the sudden splitting regime that occurred between the days of September 24 and September 25, 2002, as shown in figure 1.1?

To answer this question, we chose two main mathematical frameworks: Set-oriented dynamical systems and nonautonomous bifurcation theory. With these two frameworks, we aimed to develop an analytical set-oriented bifurcation theory with numerical illustrations and use our results to propose a mathematically justifiable answer of the above question. However, the approach seems unusual with respect to the known traditional bifurcation theory but also innovative with respect to the chosen frameworks. Moreover, a legitimate question may also address the "why" of our choice, given the amount of mathematical frameworks that can exist. Indeed, we choose a set-oriented dynamical system approach to be able to study the ensemble evolution of dynamical systems, as with this method the phase space can be divided into distinct subsets such that there is a very small probability that trajectories in one subset will leave the subset in a relatively short time. We thus, hope that the dynamics of one of these subsets mimic the dynamics of the Antarctic polar vortex. In other words, we choose subsets that are able to flow in space and time with a possibility of changing shape, which suppose that these subsets are generated by a nonautonomous dynamical systems. Hence, a set-oriented nonautonomous dynamical system approach was a promising starting idea and was actually the idea adopted to conducted our research. Nonautonomous dynamical systems are highly relevant to model the dynamics of complex systems such as the dynamics of the Antarctic polar vortex. Indeed, complex systems are known to exhibit self-organization

and self-adaptation in their dynamical behavior and, most importantly, they can show dynamically independent behaviors in different time intervals. The latter is a typical property of nonautonomous dynamical system, since time-dependent systems exhibit independent dynamics within different time intervals. Finally, given measurable subsets from the set-oriented time-dependent dynamics, the challenging task was to find suitable criteria in order to characterize a shape change as a bifurcation. In the context of this work, shape change in the sense of splitting, as illustrated in figure 1.1, is of interest.

Changes in the dynamical behavior of a complex systems, such as the Antarctic polar vortex 2002 break up, are referred to as critical transitions. Therefore, the splitting regime observed in figure 1.1 can be classified as a critical transition. Moreover, empirical evidence of early-warning signals before a critical transition was brought to prominence by scientists in ecology. However, mathematical foundations of early-warning signals observables were largely lacking. That is why, in order to predict the regime shift illustrated in figure 1.1, we reformulated our research study as a combination of set-oriented dynamics and finite time bifurcation theory for findings observables that can design early-warning signals.

In this thesis, we considered a special class of dynamical systems that are able to dynamically mimic the the Antarctic polar vortex rotating dynamics. Indeed, we consider incompressible systems whose dynamics consist of rotating trajectories around a global fixed point (i.e., solution of the zero of the velocity field). The discrete spectrum of the perturbed transfer operator yields almost-invariant sets/coherent sets which are supported on the whole phase space and, in particular, on a neighborhood of the fixed point. Moreover, these special systems are built in such a way that they undergo a (finite time) bifurcation which leads to a splitting of the phase space into two rotating gyre-like trajectories. Note that the main concept of finite time dynamical systems can be transferred to incompressible flows, even though [58] was developed by considering dissipative systems. In this context, the discrete spectrum of the perturbed transfer operator is used as observables to characterize early-warning signs of critical transition of patterns in the sense of splitting.

The lack of prior studies of set-oriented bifurcations in the sense of a splitting of patterns made this work challenging. In fact, a statistical approach to analyze bifurcation of deterministic systems is not a widely investigated topic. Known works include [17] who characterized the one-dimensional pitchfork normal form based on changes of the deterministic Frobenius-Perron operator's discrete spectrum. Results in [17] served

somehow as a referential work for the beginning of our research. Indeed, a set-oriented approach is just a particular statistical approach which, besides analyzing the ensemble evolution of the underlying dynamics, extract optimal almost-invariant/coherent sets. That is why, in chapter 4, we studied changes of the discrete spectrum of the perturbed transfer operators P_ϵ^t as a bifurcation parameter is varied. Moreover, as mentioned earlier, we consider two-dimensional incompressible systems undergoing a pitchfork bifurcation. Findings in chapter 4, were critically interesting in the sense that they allowed us to understand the manner in which we should concretely approach the study bifurcation of almost-invariant patterns using dominant real eigenvalues and their eigenvectors of the perturbed transfer operator as indicators. Indeed, from chapter 4, we understood that a set-oriented bifurcation should not be directly linked to the local bifurcation that is intrinsic to the local properties of the underlying dynamical system. This implies a shift in the critical parameter p value. That means, the critical parameter value p for the bifurcation of almost invariant sets may not coincide with the critical parameter value $\overline{p}$for the system's local bifurcation. That is why, in chapter 5 the bifurcation of almost-invariant sets is studied from a purely global approach. Besides, finding a critical value of p that determines the set-oriented bifurcation did not matter. What really mattered was only the change of dominant patterns as an external parameter p is varied. The study was developed from scratch due to the lack of previous work in this regard. Results from chapter 5 were extended to time-dependent dynamical systems in chapter 6 where dominant singular values and their singular vectors were used as observables to characterize early-warning signs of pattern splitting. Our findings were successfully confirmed in application with the Antarctic polar vortex velocity data. Indeed, the spectral warning signs for the splitting of the Antarctic polar vortex in September 2002 were successfully identified. Trends of the singular values and sign patterns of singular vectors are mutually used, as observables, to design and anticipate imminent sudden changes in the nonautonomous dynamics of vortex-like patterns.

This thesis has proved that there is a scientific answer for mathematically characterizing empirical evidence of early-warning signals for the sudden split of the Antarctic polar vortex in September 2002. Furthermore, this work may open the door to addressing more general research questions including problems involving vortex splitting phenomena in the wide field of (geophysical) real world fluid dynamics.

Bibliography

[1] M. J. Olascoaga and G. Haller. *Forecasting sudden changes in environmental contamination pattern.* Proc. National Acad. Sci. **109**, 4738–4743, 2012.

[2] WMO, 2002. *Antarctic ozone hole splits in two.* Press Release No. **681**, 1 October, 2002.

[3] M. Scheffer. *Critical Transitions in Nature and Society*. Princeton Univ. Press, 2009.

[4] M. Scheffer et al. *Early-warning signals for critical transitions.* Nature **461**, 53–59, 2003.

[5] M. Scheffer et al. *Early-warning signals for critical transitions.* Nature **461**, 53–59, 2003.

[6] D. Sornette. *Predictability of catastrophic events: material rupture, earthquakes, turbulence, financial crashes and human birth.* Proceedings of the National Academy of Sciences USA **99**, 2522–2529, 2002.

[7] A. Simmons et al. *ECMWF analyses and forecasts of stratospheric winter polar vortex break up: September 2002 in the Southern Hemisphere and related events.* J. Atmos. Sci. **62**, 668–689, 2005.

[8] T. Shepherd and R.A. Plumb. *The antarctic vortex splitting event.* J. Atmos. Sci., Special Issue 62, 2005.

[9] F. Lekien and S. D Ross. *The computation of finite-time Lyapunov exponents on unstructured meshes and for non-Euclidean manifolds.* Chaos **20**, 017505, 2010.

[10] J. Guckenheimer, P. Holmes. *Nonlinear Oscillations, Dynamical Systems, and Bifurcations of Vector Fields.* Springer, New York, 1983.

[11] P. Ricaud et al. *Polar vortex evolution during the 2002 Antarctic major warming as observed by the Odin satellite.* J. Geophys. Res., **110**, D05302, doi:10.1029/2004JD005018, 2005.

[12] G. Froyland. *Finite approximation of Sinai-Bowen-Ruelle measure for Anosov systems in two dimensions.* Random and Comput. Dynam., **3(4)**, 251-264, 1995.

[13] M. Dellnitz and O. Junge. *On the approximation of complicated dynamical behavior.* SIAM J. Numer. Anal. **36**, 491–515, 1999.

[14] G. Froyland and M. Dellnitz. *Detecting and locating near-optimal almost-invariant sets and cycles.* SIAM Journal on Scientific Computing **24**, 1839–1863, 2003.

[15] G. Froyland, N. Santitissadeekorn, and A. Monahan. *Transport in time-dependent dynamical systems: Finite-time coherent sets.* Chaos **20**, 043116, 2010.

[16] G. Froyland. *An analytic framework for identifying finite-time coherent sets in time-dependent dynamical systems.* Physica D **250**, 1–19, 2013.

[17] P. Gaspard, G. Nicolis, A. Provata and S. Tasaki. *Spectral signature of the pitchfork bifurcation: Liouville equation approach.* Phys. Rev. E **51**, 74–94, 1995.

[18] A. Tantet, F.R van der Burgt and H.A. Dijkstra. *An early warning indicator for atmospheric blocking events using transfer operators.* Chaos **25**, 036406, 2015.

[19] O. Junge, J.E. Marsden and I. Mezic. *Uncertainty in the dynamics of conservative maps.* Proc. IEEE Conference on Decision and Control (CDC 2004), 2225–2230, 2014.

[20] P. Grover, S.D. Ross, M.A. Stremler and P. Kumar. *Topological chaos, braiding and bifurcation of almost-cyclic sets*. Chaos **22**, 043135, 2012.

[21] G. Froyland. *Statistically optimal almost-invariant sets.* Physica D **200** 205–219, 2005.

[22] S. M. Ulam. *Problems in Modern Mathematics.* Courier Dover Publication, 2004.

[23] E. Seneta. *Non-negative Matrices and Markov Chains.* Springer, 2006.

[24] T. Kato. *Perturbation Theory of Linear Operators.* Springer, Berlin, 1995.

[25] Strogatz, Steven H. *Nonlinear Dynamics and Chaos: With Applications to Physics, Biology, Chemistry, and Engineering.* Reading, Mass: Addison-Wesley Pub, 1994.

[26] B. O. Koopman. *Hamiltonian Systems and Transformations in Hilbert Space.* Proc. Natl. Acad. Sci. U. S. A. **17** (1931), no. 5, 315–318.

[27] John von Neumann. *Proof of the Quasi-Ergodic Hypothesis.* Proc. Natl. Acad.Sci. U. S. A. **18** (1932), no. 2, 70–82.

[28] Y. A. Kuznetsov. *Elements of Applied Bifurcation Theory.* Second Edition. Springer-Verlag, New York, 1998.

[29] P. Walter. *An introduction to Ergodic Theory.* Springer-Verlag, 1982. MR **84e:**28017.

[30] H. Poincaré. *Les méthodes nouvelles de la mécanique céleste.* Gauthiers-Villars, Paris, 1892-1899, (3 volumes, in French).

[31] K. -J. Engel and R. Nagel. *One parameter semigroups for linear evolution equations.* Springer, New York, 2000.

[32] A. Lunardi. *Analytic Semigroups and Optimal Regularity in Parabolic Problems.* Birkhäuser, 1995.

[33] G. Froyland, O. Junge, and P. Koltai. *Estimating long term behavior of flows without trajectory integration: the infinitesimal generator approach*. SIAM Journal on Nuerical Analysis, 51(1):223-247, 2013.

[34] C.D. Meyer. *Stochastic complementation, uncoupling Markov chains, and the theory of nearly reducible systems.* SIAM Rev. **31**, 240–272, 1989.

[35] P. Deuflhard, W. Huisinga, A. Fischer and C. Schütte. *Identification of almost invariant aggregates in reversible nearly uncoupled Markov chains.* Linear Algebra and its Applications **315**, 39–59, 2000.

[36] G. Froyland and K. Padberg-Gehle. *Almost-invariant and finite-time coherent sets: directionality, duration, and diffusion.* In W. Bahsoun, C. Bose, G. Froyland (eds.): Ergodic Theory, Open Dynamics, and Coherent Structures. Springer, pp. 171–216, 2014.

[37] M. Dellnitz, G. Froyland, and O. Junge. *The algorithms behind GAIO: Set-oriented numerical methods for dynamical systems.* In B. Fiedler (ed.): Ergodic theory, analysis, and efficient simulation of dynamical systems. Springer, Berlin, pp. 145–174, 2001.

[38] T.Shepherd and R. A. Plumb. *The antarctic vortex splitting event.* J. Atmos. Sci., Special Issue 62, 2005.

[39] G. Haller. *Finding finite-time invariant manifolds in two-dimensional velocity fields.* chaos 10:99–108, 2000.

[40] V. Rom-Kedar, A. Leonard, and S. Wiggins. *An analytical study of transport, mixing and chaos in an unsteady vortical flow.* Journal of Fluid Mechanics, 214:347–394, 1990

[41] H. Aref. *The development of chaotic advection*. Physics of Fluids, 14(4) 1315-1325, 2002

[42] S. Wiggins. *Chaotic Transport in Dynamical Systems*. Springer-Verlag, New York,NY, 1992.52.

[43] S. Wiggins. *The dynamical systems approach to Lagrangian transport in oceanic flows*. Annu. Rev. Fluid Mech., 37:295–328, 2005.

[44] J. D. Meiss. *Symplectic maps, variational principles, and transport*. Rev. Mod. Phys., 64(3):795–848, 1992.

[45] Jui Ding and Aihui Zhou. *statistical properties of deterministic systems* Springer Berlin Heidelberg New York

[46] P. Gaspard and S. Tasaki. *Liouvillian dynamics of the Hopf bifurcation.* Phys. Rev. E **64**, 056232, 2001.

[47] Baladi V. *Positive transfer operators and Decay of correlations.* World Scientific, Singapore, 2000.

[48] Gaspard P. *Chaos, Scattering and statistical Mechanics.* Cambridge, University Press, Cambridge, 1998.

[49] Lasota A and Mackey M. C. *Chaos, Fractals and Noise.* Spring, Berlin, 1994.

[50] Pazy A. *Semigroups of Linear Operators and Applications to Partial Differential Equations.* Springer-Verlag-New York, 1983.

[51] N. Dunford and J.T.Schwartz. *Linear Operators*. Wiley Interscience, NewYork, 1958, 1963, 1971, Vols.I—III

[52] Da Prato and Zabczyk J. *Ergodicity for Infinite Dimensional Systems.* Cambridge University Press, Cambridge, 1996.

[53] M. Pollicott. *Meromorphic extensions of generalized zeta functions.* Invent. Math. 85(1):147-164. 1986.

[54] D. Ruelle. *Resonances of chaotic dynamical systems. Phys Rev Lett 56(5):40-407. 1986.*

[55] D. Ruelle. *Locating resonances for Axiom-A dynamical systems*. J Stat Phys 44(3-4):281-292. 1986.

[56] Batterley O. and Liverani C. *Smooth Anosov flows: correlation spectra and stability.* Journal of Modern Dynamics, 1:301-322, 2007.

[57] M. Ndour and K. Padberg-Gehle. *Predicting bifurcations of almost-invariant patterns: a set-oriented approach.* Submitted, 2019. Preprint at http://arxiv.org/abs/2001.01099.

[58] M. Rasmussen. *Attractivity and Bifurcation for Nonautonomous Dynamical Systems.* Lecture Notes in Mathematics 1907, Springer, 2007.

[59] P.E. Kloeden and M. Rasmussen. *Nonautonomous Dynamical Systems.* American Mathematical Society, 2011.

[60] M. Ndour, Padberg-Gehle and M. Rasmussen. *Spectral warning signs for sudden changes in time-dependent flow patterns.* Preprint 2020.

[61] J.B. Conway. *A course in functional analysis.* Volume 96 of Graduate texts in mathematics. Springer, 2nd edition, 1990.

[62] M.S. Birman and M.Z. Solomjak. *Spectral theory of sel-adjoint operators in Hilbert spaces.* D. Reidel Publishing Co., Inc., 1986.

[63] Alexis Tantet et al. *Crisis of the chaotic attractor of a climate model: a transfer operator approach.* Nonlinearity 31 2221. 2018

Acknowledgements

I would like to thank my supervisor Kathrin Padberg-Gehle for giving me the opportunity to engage in this research experience. As my Ph.D. advisor, she demonstrated her willingness to see this research project come to a fruitful end. I am grateful for that.

I would like to thank all the members of the Institute of scientific computing at TU Dresden and, specially, Axel Voigt who really supported me administratively, during my stay at TU Dresden. I am very grateful for that.

I would like to thank and shout out to the exciting group of the CRITICS project. I appreciate the vibrant atmosphere that was always naturally there and also the true friendship relations I ended up building in. The CRITICS was a very interesting scientific ecosystem which has allowed me to enrich my research experience, and most importantly, to encounter professors who are very generous in sharing knowledge. I want to mention Martin Rasmussen, Tobias Jaeger, Henk Djikstra, to name a few.

I would like to thank Prof. Stefano Luzzato who, during my postgraduate diploma program at ICTP, guided me in the field of dynamical systems. Discussions with stafano can be very intense and interesting at the same time with lots of insights at the end. He is very supportive and is always willing to be there for his students.

When, I started this research project, I met Alex Jean Jacques Tantet who just finished his Ph.D. in the same field. Alex, that I knew through Daniele, helped me a lot with fruitful discussions, during my early steps into this field. Alex, Daniele and I have now built a really strong friendship that goes beyond scientific interests.

I want to take this opportunity again to tell to my family, my father, my mother, my sisters, my brothers, my nephews, my nieces, etc. that I love them. My mother did not have the opportunity to do higher studies, but I am sure she would achieve way more that I am doing. Mother this work is for you!

Selbstständigkeitserklärung

Die eingereichte Dissertation zum Thema

Early-warning signals for sudden changes in dynamical flow patterns

wurde am Institut für Wissenschaftliches Rechnen der Technischen Universität Dresden unter Betreuung durch Prof. Dr. Kathrin Padberg-Gehle angefertigt. Hiermit versichere ich, dass ich die vorliegende Arbeit ohne unzulässige Hilfe Dritter und ohne Benutzung anderer als der angegebenen Hilfsmittel angefertigt habe; die aus fremden Quellen direkt oder indirekt übernommenen Gedanken sind als solche kenntlich gemacht. Die Arbeit wurde bisher weder im Inland noch im Ausland in gleicher oder ähnlicher Form einer anderen Prüfungsbehörde vorgelegt.

Dresden, den 07. April 2020

Moussa Ndour